UNIVERSITA’ DEGLI STUDI DI NAPOLI
“PARTHENOPE”

Dipartimento di Scienze Applicate

Dottorato di ricerca in
Scienze Geodetiche e Topografiche
XXIII Ciclo

GNSS/INS Integration Methods

Antonio Angrisano

Supervisors: Prof. Mark Petovello, Prof. Mario Vultaggio

Coordinatore: Prof. Lorenzo Turturici

2010

Abstract

In critical locations such as urban or mountainous areas satellite navigation is difficult, above all due to the signal blocking problem; for this reason satellite systems are often integrated with inertial sensors, owing to their complementary features. A common configuration includes a GPS receiver and a high-precision inertial sensor, able to provide navigation information during GPS gaps.

Nowadays the low cost inertial sensors with small size and weight and poor accuracy are developing and their use as part of integrated navigation systems in difficult environments is under investigation. On the other hand the recent enhancement of GLONASS satellite system suggests the combined use with GPS in order to increase the satellite availability as well as position accuracy; this can be especially useful in places with lack of GPS signals.

This study is to assess the effectiveness of the integration of GPS/GLONASS with low cost inertial sensors in pedestrian and vehicular urban navigation and to investigate methods to improve its performance.

The Extended Kalman filter is used to merge the satellite and inertial information and the loosely and tightly coupled integration strategies are adopted; their performances comparison in difficult areas is one of the main objectives of this work. Generally the tight coupling is more used in urban or natural canyons because it can provide an integrated navigation solution also with less than four satellites (minimum number of satellites necessary for a GPS only positioning); the inclusion of GLONASS satellites in this context may change significantly the role of loosely coupling in urban navigation.

In this work pseudorange and Doppler measurements are processed in single point mode; hence no differential processing is performed and no base station is necessary. For bounding the MEMS INS errors during GPS/GLONASS outages, the use of motion constraints is introduced and evaluated. To carry out the analysis a complete navigation software has been developed in Matlab environment.

The results show that the integration of GPS/INS provides satisfying performance only in good visibility conditions in both loose and tight architectures, while during GPS outages (longer than few seconds) very large errors are experienced; including GLONASS in GPS/INS integration produces significant solution improvements. As expected the tight integration shows better performance during GNSS outages, but the results obtained with GPS/INS integration in tight architecture and

GPS/GLONASS/INS integration in loose approach are often similar, suggesting the use of the latter configuration owing to its relatively simple implementation. The motion constraints provide remarkable enhancements of the navigation solution, with RMS position error of a few meters in difficult urban canyons for both loose and tight architectures.

Acknowledgements

I would like to thank my supervisor, Prof. Mario Vultaggio, for his continuous guidance and encouragement throughout my PhD studies. He was the first to believe in my ability and give me a chance to express and develop it. I am grateful to him.

I sincerely thank my co-supervisor, Prof. Mark Petovello, for his support and guidance throughout my visit at University of Calgary and after I returned in Italy; he patiently answered my questions and his valuable suggestions helped to improve my research.

I am grateful to Prof. Giovanni Pugliano, who played a major role to organize my experience in Calgary and followed my progress during the period I spent there.

Thanks to my colleagues and friends Salvatore Gaglione, Umberto Robustelli and Ciro "Gyro" Gioia. According to me, work is an important aspect of life because everyone spends almost half of his life working, and working with you gratifies me… so thank you guys.

I would also like to thank Anshu Pahadia, Thomas Williams, Peng Xie, Muhammad Haris Afzal, Li Tao ("Big Tao") and Zhe He for their significant support to my research. A special thanks to all my Calgarian friends, with whom I spent a wonderful time and maybe the best of my life.

Finally, I would like to thank my parents and my sister for their priceless love
and
my Love, without her nothing would matter.

Dedication

To my friends,

To my family,

To my Love.

Table of Contents

List of Tables

List of Figures

List of Abbreviations

ARW	Angular Random Walk
C/A code	Coarse-Acquisition code
CDMA	Code Division Multiple Access
CS	Control Segment
DGPS	Differential GPS
DOP	Dilution of Precision
DR	Dead Reckoning
ECEF	Earth Centered Earth Fixed
ECI	Earth Centered Inertial
ENU	East North Up
EKF	Extended Kalman Filter
FDMA	Frequency Division Multiple Access
GA	Ground Antennas
GDOP	Geometric Dilution of Precision
GLONASS	GLObal NAvigation Satellite System
GNSS	Global Navigation Satellite System
GPS	Global Positioning System
IGS	International GNSS Service
IMU	Inertial Measurement Unit
INS	Inertial Navigation system
KF	Kalman Filter
LBS	Location-Based Services
LC	Loosely Coupled
LS	Least Square method

MEMS	Micro Electro-Mechanical Systems
MCS	Master Control Station
MS	Monitor Stations
P code	Precise code
PDR	Pedestrian Dead Reckoning
PPP	Precise Point Positioning
PPS	Precise Positioning Service
PPS	Pulse Per Second
PR	Pseudorange
PRN	Pseudo-Random-Noise
PVT	Position Velocity Time
RAIM	Receiver Autonomous Integrity Monitoring
RMS	Root Mean Square
SPS	Standard Positioning Service
TC	Tightly Coupled
UERE	User Equivalent Range Error
USNO	US Naval Observatory
UTC	Universal Time Coordinate
VRW	Velocity Random Walk
WGS84	World Geodetic System 1984
WLS	Weighted Least Square
ZUPT	Zero Velocity Updates

Chapter 1 Introduction

In this chapter an overview of the background of this research is provided, i.e. the importance and the limitations of the satellite navigation, the reason of the integration with other sensors, the difficulties of the navigation in urban environment, the requirements of pedestrian and vehicular navigation.

Then an overview on the previous work related to the research topic and their limitations is provided.

Then the objective of this research is discussed, i.e. investigating the performance of the integration of GNSS systems and INS low-cost sensors in urban navigation.

Finally the outline of this thesis is provided.

1.1 Background

Nowadays the global satellite navigation systems (GNSS) play a fundamental role in many areas as civil aviation, maritime and land navigation or geomatics, owing to the ability to provide worldwide, tridimensional, all weather position, velocity and time synchronization.

At this time GPS system is the more widespread GNSS system and the only fully operational; its main quality is the ability to provide position (besides velocity and time synchronization) with time-invariant accuracy (Lachapelle 1997); the attainable accuracy varies from meter to centimeter level, depending on the observables and methods employed (Petovello 2003). The best performance can be obtained with carrier phase observable and differential techniques, involving two or more receivers; a radio modem is necessary to link the receivers in case of real-time positioning.

A real-time positioning, without requiring extra infrastructure (other receivers or radio modem) can be achieved using pseudorange observable in single point mode, yielding an accuracy of about 10 meters in good visibility condition (Conley et al. 2006).

A drawback of GPS in general is the necessity to have a good light-of-sight visibility to the satellites. Signal-degraded environments as urban areas are critical locations for satellite navigation; buildings block many of the signals, thus reducing satellite availability and weakening observation geometry, with the extreme case being solution unavailability. Buildings can also reflect the signals causing multipath phenomenon, introducing large measurement errors. For these reasons, standalone GPS is not adequate to guarantee a continuous and accurate navigation in urban environment.

In these scenarios GPS system must be augmented with other sensors to allow an accurate and continuous navigation.

The recent enhancement of GLONASS satellite system suggests the combined use with GPS in order to increase the satellite availability, especially in places with lack of GPS signals; also GLONASS measurements are affected by blocking and multipath problems in urban areas.

Inertial sensors are well suited for integration with GNSS systems owing to their complementary features.

Unlike GNSS systems, the inertial navigation systems (INS) are self-contained and their performance is not degraded in environment as urban canyons, being independent of external electro-magnetic signals. Moreover INS are more accurate in the short term and they can supply data continuously with very high rate (at several hundred Hz, whereas GNSS receivers typically updates position and velocity at 1 to 20 Hz); INS can also provide attitude information.

The main drawback of an INS is the degradation of its performance with time; in order to bound the errors to an acceptable level, regular updates are necessary and GNSS measurements can be used to this purpose.

A common configuration includes a GPS receiver and an high-end INS, able to provide navigation solution during GPS gaps; the use of high-end INS is generally confined to only high accuracy navigation and geo-referencing applications, owing to their price and size.

The recent advances in MEMS technology has made possible the development of a generation of low cost inertial sensors, characterized by small size and light weight which represent an attractive option for commercial applications as pedestrian and vehicular navigation. MEMS-based INS are characterized by low performance too, so their use as part of an integrated navigation system is currently under investigation.

This dissertation investigates the integration of MEMS INS with GNSS systems in pedestrian and vehicular navigation in urban environment; the GPS and GLONASS measurements are employed and processed in single point mode.

Pedestrian and vehicular navigation, and in general land navigation, are often related to the LBS (Location-Based Services), i.e. the information or entertainment services, accessible with mobile devices, based on the ability to determine the position of the mobile device (De Agostino 2010); the requirements of a service depend on how critical it is and can vary from 100 meters (for commercial purpose) to few meters for emergency service.

1.2 Previous Work and Limitations

The main topic discussed in this dissertation is the integration of GNSS and INS systems.

Several researchers have investigated this topic considering high-end inertial sensors, e.g. a navigation-grade inertial system is adopted in El-Sheimy et al. (1995) and Grejner-Brzezinska et al. (1998), and a tactical-grade INS is adopted in Petovello (2003) and Nassar (2003). The use of high-end INS allows a sub-metric position accuracy level during GPS outages and is generally confined to only technical high-accuracy applications, owing to their price and size.

In the last few years, several researchers have investigated the integration of GNSS systems with MEMS-based INS, characterized by low cost and low performance, for instance Nayak (2000), Shin (2005), Mezentsev (2005), Abdel-Hamid (2005), Godha (2006).

Nayak (2000) investigated the feasibility of using multiple antennas to isolate and detect multipath on pseudoranges, and the integration of differential GPS (DGPS) and a low cost IMU for navigation in an urban vehicular environment. Shin (2005) focused on the use of the unscented Kalman filter to develop a low cost INS aided by DGPS measurements. Abdel-Hamid’s research (2005) aims at enhancing the accuracy of an integrated system DGPS/INS(MEMS) in land vehicular navigation, using fuzzy logic based techniques. Godha (2006) evaluated the performance of the integration between DGPS and MEMS-INS, using single differenced pseudorange and Doppler observables in vehicular navigation. Shin (2005) and Godha (2006) proposed also the use of post-mission smoothing techniques.

All the above-mentioned researchers have focused their work on the use of GPS system in differential mode; this involves the deployment of a base station not far from the area where the navigation takes place and, in case of real-time application, a radio-modem linking the base and the rover must be included too. The need of the mentioned surplus equipment can be considered an important limitation of these works.

This research investigates the performance of an integrated system GPS/INS(MEMS), with GPS working in single point mode.

Since the beginning of 2003, the Russian government started to restoring the GLONASS system, which at November 11th 2010 includes 20 operating satellites.

The recent enhancement of GLONASS satellite system suggests the combined use with GPS in order to increase the satellite availability; this can be especially useful in places with lack of GPS signals.

The benefits of a combined use of GPS and GLONASS systems in terms of reliability, accuracy, availability and integrity is pointed out in Cai and Gao (2009) and Angrisano et al. (2009a); the benefits in urban vehicular navigation is demonstrated in Angrisano et al. (2010).

Hence in this research, the benefits of GLONASS measurements in the considered integrated system are investigated.

In Sukkarieh (2000) and Shin (2001), it is proposed the use of motion constraints to bound the INS errors during GPS outages. The motion constraints are applied to vehicular navigation case and are based on the assumptions that the vehicle does not slip and always remains in contact with the ground and so the velocity of the vehicle in the plane perpendicular to the forward direction is approximately zero. In Sukkarieh (2000) the effectiveness of velocity constraints is demonstrated with a medium accuracy IMU; Shin (2001) used the velocity constraints to bound the errors in a tactical grade IMU. Godha (2006) adopted, in addition to the velocity constraints, an height constraint, based on the assumption that the height solution does not typically vary by more than few tens of meters in a small region; Godha (2006) demonstrated the motion constraint effectiveness with a MEMS IMU in vehicular application. Also in Klein et al. (2010) the knowledge of the vehicle’s behavior is used to generate pseudo-measurements aiding the estimation process.

This research investigates the effectiveness of the motion constrains in pedestrian navigation too, suitably increasing the constraint uncertainty with respect to the vehicular case.

1.3 Objectives

This dissertation investigates the performance of an integrated system consisting of a GNSS receiver and a low-cost MEMS-based INS; the considered GNSS systems are GPS and GLONASS, whose pseudorange and Doppler observables are processed in single point mode (real-time algorithms are adopted). The INS system is implemented in the strapdown configuration and the extended Kalman filter is used to merge inertial and GNSS information, in loose or tight architecture. The inertial sensor errors are modeled by biases and scale factors, which are estimated in the Kalman filter and feedback to the sensor to limit the error growth (implementing a closed loop strategy).

The velocity and height motion constraints are introduced to bound the INS errors during GNSS outages.

The specific objectives of this thesis are:

- To analyze the performance of GPS/INS system with loosely and tightly coupled architectures. The GPS/INS system (without further aiding) represents the basic configuration to evaluate the loose and tight strategies; tight architecture is usually preferred in environments with lack of GPS signals (as urban scenario), owing to its ability to carry out integrated solution in case of GPS partial outages. In open sky condition the two architecture usually provide similar results.
- To investigate the performance improvements when GLONASS measurements are included. The GPS/GLONASS/INS (GNSS/INS) system performance is analyzed in loose and tight integration to assess the benefits of including GLONASS and evaluate if the GLONASS inclusion can change the role of loosely coupling in urban navigation.
- To evaluate the performance of the integrated systems GPS/INS and GNSS/INS in different operating environments as open sky, urban canyon, severe urban canyon.
- To analyze the integrated systems in vehicular and pedestrian navigation in the considered operating scenarios.
- To investigate the performance improvements when the integrated system is aided by velocity and height motion constraints. This aided configuration is compared with other configurations and the effectiveness of the constraint aiding is evaluated in both pedestrian and vehicular contexts.

1.4 Thesis Outline

Chapter 2 provides an overview on the navigations systems involved in this research.

First GPS and GLONASS systems are reviewed with emphasis on their similarities and differences and on the single point positioning.

Next inertial navigation systems are introduced, focusing on the main equations involved and on the errors limiting their accuracy.

Chapter 3 provides an overview about the estimation methods used in this research, i.e. Kalman Filter and Least Square method.
In the second part of the chapter the reliability testing and the blunder detections strategies are briefly reviewed.

Chapter 4 provides a review of the GNSS measurement models for single point positioning, using pseudorange and Doppler observables.
First the algorithms for PVT (Position-Velocity-Time) estimation are explained in case of GPS only. Subsequently the GPS/GLONASS combined algorithms are introduced.

In Chapter 5 the main aspects of the GNSS/INS integration are reviewed.
The loosely and tightly coupled architectures are discussed and compared. Afterwards an algorithm for the direct observation of azimuth is reported and the use of constraints to bound the INS error during GNSS outages is introduced.

Chapter 6 describes some tests carried out with details about the adopted equipment, the operational environment and the implemented algorithms.
The considered scenarios are the pedestrian and the vehicular navigation in urban canyon context. The results obtained are compared with a reference solution achieved using an higher grade inertial sensor and post-processing procedures.

Chapter 7 summarizes the work presented in this thesis and draw conclusions from the test results described in Chapter 6.

Chapter 2 Systems Overview

This Chapter discusses the navigations systems involved in this research.

First the main Global Navigation Satellite Systems (GNSS), GPS and GLONASS, are reviewed with emphasis on the single point positioning and the resulting accuracy. The similarities and the differences between the systems are made clear as is the benefit of their joint use.

Next inertial navigation systems are introduced, focusing on the main equations involved and on the errors limiting their accuracy. Some details are provided about MEMS low-cost sensors and their performance.

2.1 GPS Overview

Global Positioning System (GPS) is a worldwide, all-weather positioning system able to provide tri-dimensional position and time synchronization to UTC scale.

GPS positioning is based on the one-way ranging technique: the time of travel of a signal transmitted by satellites is measured and scaled by speed of light to obtain the satellite-user distance.

To measure the time of travel of the signal both satellite and receiver are equipped with clocks and a ranging signal is broadcast by satellite; the ranging signal is a particular code in which is embedded a timing information that enables the receiver to compute when the signal left the satellite according to the satellite clock (Kaplan and Leva 2006).

In ideal conditions satellite and receiver clocks are synchronized and the time of travel, multiplied by light speed, provides the true range satellite-receiver; in this case the user position would belong to the spherical surface centered in the satellite position (at the transmission epoch) and with radius equal to the true range. Thus three simultaneous range measurements define three spherical surfaces, whose intersection would allow coordinates determination.

Actually satellites and receiver clock are not synchronized, generating errors in the measured distances (also other error sources affect the measurements, but they are negligible with respect to the error due to non-synchronization); so the measured range is not equal to the true range and is denoted as pseudorange (Kaplan and Leva 2006).

At least four simultaneous measurements are necessary to compute user position, because a further unknown, representing the receiver clock bias, has to be included (more details are given in the section 2.1.2).

2.1.1 GPS Structure

The GPS system consists of three segments: the space segment, the control segment and the user segment.

The space segment consists of a constellation of artificial satellites. The GPS constellation is defined as an “Expandable 24-Slot” constellation (GPS SPS Performance Standard 2008). A slot is a defined location, containing at least one operational satellite; 24 slots are placed on six orbital planes, with four slots per plane. Three slots are expandable, i.e. can be occupied by two satellites in backward and forward locations with respect to the pre-defined slot location. Satellites without a pre-defined slot are considered “surplus” satellites; surplus satellites are recently launched waiting to be moved into a slot or old satellites in the last period of their operative life (the last case is really common because so far the GPS satellites had longer operative life than expected) (GPS SPS Performance Standard 2008).

The GPS space segment at November 11th 2010 includes 30 operating satellites (ftp://tycho.usno.navy.mil/pub/gps/gpstd.txt).

The right ascensions of the adjacent ascending nodes are spaced 60°, the orbits are almost circular with an inclination of about 55° and an average altitude of 20200 km; the orbital period is one-half sidereal day so that the ground traces repeat each sidereal day.

The GPS satellites are able to receive signals from control segment and other satellites and can broadcast signals to the control and user segments; they are equipped with micro-processor to process data and they are able to perform maneuvers guided by the control segment. Moreover satellites are equipped with atomic clocks, able to keep time with great precision with frequency stability on the order of 10^{-14} (Spilker 1996a).

The Control Segment (CS) consists of the Master Control Station (MCS), L-band Monitor Stations (MS) and S-band Ground Antennas (GA). MCS tasks include estimation of satellite ephemeris and clock parameters, starting from information stored by MS, generation of navigation message, maintaining of GPS time and synchronization to Universal Time Coordinate (UTC) as maintained by US Naval Observatory (USNO), and commanding satellite maneuvers to keep the nominal orbits. MS tasks include navigation signal tracking, range and carrier measurement and atmospheric data collection. The job of the GA is to transmit satellite commands and to perform satellite navigation upload (Dorsey et al 2006).

The user segment is made up of all the system users, equipped with a GPS receiver-processor able to receive and decode the GPS signal to obtain position/velocity/time information.

GPS satellites broadcast signals on two carrier frequencies: L1 (1575.42 MHz) and L2 (1227.60 MHz). These carriers are modulated by two kinds of Pseudo-Random-Noise (PRN) codes, the Coarse-Acquisition (C/A) code with a 1.023 MHz chip-rate and a period of one millisecond, and the Precise (P) code with a 10.23 MHz chip-rate and a period of seven days. The C/A code is available on the L1 carrier only and the Precise (P) code on both L1 and L2.

Since 2000 the US government started a modernization of GPS including the broadcast of new signals for civil and military use (Ward et al 2006).

The PRN codes are binary signals having spectral characteristics similar to random sequences, but which are actually deterministic (Ward et al 2006). GPS system uses the Code Division Multiple Access (CDMA), i.e. all satellites use the same frequencies and each satellite transmits a different PRN code, so that at the receiver level it is possible to distinguish between tracked satellites.

PRN codes are also called “ranging codes”, because the comparison between the received PRN code and its replica generated inside the receiver allows the estimation of the propagation interval of the signal from the satellite to the user (and hence the pseudo-range).

The C/A code is for civil use, it can be used by every user equipped with a GPS receiver/processor and its use is associated with Standard Positioning Service (SPS). The P code instead is for military purpose, its access is restricted to authorized users only (using encrypting techniques) and its use is associated with Precise Positioning Service (PPS). The need of two frequencies to accurately compensate for ionospheric delay has motivated the development of techniques to obtain L2 P code pseudorange and carrier-phase measurements without the cryptographic knowledge for full access to this signal. These techniques are referred to as either codeless or semicodeless techniques (Ward et al 2006).

In addition to the ranging codes, the carries are also modulated by the navigation message, a 50 Hz signal providing all the information necessary to compute the precise location of the satellites and to correct the satellite clock errors.

The GPS modernization adds to the existing signals three new civil signals: the L2C civil signal allowing ionospheric correction along with L1 C/A signal in civil applications, the L5 signal on the new carrier 1176.45 MHz designed for aviation safety applications, and the L1C signal designed to enable interoperability with Galileo and other GNSS systems (Wang 2010). Also the military code M is added to both L1 and L2 (Ward et al 2006).

2.1.2 GPS Observables

GPS civil receivers can generate three types of measurements: pseudorange (PR) measurements, phase measurements and Doppler measurements.

The Pseudorange measurement is obtained using the ranging code C/A and represents the time necessary for the signal to travel from the satellite to the receiver, scaled by the light speed. The PR is obtained using correlation between the received PRN-code and a replica generated inside the receiver; the measured shift between the two signals anyway contains clock biases (hence the term “pseudo”), because the received signal is marked by the satellite time and the local signal is referred to the receiver clock. Formula (2-1) shows the expression of the true PR, i.e. the pseudorange in ideal error-free condition including only clock biases.

$$PR_{true} = d + c\delta t_S - c\delta t_R \tag{2-1}$$

where

PR_{true} is the true PR (m)

d is the true range satellite-receiver (m)

$c\delta t_S$ is the satellite clock bias relative to the GPS time (s)

$c\delta t_R$ is the receiver clock bias relative to the GPS time (s)

c is the speed of light (m/s)

Actually the PR measurement includes also other kind of error, as shown in formula (2-2):

$$PR = d + c\delta t_S - c\delta t_R + \delta d_{orb} + \delta d_{iono} + \delta d_{tropo} + \delta d_{multi} + \eta \tag{2-2}$$

where

PR is the measured PR (m)

δd_{orb} is the orbital error (m)

δd_{iono} is the ionospheric error (m)

δd_{tropo} is the tropospheric error (m)

δd_{multi} is the multipath error (m)

η is the error caused by the noise in the receiver (m)

and the other terms meaning is the same of the previous formula.

In single point positioning, the operational mode investigated in this work, all the error terms are modeled or neglected leaving four unknowns: the three receiver coordinates, included in the *d* term, and the receiver clock bias $c\delta t_R$. So at least four simultaneous visible satellites are necessary to compute the user position, solving the system of equations (2-2), linearized around an approximate solution, using Kalman Filter or Least Square method.

The position accuracy obtainable in good visibility condition for a single point mode is about 10 meters (Conley et al. 2006).

Phase measurement is obtained using the carrier phase (L1 or L2) and is the (accumulated) phase of the beat frequency generated by the difference of the incoming and local carriers. The phase measurement, multiplied by the carrier wavelength, represents the satellite–receiver range with the ambiguity of an integer number of wavelength. The phase measurement equation is:

$$\lambda \cdot \phi = d + c\delta t_S - c\delta t_R + \lambda \cdot N + \delta d_{orb} - \delta d_{iono} + \delta d_{tropo} + \delta d_{multi} + \eta \qquad (2\text{-}3)$$

where

λ is the wavelength of the carrier

ϕ is the phase measurement

N is the number of cycles in the satellite–receiver distance

and the other terms are as previously defined.

The phase measurement is inherently more precise than the code measurement (Wells et al 1987), with more than two orders of magnitude less noise (Ward et al. 2006).

A meaningful difference between phase and pseudorange measurements is that the phase observable includes the unknown number of carrier cycles between the satellite and the receiver, which usually cannot be determined in stand-alone navigation (Axelrad and Brown 1996). However this measurement is used for precise differential interferometric GPS applications, such as static and kinematic surveying or for attitude determination (Ward et al. 2006).

An exception is the Precise Point Positioning (PPP) technique, which uses both code and carrier phase measurements in single point mode and precise satellite orbit and clock products (e.g. from IGS), obtaining accuracies of decimeter (Kouba and Héroux 2001).

The Doppler measurement is the derivative of the carrier phase and represents the frequency shift caused by the relative receiver-satellite motion. It is generally measured in carrier cycles per seconds (Hz) and, when multiplied with the carrier wavelength, represents the derivative of the satellite-receiver range and thus can be used to compute the user velocity (considering known the satellite motion). The Doppler measurement equation is obtained by taking the derivative of equation (2-3):

$$P\dot{R} = \dot{d} + c\delta\dot{t}_S - c\delta\dot{t}_R + \delta\dot{d}_{orb} - \delta\dot{d}_{iono} + \delta\dot{d}_{tropo} + \delta\dot{d}_{multi} + \dot{\eta} \tag{2-4}$$

where:

$P\dot{R}$ is the measured range derivative, from Doppler measurement (m/s)

$\dot{d}$ is the satellite-receiver distance rate (m/s)

$c\delta\dot{t}_S$ is the satellite clock drift (m/s)

$c\delta\dot{t}_R$ is the receiver clock drift (m/s)

$\delta\dot{d}_{orb}$ is the orbit error drift (m/s)

$\delta\dot{d}_{iono}$ is the ionospheric error drift (m/s)

$\delta\dot{d}_{tropo}$ is the tropospheric error drift (m/s)

$\delta\dot{d}_{multi}$ is the multipath error drift (m/s)

$\dot{\eta}$ is the error drift of the noise in the receiver (m/s).

The velocity accuracy obtainable using the Doppler measurements is in the order of some centimeter per second (Hoffmann-Wellenhof 1992); this good accuracy level is connected to the small amount of the errors in equation (2-4), indeed these errors are derivatives of the orbital, propagation (atmospheric and multipath) and noise errors.

2.1.3 GPS Errors

The errors corrupting the GPS performance are described below; a more extensive treatment is in Conley et al 2006 and Parkinson 1996.

The satellite clock error is the offset between the time maintained by the atomic clocks on the satellite and the reference GPS time. The MCS computes and broadcasts to the users the parameters to correct the satellite clock error, according to the equation (IS-GPS-200 2004):

$$\delta t_{sat} = a_{f0} + a_{f1} \cdot (t - t_{oc}) + a_{f2} \cdot (t - t_{oc})^2 + \Delta t_{rel} \tag{2-5}$$

where:

a_{f0} is the clock bias (s)

a_{f1} is the clock drift (s/s)

a_{f2} is the frequency drift (s/s^2)

t_{oc} is the clock parameters reference epoch (s)

t is the current epoch (s)

Δt_{rel} is the relativistic correction (s)

The relativistic correction is caused by the slight eccentricity of the satellite orbits, bringing a periodic change in the satellite gravitational potential and in the satellite speed in the inertial frame (Conley et al 2006). The relativistic correction is expressed by the formula:

$$\Delta t_{rel} = F \cdot ecc \cdot \sqrt{a} \cdot \sin(E) \tag{2-6}$$

where

$F = -4.442807633 \cdot 10^{-10} s / m^{1/2}$

ecc is the orbit eccentricity

$\sqrt{a}$ is the square root of the orbital semi-major axis

E is the eccentric anomaly of the satellite

The residual satellite clock error, after the application of (2-5), vary from 0.3-4 m RMS of equivalent range error, depending on the satellite generation and correction parameters age (Conley et al 2006).

The receiver clock error is the difference between the time maintained by the receiver clock and the reference GPS time. The receiver clock error is typically modeled with two states representing a bias and a drift error, indicating the presence of a frequency error (Brown and Hwang 1997).
The receiver clock bias is a time-varying error that affects all the range measurements in the same amount for a fixed epoch and is included as an unknown in the single point positioning mode (section 4.1). The receiver clock drift affects the Doppler measurement (Kaplan and Leva 2006) and is included as an unknown in the Doppler measurement models as shown in section 4.2.

The orbital error is the difference between the computed and the actual satellite position. The computed position is estimated by the MCS using data collected by MS, is upload to the satellite and is broadcasted to the users in the navigation message. The orbital error has three components: along-track, cross-track and radial. The range error is essentially related to the radial component. The accuracy of the computed satellite position is related to the age of the estimations and is on the order of 0.8 m RMS (Conley et al. 2006).

The ionospheric error is the measurement error caused by the propagation of the GPS signals in the ionosphere. The ionosphere is the region of the atmosphere between about 70 km and 1000 km above the Earth surface. Within this region sun radiation ionizes a portion of the gas, producing free electrons and ions; a signal travels through the ionosphere with a speed different from the speed of light. In the GPS case, the code and so the PR are delayed and the carrier phase is advanced. The ionosphere is a dispersive medium, i.e. the propagation speed depends on the carrier frequency, so the ionospheric delay can be eliminated using dual frequency receivers. In this work only single frequency solutions are considered and in this case the ionospheric error can be reduced using suitable models, the most common being the Klobuchar model (Klobuchar 1996) which removes about 50% of ionospheric error on average and whose coefficients are broadcasted in the navigation message. The ionospheric residual error after the Klobuchar model is on order of 7 m RMS (Conley et al. 2006).

The troposphere is the lower atmosphere layer, from the Earth's surface to 50 km. The troposphere yields a variation in the wave propagation with respect to vacuum. It can be considered a non-dispersive medium for frequency up to 15 GHz, so the delay is independent from the carrier frequency. In GPS case both PR and carrier phase will experiment the same delay and dual-frequency receivers cannot be used to eliminate it. The tropospheric delay is a function of the temperature, pressure and humidity. The tropospheric error is typically broken in two components: a dry component, including about 90% of the error and highly predictable, and a wet component, including about 10% of the error and more difficult to predict. Several models can be used to reduce the influence of the tropospheric error, bringing sub-meter accuracy (Spilker 1996b). In this study the Hopfield model is used.

The multipath error is caused by the arrival at the receiver of the signal via multiple paths because of the reflections during the signal propagation (Parkinson 1996). The multipath error can be the dominant error in some scenarios like urban environment. Both code and carrier phase are affected by multipath phenomenon, but in different ways. Code multipath can vary from few meters in benign environments to over one hundred meters in strongly reflective scenarios (Parkinson 1996) and can be much greater in situations where only the echoes are received (Mezentsev 2005). Carrier phase multipath is generally much smaller, of centimeter order. Because the Doppler measurements is the derivative of the carrier phase measurement, the multipath effect on the velocity estimation is very small (Godha 2006).

The receiver noise error includes the thermal noise and the receiver hardware effects. Typical errors for code measurement are of few decimeters order and negligible for carrier phase measurement (Conley et al. 2006).

2.2 GLONASS Overview

GLONASS system has an operational principle similar to GPS system: the user equipment is able to measure pseudo-ranges and pseudo-range rates with respect to space vehicles, and uses this information to compute the position, velocity and for synchronization with a reference time scale. As with GPS, GLONASS also consists of space segment, control segment and user segment.

The space segment is a constellation of nominally 24 artificial satellites placed in three orbital planes whose ascending nodes are 120° apart. Theoretically 8 satellites are equally displaced on each plane, with a displacement of argument of latitude among the planes of 15°. The orbits are planned to be circular with an inclination of 64.8° and a radius of 19100 km, corresponding to an orbital period of 11^h15^m with ground tracks repeating every 17 orbital periods. The satellite constellation, if completely deployed, would provide a continuous and worldwide coverage for users on the Earth surface or in the near-Earth space (ICD-GLONASS 2008). The GLONASS space segment at November 11th 2010 includes 20 operating satellites, 4 in maintenance and 2 spares. Currently the "Glonass-M" generation of satellites are in orbit (www.glonass-ianc.rsa.ru).

The control segment consists of a System Control Center and a network of command and tracking stations deployed in the Russian territory, and is responsible for the determination and the upload of the satellite orbits and for monitoring satellite clock and health.

The user segment is the ensemble of all the users equipped with a GLONASS receiver/processor able to receive the GLONASS signals and to process the received information to obtain position, velocity and time synchronization with UTC reference time.

The Glonass-M satellites transmit signals on two frequency bands: L1 ~ 1.6 GHz and L2 ~ 1.25 GHz. On both the bands, the carriers are modulated by two ranging codes, one associated to a standard positioning service (ST) accessible to all the users and another associated to a precise positioning service (VT) restricted to authorized users only. The ranging code associated to the ST has a 511 kHz chip-rate and a period of one millisecond, the code associated to the VT has 5.11 MHz chip-rate. In this work only the ST is considered. Both carriers are modulated by signal storing the navigation message.

Unlike GPS, the GLONASS system uses the Frequency Division Multiple Access (FDMA) technique, i.e. each satellite transmits on carriers with different frequencies and the frequency plan is:

$$
\begin{aligned}
f_{K1} &= f_{01} + K \cdot \Delta f_1 \\
f_{K2} &= f_{02} + K \cdot \Delta f_2
\end{aligned}
\tag{2-7}
$$

where:

f_{K1} is the frequency of the Kth satellite on the sub-band L1,

f_{K2} is the frequency of the Kth satellite on the sub-band L2,

f_{01} is the central frequency of the L1 sub-band and is 1602 MHz,

f_{02} is the central frequency of the L2 sub-band and is 1246 MHz,

K is the frequency channel and is an integer number from -7 to +6,

Δf_1 is the frequency increment for the sub-band L1 and is 562.5 KHz and

Δf_2 is the frequency increment for the sub-band L2 and is 437.5 KHz.

Hence at the receiver level, GLONASS satellites can be distinguished by the frequency; GLONASS satellites on the same orbit and in antipodal positions can transmit carries at the same frequency.

In addition to the ranging codes the carriers are modulated by the navigation message.

The navigation message includes immediate and non-immediate information. The immediate data are related to the satellite broadcasting the signal and include the satellite ephemeris and the parameters for the on-board clock correction. The non-immediate data are related to the whole constellation and include the coarse constellation ephemeris and clock corrections, the constellation status and correction to convert GLONASS system time to UTC scale.

2.2.1 GPS-GLONASS Differences

Although GPS and GLONASS are very similar, there are several meaningful differences, which can be classified in three categories: constellation differences, signal differences and reference differences (Cai 2009).

About the GPS and GLONASS constellations, the nominal number of satellites is 24 for both, but GPS constellation provides for the eventuality of surplus satellites with no pre-defined slots. The orbital planes are 6 for GPS and 3 for GLONASS; the GLONASS orbits are lower than GPS ones, and are more inclined, allowing a better coverage at high latitudes. The GLONASS satellites orbital period is shorter than GPS one, with ground tracks repeating every 8 sidereal days for the first and every day for the second.

Moreover GLONASS constellation has a “symmetric” configuration, i.e. the 24 slots are uniformly distributed on the three orbital planes; the slots on each plane are evenly spaced and the argument of latitude displacement between the planes is constant (the GLONASS constellation is referred to as Walker constellation). On the other hand GPS constellation is intentionally “asymmetric”: the number of satellites on the planes can be different owing to the surplus satellites and the satellites are unevenly distributed on the orbit, in order to optimize the constellation coverage in case of one satellite outage (Spilker 1996c).

About the signal, all the GPS satellites broadcast signals at the same carrier frequencies L1 and L2, while GLONASS satellites use different carrier frequency on each satellite. So GPS and GLONASS system use different multiple access schemes: CDMA for GPS (the transmitting satellites are distinguished by the code) and FDMA for GLONASS (the transmitting satellites are distinguished by the frequency). The next generation of GLONASS satellites (Glonass-K) is planned to implement the CDMA strategy to improve the compatibility with GPS (Cai 2009).

In addition the chip rate of the C/A and P codes of GLONASS is about half of the corresponding GPS codes. The chip width, defined as the inverse of the chip rate, is related with the receiver high-frequency error. For typical receivers, the standard deviation of this error is about 1/100 of the chip width, corresponding to about 3 m and 0.3 m for GPS C/A and P codes, and to about 6 m and 0.6 m for GLONASS C/A and P codes (Axelrad and Brown 1996).

Moreover the satellite broadcast ephemerides stored in the GPS navigation message are Keplerian parameters and are transformed in Earth Centered Earth Fixed (ECEF) frame using the orbital propagation algorithm (IS-GPS-200 2004); the satellite broadcast ephemerides in GLONASS navigation message are directly expressed in ECEF frame (ICD-GLONASS 2008), but anyway a propagation algorithm is necessary to compute the satellite position in the desired epoch (usually the epoch of transmission of the signal). The detailed orbital algorithms are described in section 4.3.

GPS and GLONASS systems adopt different coordinate frames to express the satellite and user coordinates: WGS84 for GPS and PZ90 for GLONASS. All the details, geodetic constants and parameters of WGS84 and PZ90 are in IS-GPS-200 2004 and ICD-GLONASS 2008. The two reference frames are nearly coincident, but the combination of measurements from both the system requires a transformation between the frames; neglecting this transformation yields an position error from a single receiver of metric order (Misra et al. 1998). In general, the transformation WGS84 – PZ90 is performed using a seven-parameters transformation, including a rotation, a translation and a scale factor. Starting from September 20 2007, an improved version of the GLONASS reference frame is in use, called PZ90.02; WGS84 – PZ90.02 transformation requires only a shift as shown in formula (2-8):

$$\begin{pmatrix} X \\ Y \\ Z \end{pmatrix}_{WGS84} = \begin{pmatrix} X \\ Y \\ Z \end{pmatrix}_{PZ90.02} + \begin{pmatrix} \Delta X \\ \Delta Y \\ \Delta Z \end{pmatrix} \tag{2-8}$$

with $\Delta X = -36cm$, $\Delta Y = +8cm$, $\Delta Z = +18cm$ (Revnivykh 2007).

GPS and GLONASS systems adopt different reference time scales, which are connected with different realizations of Universal Time Coordinated (UTC).

In detail GPS time is connected with UTC(USNO), the UTC maintained by US Naval Observatory; GPS time and UTC(USNO) are different because UTC scale is occasionally adjusted of one second to keep it close to the mean solar time (connected to the astronomical definition of time). GPS time scale is indeed continuous and so there is a difference of an integer number of seconds (called leap seconds) between GPS time scale and UTC(USNO) (currently the leap seconds are 15). Moreover GPS time and UTC(USNO) are maintained by different master clocks, producing a further difference of typically less than 100 ns; this difference is broadcast to the users in the navigation message.

GLONASS time scale is connected to UTC(RU), the UTC as maintained by Russia. GLONASS time is adjusted by leap seconds, according to the UTC adjustments, so there is no integer number of seconds between the GLONASS and UTC(RU) scales, only a difference less than 1 millisecond exists and is broadcasted in the GLONASS navigation message.

The transformation between GPS and GLONASS times is expressed by the following formula (Cai 2009):

$$t_{GPS} = t_{GLO} + \tau_c + \tau_u + \tau_g \tag{2-9}$$

with:

$\tau_c = t_{UTC(RU)} - t_{GLO}$ broadcasted in the GLONASS navigation message

$\tau_u = t_{UTC(USNO)} - t_{UTC(RU)}$ to be estimated

$\tau_g = t_{GPS} - t_{UTC(USNO)}$ broadcasted in the GPS navigation message

To perform the transformation (2-9), the difference between UTC(USNO) and UTC(RU) should be known, but this information nowadays is not provided in real-time; this problem is generally solved (also in this work) including the difference between the systems time scales as unknown when GPS and GLONASS measurements are used together.

The comparison between GPS and GLONASS systems is summarized in Table 2-1.

Table 2-1 – Comparison between GPS and GLONASS (adapted by Cai 2009)

		GPS	GLONASS
Constellation	Number of Satellites	24+surplus	24
	Orbital Planes	6	3
	Orbit Altitude	20200 Km	19100 Km
	Orbit Inclination	55°	64.8°
	Ground Track Period	1 Sidereal Day	8 Sidereal Days
	Layout	Asymmetric	Symmetric
Signal	Carrier Frequency	1575.42 MHz 1227.60 MHz	1602+K*0.5625 MHz 1246+K*0.4375 MHz
	Ranging Code Frequency	C/A: 1.023 MHz P: 10.23 MHz	C/A: 0.511 MHz P: 5.11 MHz
	Multiple Access Scheme	CDMA	FDMA
	Broadcast Ephemeredes	Keplerian	ECEF
Reference	Reference System	WGS84	PZ90.02
	Reference Time	GPS Time	GLONASS Time

2.3 INS Overview

In this section an overview on the inertial navigation is provided; more complete treatments are in Chatfield 1997 and El-Sheimy 2004.

An Inertial Navigation System (INS) is a combination of sensors able to determine all navigation states of a moving object, i.e. position, velocity and attitude; the ensemble of sensors is an Inertial Measurement Unit (IMU) and consists of three accelerometers and three gyroscopes mounted on an orthogonal triad. The accelerometers measure the specific force, defined in the inertial frame as:

$$\underline{f} = \underline{a} - \underline{g} \tag{2-10}$$

where

$\underline{f}$ is the specific force

$\underline{a}$ is the kinematic acceleration

$\underline{g}$ is the gravitational acceleration

To obtain the velocity of the moving object, the measured specific force should be corrected of the gravitational term, integrated once and the result added to the initial velocity. Integrating the obtained velocity and adding the initial position, yields the final position. So an INS can be considered a sophisticated Dead Reckoning (DR) system (El-Sheimy 2004). However the INS is actually more complicated because the measured specific force is expressed in a frame different from the frame in which velocity and position are usually expressed (navigation frame). For this reason the gyro triad is included in the IMU: gyros are able to measure angular rate with respect to the inertial frame, which, when integrated, provides the angular change with respect to the previous, supposed known, initial orientation. So gyros are used to transform the measured specific force in the navigation frame; the transformation can be mechanic, i.e. the IMU is physically aligned to the navigation frame (Gimbaled configuration), or analytic, i.e. the acceleration measurements are numerically transformed in the navigation frame (Strapdown configuration). Strapdown configuration is currently the more common strategy and is used in this work.

An uncompensated error in the accelerometer measurement (e.g. a bias) is integrated once introducing a linear error in velocity, which in turn integrated will introduce a quadratic error in position (El-Sheimy 2004). The presence of an uncompensated gyro error is more critical, introducing linear error in angles and in turn yielding quadratic error in velocity and cubic error in position. Thus the INS performance strongly depends on the quality of the included gyros (El-Sheimy 2004).

2.3.1 Reference Frames and Transformations

The most common reference frames are used in this work and are listed below.

An inertial frame is a non-rotating and non-accelerating frame with respect to the fixed stars. In inertial navigation the Earth Centered Inertial (ECI) frame is used and is defined as follows:

Origin: Earth's center of mass
Z^i-Axis: parallel to the Earth's spin axis
X^i-Axis: pointing to the mean vernal equinox
Y^i-Axis: orthogonal to X^i and Z^i axes to complete a right-hand frame

The ECI frame is not strictly inertial, because its origin is involved in the Earth revolution round the Sun; moreover the Earth's spin axis is involved in the precession and nutation motions, making the vernal equinox slowly move. Anyway the ECI frame is considered inertial for navigation purpose (Nastro 2004).

The Earth Centered Earth Fixed (ECEF) is a frame integral to the Earth and is defined as follows:

Origin: Earth's center of mass
Z^e-Axis: parallel to the Earth's spin axis
X^e-Axis: on the equatorial plane, pointing to the mean meridian of Greenwich
Y^e-Axis: orthogonal to X^i and Z^i axes to complete a right-hand frame.

The East-North-Up (ENU) reference is a local frame centered in the navigation system origin and defined as follows:

Origin: center of the navigation system
Z^n-Axis (or U-Axis): pointing upward along the ellipsoid normal
X^n-Axis (or E-Axis): on the horizontal plane, pointing toward geodetic East
Y^n-Axis (or N-Axis): on the horizontal plane, pointing toward geodetic North.

The ECI, ECEF and ENU frames are shown in Figure 2-1.

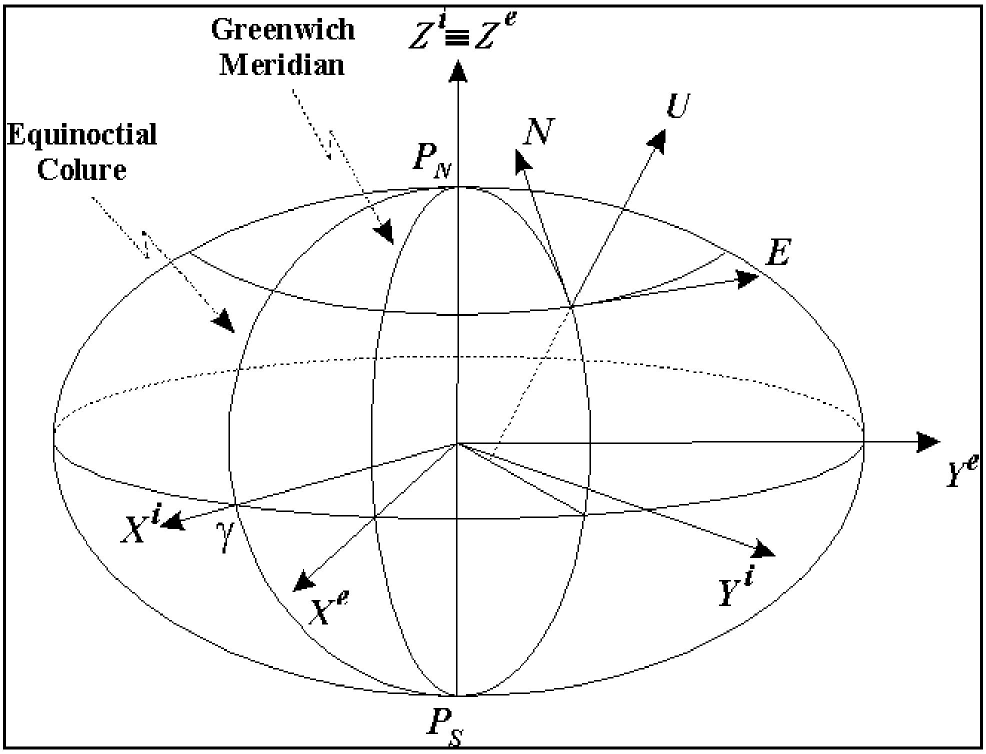

Figure 2-1 – ECI, ECEF and ENU Frames

The body frame is an orthogonal frame, whose axes are coincident with the axes of the IMU. In the gimbaled arrangement the body frame is kept aligned to the chosen navigation frame, using the gyro information and external torques. In the strapdown arrangement the IMU is rigidly mounted on the moving object to be positioned and conventionally is considered aligned with it. The body frame (Figure 2-2) in this work is defined as follows:

Origin: center of the navigation system
X^b-Axis: pointing towards the right of the moving object
Y^b-Axis: pointing towards the front of the moving object
Z^b-Axis: orthogonal to X^b and Z^b axes to complete a right-hand frame.

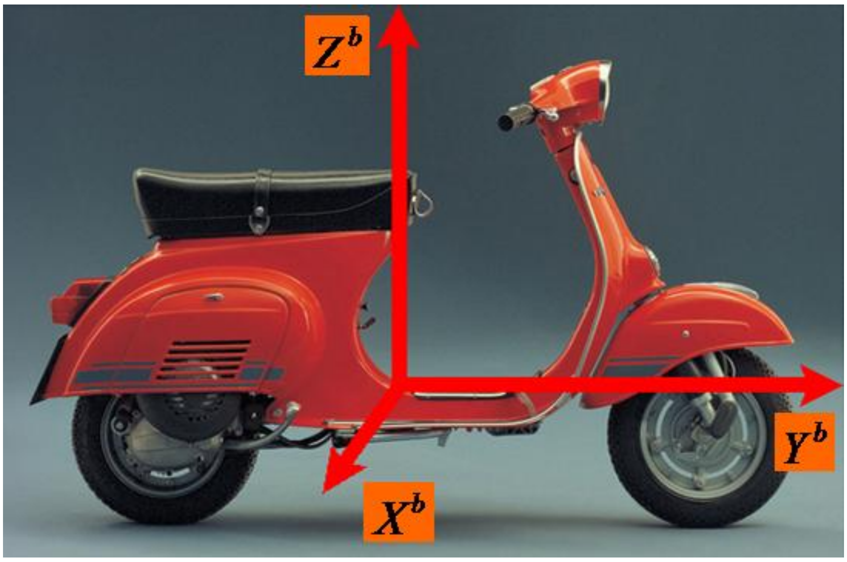

Figure 2-2 – Body Frame

The transformation between ECI and ECEF can be performed by a single rotation around Z axis (formula (2-11)), because the frames have coincident origins and Z axes.

$$\begin{pmatrix} X \\ Y \\ Z \end{pmatrix}_{ECEF} = R_z(\sigma \cdot \Delta t) \cdot \begin{pmatrix} X \\ Y \\ Z \end{pmatrix}_{ECI} \tag{2-11}$$

where:

$\sigma = 7.2921151467\mathrm{e}-5 \text{ rad/sec}$ is the Earth's rotation rate,

$\Delta t = t - t_0$ is the difference between the current epoch t and the epoch when the frames were coincident t_0 and

$R_z(\cdot)$ is a rotation matrix around the z-axis, representing an anticlockwise rotation of the amount in the parenthesis

The transformation between ECEF and ENU frames, in addition to the rotation, must include the shift, because the frames have different origins, and is expressed by the formula (2-12) (Farrell 2008):

$$\begin{pmatrix} X \\ Y \\ Z \end{pmatrix}_{ENU} = R_x(90° - \varphi) \cdot R_z(90° + \lambda) \cdot \left[\begin{pmatrix} X \\ Y \\ Z \end{pmatrix}_{ECEF} - \begin{pmatrix} X_0 \\ Y_0 \\ Z_0 \end{pmatrix}_{ECEF} \right] \tag{2-12}$$

where

φ and λ are the geodetic coordinates of the origin of the ENU frame,

$R_x(\cdot)$ and $R_z(\cdot)$ are rotation matrices around the X and Z axes, representing anticlockwise rotations of the amount in the parenthesis and

$[X_0 \quad Y_0 \quad Z_0]^T$ are the coordinates of the ENU frame origin, expressed in the ECEF frame.

In case of ECEF-ENU transformation of a velocity vector, the shift term must be omitted as showed below (Farrell 2008):

$$\begin{pmatrix} V_X \\ V_Y \\ V_Z \end{pmatrix}_{ENU} = R_x(90° - \varphi) \cdot R_z(90° + \lambda) \cdot \begin{pmatrix} V_X \\ V_Y \\ V_Z \end{pmatrix}_{ECEF} \tag{2-13}$$

where

$[V_X \quad V_Y \quad V_Z]^T_{ENU}$ are the velocity components in the ENU frame and

$[V_X \quad V_Y \quad V_Z]^T_{ECEF}$ are the velocity components in the ECEF frame.

The transformation between ENU and body frames can be performed by three consecutive rotations as shown in (2-14):

$$\begin{pmatrix} X \\ Y \\ Z \end{pmatrix}_{Body} = R_y(\phi) \cdot R_x(\theta) \cdot R_z(-\psi) \cdot \begin{pmatrix} X \\ Y \\ Z \end{pmatrix}_{ENU} \tag{2-14}$$

where:

ϕ is the roll angle of the moving object,

θ is the pitch angle,

ψ is the yaw angle and

$R_x(\cdot)$, $R_y(\cdot)$ and $R_z(\cdot)$ are rotation matrices around the X,Y and Z axes respectively.

ϕ, θ and ψ are called Euler angles. A more compact notation can be used to express the ensemble of rotations necessary to transform a point coordinates from a frame to another; the matrix necessary to transform ENU coordinates in body frame can be indicated as:

$$R_n^b = R_y(\phi)\cdot R_x(\theta)\cdot R_z(-\psi) \tag{2-15}$$

Performing the computations, equation (2-15) becomes (from Salychev 1998):

$$R_n^b = \begin{pmatrix} \cos\phi\cos\psi + \sin\phi\sin\theta\sin\psi & -\cos\phi\sin\psi + \sin\phi\sin\theta\cos\psi & -\sin\phi\cos\theta \\ \cos\theta\sin\psi & \cos\theta\cos\psi & \sin\theta \\ \sin\phi\cos\psi - \cos\phi\sin\theta\sin\psi & -\sin\phi\sin\psi - \cos\phi\sin\theta\cos\psi & \cos\phi\cos\theta \end{pmatrix} \tag{2-16}$$

and the Euler angles as functions of the elements of the rotation matrix R_{ENU}^b are computer as:

$$\begin{aligned} \phi &= -\arctan\left(\frac{R_n^b(1,3)}{R_n^b(3,3)}\right) \\ \theta &= \arcsin\left(R_n^b(2,3)\right) \\ \psi &= \arctan\left(\frac{R_n^b(2,1)}{R_n^b(2,2)}\right) \end{aligned} \tag{2-17}$$

2.3.2 Mechanization Equations

The mechanization equations are a set of equations used to obtain useful navigation information from the IMU measurements, i.e. specific force and angular rate. In this work the mechanization is implemented in ENU frame (El-Sheimy 2004) and so it is referred to as navigation frame.

The equations modeling the motion of the moving object in the ENU frame are (extensive treatment about the computations is given in Shin 2001 and El-Sheimy 2004):

$$\begin{pmatrix} \dot{\underline{r}}^n \\ \dot{\underline{V}}^n \\ \dot{R}_b^n \end{pmatrix} = \begin{pmatrix} D\cdot\underline{V}^n \\ R_b^n \underline{f}^b - \left(2\Omega_{ie}^n + \Omega_{en}^n\right)\cdot\underline{V}^n + \underline{g}^n \\ R_b^n\left(\Omega_{ib}^b - \Omega_{in}^b\right) \end{pmatrix} \tag{2-18}$$

The first equation of (2-18) represents the relationship between the geographic coordinates and the velocity components in the ENU frame:

$$\dot{\underline{r}}^n = D\cdot\underline{V}^n \tag{2-19}$$

where:

$\underline{r}^n = [\varphi \quad \lambda \quad h]^T$ is position of a mobile in the local ENU frame, expressed by the geographic coordinates latitude, longitude and altitude,

$\underline{V}^n = [V_E \quad V_N \quad V_U]^T$ is the velocity in the ENU frame, consisting of the three East, North and Up components,

D is matrix to transform velocity components to the derivative of geographic coordinates and has the expression:

$$D = \begin{pmatrix} 0 & \frac{1}{M+h} & 0 \\ \frac{1}{(N+h)\cos\varphi} & 0 & 0 \\ 0 & 0 & 1 \end{pmatrix} \tag{2-20}$$

with

M radius of curvature in the Meridian and

N radius of curvature in the Prime Vertical.

The second equation of (2-18) is the velocity mechanization equation in ENU frame:

$$\underline{\dot{V}}^n = R_b^n \underline{f}^b - \left(2\Omega_{ie}^n + \Omega_{en}^n\right) \cdot \underline{V}^n + \underline{g}^n \tag{2-21}$$

where

$\underline{\dot{V}}^n$ is the kinematic acceleration in the ENU frame,

$\Omega_{en}^n \cdot \underline{V}^n$ is the centripetal acceleration related to the motion of the ENU frame with respect to the ECEF frame,

$2\Omega_{ie}^n \cdot \underline{V}^n$ is the Coriolis acceleration,

$\underline{g}^n$ is the gravity vector, including the Gravitation term and the centripetal term related to the Earth rotation and

$\underline{f}^b$ is the specific force vector in the Body frame and is measured by the accelerometers.

The matrix Ω_{ie}^{n} is the skew-symmetric matrix of the vector $\underline{\omega}_{ie}^{n}$, rotation rate of Earth expressed in the ENU frame as:

$$\underline{\omega}_{ie}^{n} = \begin{bmatrix} 0 & \sigma\cos\varphi & \sigma\sin\varphi \end{bmatrix}^{T} \tag{2-22}$$

The matrix Ω_{en}^{n} is the skew-symmetric matrix of the vector $\underline{\omega}_{en}^{n}$, rotation rate of the ENU frame with respect to ECEF frame, expressed in the ENU frame as:

$$\underline{\omega}_{en}^{n} = \begin{bmatrix} \dfrac{-V_N}{M+h} & \dfrac{V_E}{N+h} & \dfrac{V_E\tan\varphi}{N+h} \end{bmatrix}^{T} \tag{2-23}$$

The third equation of (2-18) is the attitude mechanization equation and expresses the dynamics of the attitude of the Body frame with respect to navigation frame:

$$\dot{R}_{b}^{n} = R_{b}^{n}\left(\Omega_{ib}^{b} - \Omega_{in}^{b}\right) \tag{2-24}$$

The matrix Ω_{ib}^{b} is the skew-symmetric matrix of the vector $\underline{\omega}_{ib}^{b}$, rotation rate of the Body frame with respect to the ECI frame, expressed in the Body reference; $\underline{\omega}_{ib}^{b}$ is measured by the gyros.

The matrix Ω_{in}^{b} is the skew-symmetric matrix of the vector $\underline{\omega}_{in}^{b}$, which is the rotation rate of the navigation frame with respect to inertial frame expressed in the Body frame; $\underline{\omega}_{in}^{b}$ is computed combining $\underline{\omega}_{ie}^{n}$ and $\underline{\omega}_{en}^{n}$ from equations (2-22) and (2-23) and transforming the result in the Body frame as follows:

$$\underline{\omega}_{in}^{b} = R_{n}^{b}\cdot\left(\underline{\omega}_{ie}^{n} + \underline{\omega}_{en}^{n}\right) \tag{2-25}$$

The INS mechanization in the ENU frame is summarized in Figure 2-3.

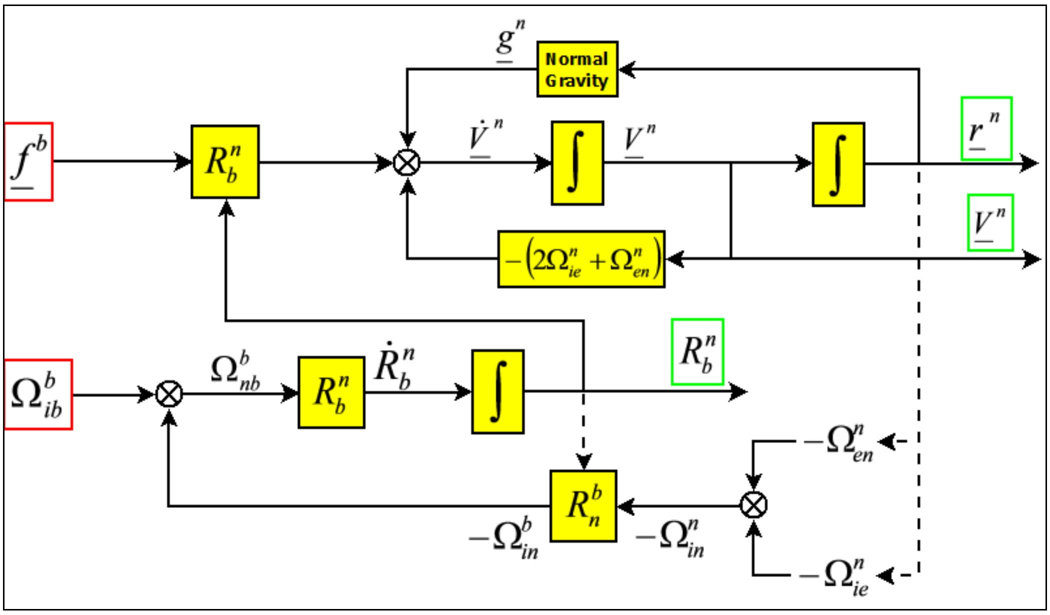

Figure 2-3 – INS Mechanization in ENU Frame (adapted from El-Sheimy 2004)

To obtain the navigation parameters from the INS measurements, the first step is using the gyro measurements to determine the orientation of the IMU with respect to the navigation frame. Gyros sense the angular rate of the IMU referred to the inertial frame, including the Earth rotation, the orientation changes of the local frame and the angular rates of the IMU; to obtain only the angular rate of the moving body, the other two components should be removed. In the equation (2-24) this correction is obtained subtracting the term Ω_{in}^b, including Earth rotation and ENU orientation changes as shown in (2-25). To determine the IMU attitude the differential equation (2-24) can be solved by integration, computing R_b^n. The more common approach (not used in this work) consists in using quaternion method (details in El-Sheimy 2004 and Chatfield 1997).

In the second step, the specific force from the accelerometers (in the Body frame) is transformed in the navigation frame using the computed rotation matrix R_b^n and is corrected for the Coriolis term, for the navigation frame change of orientation term and for the gravity (equation (2-21)). The corrected acceleration can be integrated to compute the velocity, which integrated provide the position, being known the initial values.

The IMU measurements are typically corrupted by some kind of errors like bias, scale factor and misalignment errors (the INS errors are treated in the next section and more details can be found in Chatfield 1997 and El-Sheimy 2004). The INS errors can be in part determined in laboratory calibration and in part estimated in the Kalman filter; once the errors are obtained, the measurements should be suitably corrected according to the follow equations:

$$
\begin{aligned}
f_i^b &= \frac{\tilde{f}_i^b + b_{ai}}{1 - S_{ai}} \\
\omega_i^b &= \frac{\tilde{\omega}_i^b + b_{gi}}{1 - S_{gi}}
\end{aligned}
\tag{2-26}
$$

where

the subscript *i* is referred to the axis of the sensor (*i*=x,y,z)

the symbol "~" is placed on the raw measurements

b_{ai} is the bias of the accelerometer on the axis *i*

b_{gi} is the bias of the gyro on the axis *i*

S_{ai} is the scale factor of the accelerometer on the axis *i*

S_{gi} is the scale factor of the gyro on the axis *i*

2.3.3 INS Error Dynamics

The mechanization equations (2-18) simply process inertial data from the IMU to obtain navigation parameters providing no information about the errors of the system; the estimation of the system errors is often required to improve performance to a satisfactory level and this is usually performed in a Kalman filter as showed in section 5.3.2 (Petovello 2003).

The errors of the navigation parameters are defined as:

$$
\begin{aligned}
\underline{\delta r}^n &= \underline{r}^n - \underline{\hat{r}}^n \\
\underline{\delta v}^n &= \underline{v}^n - \underline{\hat{v}}^n \\
\hat{R}_b^n &= \left(I - E^n\right) R_b^n
\end{aligned}
\tag{2-27}
$$

where

the symbol δ represents the perturbation from the nominal value,

the elements with the hat ^ are estimated quantities and without are actual quantities,

E^n is the skew-symmetric matrix of the vector of the attitude errors in the ENU frame.

It must be noticed that the error definition in (2-27) is only a convention; the opposite convention could also be adopted without loss of generality, paying attention to maintain a consistent convention throughout (Petovello 2009).

The behavior of the navigation parameter errors, i.e. the position, velocity and attitude errors, can be obtained perturbing the mechanization equations (2-18) and neglecting terms of order higher than first as (the full derivation of the equation is in El-Sheimy 2004, Shin 2001 and Yang 2008):

$$\begin{bmatrix} \underline{\delta \dot{r}}^n \\ \underline{\delta \dot{v}}^n \\ \underline{\dot{\varepsilon}}^n \end{bmatrix} = \begin{bmatrix} F_{rr} & F_{rv} & F_{r\varepsilon} \\ F_{vr} & F_{vv} & F_{v\varepsilon} \\ F_{\varepsilon r} & F_{\varepsilon v} & F_{\varepsilon\varepsilon} \end{bmatrix} \cdot \begin{bmatrix} \underline{\delta r}^n \\ \underline{\delta v}^n \\ \underline{\varepsilon}^n \end{bmatrix} + \begin{bmatrix} 0_{3x1} \\ R_b^n \underline{\delta f}^b \\ R_b^n \underline{\delta w}^b \end{bmatrix} \tag{2-28}$$

where

$\underline{\varepsilon}^n$ is the vector of the attitude errors in the ENU frame,

$\underline{\delta f}^b$ is the vector of the errors in the measured specific force,

$\underline{\delta w}^b$ is the vector of the errors in the measured angular rate,

$$F_{rr} = \begin{pmatrix} 0 & 0 & \dfrac{-V_N}{(M+h)^2} \\ \dfrac{V_E \sin\varphi}{(N+h)\cos^2\varphi} & 0 & \dfrac{-V_E}{(N+h)\cos\varphi} \\ 0 & 0 & 0 \end{pmatrix},$$

$$F_{rv} = \begin{pmatrix} 0 & \dfrac{1}{M+h} & 0 \\ \dfrac{1}{(N+h)\cos\varphi} & 0 & 0 \\ 0 & 0 & 1 \end{pmatrix},$$

$$F_{r\varepsilon} = 0_{3x3}$$

$$F_{vr}=\begin{pmatrix} 2\sigma\left(V_U\sin\varphi+V_N\cos\varphi\right)+\dfrac{V_EV_N}{\left(N+h\right)\cos^2\varphi} & 0 & \dfrac{V_EV_U}{\left(N+h\right)^2}-\dfrac{V_EV_N\tan\varphi}{\left(N+h\right)^2} \\ -2\sigma V_E\cos\varphi-\dfrac{V_E^2}{\left(N+h\right)\cos^2\varphi} & 0 & \dfrac{V_NV_U}{\left(M+h\right)^2}+\dfrac{V_E^2\tan\varphi}{\left(N+h\right)^2} \\ -2\sigma V_E\sin\varphi & 0 & -\dfrac{V_E^2}{\left(N+h\right)^2}-\dfrac{V_N^2}{\left(M+h\right)^2}+\dfrac{2g}{R+h} \end{pmatrix}$$

$$F_{vv}=\begin{pmatrix} \dfrac{V_N\tan\varphi}{N+h}-\dfrac{V_U}{N+h} & 2\sigma\sin\varphi+\dfrac{V_E\tan\varphi}{N+h} & -2\sigma\cos\varphi-\dfrac{V_E}{N+h} \\ -2\sigma\sin\varphi-\dfrac{2V_E\tan\varphi}{N+h} & -\dfrac{V_U}{M+h} & -\dfrac{V_N}{M+h} \\ 2\sigma\cos\varphi+\dfrac{2V_E}{N+h} & \dfrac{V_N}{M+h} & 0 \end{pmatrix},$$

$$F_{v\varepsilon}=\begin{pmatrix} 0 & f_U & -f_N \\ -f_U & 0 & f_E \\ f_N & -f_E & 0 \end{pmatrix}$$

$$F_{\varepsilon r}=\begin{pmatrix} 0 & 0 & -\dfrac{V_N}{\left(M+h\right)^2} \\ \sigma\sin\varphi & 0 & \dfrac{V_E}{\left(N+h\right)^2} \\ -\sigma\cos\varphi-\dfrac{V_E}{\left(N+h\right)\cos^2\varphi} & 0 & \dfrac{V_E\tan\varphi}{\left(N+h\right)^2} \end{pmatrix}$$

$$F_{\varepsilon v}=\begin{pmatrix} 0 & \dfrac{1}{M+h} & 0 \\ -\dfrac{1}{N+h} & 0 & 0 \\ -\dfrac{\tan\varphi}{N+h} & 0 & 0 \end{pmatrix}$$

$$F_{\varepsilon\varepsilon}=\begin{pmatrix} 0 & \sigma\sin\varphi+\dfrac{V_E\tan\varphi}{N+h} & -\sigma\cos\varphi-\dfrac{V_E}{N+h} \\ -\sigma\sin\varphi-\dfrac{V_E\tan\varphi}{N+h} & 0 & -\dfrac{V_N}{M+h} \\ \sigma\cos\varphi+\dfrac{V_E}{N+h} & \dfrac{V_N}{M+h} & 0 \end{pmatrix}$$

2.3.4 Inertial Sensor Errors

All sensors are affected by errors which degrade their accuracy. The primary sources of errors in inertial sensors are bias, scale factor and noise. Some errors of inertial sensors are deterministic and can be determined through specific lab-calibration procedures. The remaining errors are not systematic and they need to be modeled stochastically.

The accelerometer and gyro measurements equations are:

$$\begin{aligned} f &= \tilde{f} + b_a + f \cdot S_a + f \cdot m_a + \eta_a \\ \omega &= \tilde{\omega} + b_g + f \cdot S_g + f \cdot m_g + \eta_g \end{aligned} \tag{2-29}$$

with

f and $\tilde{f}$ actual and measured specific force

ω and $\tilde{\omega}$ actual and measured angular rate

b_a and b_g sensor biases

S_a and S_g sensor scale factors

m_a and m_g non-orthogonality errors

η_a and η_g sensor noises

More detailed measurement equations can be found in Chatfield 1997 and El-Sheimy 2004, including further terms as non-linear scale factors and cross-axis coupling factors.

The sensor bias is defined as the average of the output, obtained during a specific period with fixed operational conditions when the input is null. The bias generally consists of two parts: a deterministic part called bias offset or turn-on bias and a stochastic part called bias drift or in-run bias. The turn-on bias is essentially the offset in the measurement and is constant over a single mission; it has deterministic nature and so can be determined by calibration procedure. The turn-on bias is generally negligible in high-end IMUs, while in low-cost sensors (used in this work) can be large and has to be determined with frequent calibrations or estimated in the Kalman filter. The bias drift is the rate at which the error in the sensor accumulates with time (El-Sheimy 2004); the bias drift has random nature and so must be modeled as a stochastic process.

The scale factor error is the ratio between the change in the output signal of the sensor and the change in the physical quantity to measure. In ideal conditions the scale factor should be unity (El-Sheimy 2004). This error has a deterministic nature and can theoretically be determined by calibration but generally is modeled as a random process. The non-orthogonality errors results from imperfection in mounting the sensor triad, so that each axis is affected by the measurements of the other axes (El-Sheimy 2004). This error has a deterministic nature and can be calibrated in the laboratory using suitable techniques (a low cost procedure is proposed in Angrisano et al. 2009), but usually is included in the INS error equations.

The sensor noise is an additional signal affecting the measurement, resulting from the sensor itself or from the other electronic equipment (El-Sheimy 2004). Noise has random nature and cannot be removed using deterministic models, but can only be modeled stochastically. Several stochastic models can be used to model noise and to choose the suitable model the autocorrelation sequence of the sensor output should be studied (or equivalently its spectral density) (Nassar 2003). Noise in inertial sensors usually is modeled as zero-mean white noise, i.e. it is considered to have a spectral density the same for all the frequencies of interest (Godha 2006). Different techniques can be adopted to study noise in inertial sensors. A possible option is the wavelet decomposition, detailed in Nassar 2003. The wavelet decomposition technique consists in splitting the signal into low and high frequency components; the low frequency component represents the slowly varying sensor errors (essentially the bias drift) and the high frequency component is the sensor noise. The standard deviation of the high frequency component is an estimation of the noise power. Another possible procedure is to compute the standard deviation using few seconds of static data (removing the mean) and several data sets; the mean of the computed standard deviations is an estimation of the noise power. This method is based on the assumption that in short intervals other errors and input are approximately constant (Petovello 2003).

2.3.5 MEMS Sensors

The inertial sensors adopted in this work are low-cost and a brief overview on their performance is below (from Angrisano et al. 2010).

The great advances in Micro Electro-Mechanical Systems (MEMS) has been made possible the development of a generation of low cost inertial sensors. MEMS IMU are characterized by small size, light weight and low cost with respect to high-end inertial sensors. These features make the MEMS sensors an attractive option for applications such as pedestrian or vehicular navigation. However, MEMS sensors are characterized by poorer performance too, so they cannot be used in autonomous mode for extended periods but they are well suited to integrated navigation systems (usually coupled with GNSS systems). MEMS sensor performance is summarized in the Table 2-2, where also navigation and a tactical grade IMU performance are listed for a direct comparison.

Table 2-2 – Summary of IMU Characteristics for Different Grades of Sensors (from Petovello 2003 and Godha 2006)

Parameter	IMU Grade		
	Navigation	Tactical	MEMS
Accelerometers			
In Run Bias (mg)	0.025	1	2.5
Turn On Bias (mg)	-	-	30
Scale Factor (PPM)	100	300	10000
VRW (g/√Hz)	-	2.16e-06	370e-06
Gyros			
In Run Bias (°/h)	0.0022	1	<1040
Turn On Bias (°/h)	-	-	5400
Scale Factor (PPM)	5	150	10000
ARW (°/h/√Hz)	6.92	7.5	226.8
Approx. Cost	>$90000	>$20000	<$2000

The ARW (Angular Random Walk) and VRW (Velocity Random Walk) are parameters usually included in the sensors data-sheets to describe their performance.

The ARW parameter describes the average deviation or error that will occur from integrating the noise on gyro output signal (Stockwell 2003). Similarly VRW parameter definition is based on the same concept for the accelerometers.

The performance and the cost of an IMU strongly depends on the gyro quality (El-Sheimy 2004). From Table 2-2 we can see that the turn on bias of MEMS gyro is about 5400 deg/h, while it is negligible in the navigation and tactical grade sensors. Also the in run bias can be 1040 deg/h in MEMS sensors, while is about 1 deg/h in a tactical grade gyro. These parameters provide a good assessment of MEMS performance with respect to higher grade sensors.

Chapter 3 Estimation and Reliability Overview

In the first part of this chapter an overview about the estimation methods used in this research is provided. Details of Extended Kalman Filter (EKF) and Least Square method (LS) are introduced and compared. Main references for this topics are Brown and Hwang (1997) and Petovello (2009). In the second part of the chapter the reliability testing and the blunder detections strategies are briefly reviewed.

3.1 Estimation

Estimation is the process of obtaining a set of unknowns of interest from a set of uncertain measurements, according to a definite optimization criterion (Bar-Shalom et al. 2001). To estimate the unknown parameters, a functional relationship has to be defined with the measurements; usually this relationship is referred to as the measurement model and the set of unknown parameters is referred to as system state vector.

The measurement model could be solved for the unknowns if the number of (independent) equations is at least equal to the number of the unknowns. If the measurements are redundant, the solution can be estimated in some optimal sense. If the measurement number equals the equation number, the solution is unique (if it exists) and there is no space for optimization.

If other equations are included in addition to the measurement model, the set of unknowns can be estimated also in situations of lack of measurements. These further equations can be obtained considering information about the system state dynamics, usually referred to as process model. The inclusion of the process model can provide in general a better estimation of the system state vector.

The measurement model is usually expressed in the form:

$$\underline{z}(t) = H(t) \cdot \underline{x}(t) + \underline{\eta}(t) \tag{3-1}$$

where:

$\underline{z}(t)$ is the measurement (or observation) vector at time *t*

$H(t)$ is the design matrix or geometry matrix at time *t*, containing the geometry of the observations with respect to the state vector

$\underline{x}(t)$ is the state vector at time *t*

$\underline{\eta}(t)$ is the measurement noise at time *t*, with spectral density $R(t)$

The process model is usually represented as:

$$\underline{\dot{x}}(t) = F(t) \cdot \underline{x}(t) + G(t) \cdot \underline{w}(t) \tag{3-2}$$

where:
the 'dot' notation indicates the time derivative,
$F(t)$ is the system dynamic matrix at time *t*, a coefficient matrix describing the dynamics of the system,
$G(t)$ is the shaping matrix at time *t*, used to shape the white noise in input to match the actual characteristic of the system,
$\underline{w}(t)$ is the process driving noise at time t, with spectral density $Q(t)$

The measurement and system models in equations (3-1) and (3-2) are supposed to be linear; actually it is common that these models are characterized by a more complicated form. In this case the models are previously treated by linearization techniques such as Taylor expansion (Petovello 2003).

The estimation methods adopted in this research are the Least Square method (described in the section 3.1.1), which uses only the knowledge of the measurement model to estimate the state vector and the Kalman filter (described in section 3.1.2), which uses also the process model.

3.1.1 Least Square Method

The Least Square method (LS) is the most common estimation procedure in geomatics application (Petovello 2009) and in LS the state vector estimation is based purely on the measurements. The discrete version of measurement model (3-1) is used, because the LS algorithm (as are the other algorithms considered herein) is usually implemented on a computer:

$$\underline{z}_k = H_k \cdot \underline{x}_k + \underline{\eta}_k \tag{3-3}$$

where the subscript '*k*' refers to the k^{th} epoch t_k.

The LS approach is to obtain an estimate of the state vector $\underline{\hat{x}}_k$ minimizing the sum of the squares of the difference $\left(\underline{z}_k - H_k \cdot \underline{\hat{x}}_k\right)$, referred to as residuals. To this purpose a cost function is defined as:

$$J_k = \left(\underline{z}_k - H_k \cdot \underline{\hat{x}}_k\right)^T \cdot \left(\underline{z}_k - H_k \cdot \underline{\hat{x}}_k\right) \tag{3-4}$$

The LS estimate is obtained computing and setting to zero the derivative of the cost function (3-4) and solving for $\underline{\hat{x}}_k$ (equation (3-5)):

$$\frac{dJ_k}{d\underline{\hat{x}}_k} = -2H_k^T \cdot \underline{z}_k + 2H_k^T H_k \cdot \underline{\hat{x}}_k = 0 \tag{3-5}$$

The result is:

$$\underline{\hat{x}}_k = \left(H_k^T H_k\right)^{-1} H_k^T \cdot \underline{z}_k \tag{3-6}$$

Equation (3-6) is the LS solution, whose error covariance matrix is

$$C_{\hat{x}} = \left(H_k^T H_k\right)^{-1} H_k^T \cdot C_z \cdot H\left(H_k^T H_k\right)^{-1} \tag{3-7}$$

where C_z is the measurement covariance matrix.

In ideal conditions of independent measurement errors, with zero mean and equal variance σ^2, the C_z matrix becomes diagonal with equal values on its diagonal and the solution error covariance matrix becomes

$$C_{\hat{x}} = \left(H_k^T H_k\right)^{-1} \sigma^2 \tag{3-8}$$

Taking into account in the estimation that the measurements are characterized by different accuracy, a Weighted LS (WLS) can be performed.
The new cost function is defined as:

$$J_k = \left(\underline{z}_k - H_k \cdot \underline{\hat{x}}_k\right)^T \cdot W \cdot \left(\underline{z}_k - H_k \cdot \underline{\hat{x}}_k\right) \tag{3-9}$$

with W weighting matrix.

The WLS solution, obtained by setting to zero the time derivative of the cost function (3-9) and solving for the state vector, is:

$$\underline{\hat{x}}_k = \left(H_k^T W H_k\right)^{-1} H_k^T W \cdot \underline{z}_k \tag{3-10}$$

and the WLS solution error covariance matrix is:

$$C_{\hat{x}} = \left(H_k^T W H_k\right)^{-1} H_k^T W C_z W H \left(H_k^T W H_k\right)^{-1} \tag{3-11}$$

The weighting matrix can be set as the inverse of the measurement covariance matrix, weighting the accurate measurements more and the noisy ones less (Brogan 1981); in this case the (3-11) becomes:

$$C_{\hat{x}} = \left(H_k^T W H_k\right)^{-1} = \left(H_k^T C_z^{-1} H_k\right)^{-1} \tag{3-12}$$

3.1.2 Kalman Filter

The Kalman Filter (KF) estimation is a common technique commonly used in navigational applications. KF uses knowledge about measurements and state vector dynamics and so adopts both measurement (3-1) and process models (3-2), in discrete form as follows:

$$\underline{z}_{k+1} = H_{k+1} \cdot \underline{x}_{k+1} + \underline{\eta}_{k+1} \tag{3-13}$$

$$\underline{x}_{k+1} = \Phi_{k+1,k} \cdot \underline{x}_k + \underline{w}_k \tag{3-14}$$

The measurement model in equation (3-13) is formally identical to the model used in LS, with the additional assumption of zero-mean white noise with Gaussian distribution for the measurement noise $\underline{\eta}_k$ (whose covariance matrix is indicated as R_k).

In the process model (3-14), $\Phi_{k+1,k}$ is the state transition matrix from epoch *k*th to *(k+1)*th and can be obtained from the continuous system dynamic matrix *F* in (3-2), assuming *F* time-invariant during the sampling time interval Δt, as:

$$\Phi_{k+1,k} = e^{F \cdot \Delta t} \cong I + F \cdot \Delta t \tag{3-15}$$

This assumption is not rigorously true, but the resulting error can be considered negligible because the sampling time interval is usually very small (Shin 2001).

The term $\underline{w}_k$ is the process driving noise at epoch k^{th}, with a covariance matrix Q_k, accounting for the uncertainty of the process model. The covariance matrix of the process noise Q_k can be obtained from the continuous spectral density matrix Q using the equation:

$$Q_k = \int_{t_k}^{t_{k+1}} \Phi_{k+1,\tau} G(\tau) Q(\tau) G^T(\tau) \Phi_{k+1,\tau}^T d\tau \tag{3-16}$$

The equation (3-16) is usually impractical, so a numerical approach has to be adopted; in this research the following approximation is used (Petovello 2003):

$$Q_k \approx \left[\Phi_{k+1,\tau} G(t_k) Q(t_k) G^T(t_k) \Phi_{k+1,\tau}^T + G(t_k) Q(t_k) G^T(t_k)\right] \frac{\Delta t}{2} \tag{3-17}$$

The process noise $\underline{w}_k$ is assumed to be white with zero-mean and Gaussian distribution and uncorrelated with the measurement noise $\underline{\eta}_k$.

The Kalman filter is a recursive algorithm using a series of prediction and update steps to obtain an optimal state vector estimate in a minimum variance sense.

The KF equations (whose details of derivation are in Brown and Hwang 1997) belong to two groups.

The first group contains the prediction equations, used to predict the state vector and the associated covariance matrix from the current to the next epoch, using the assumed process model. The equations performing the prediction step are:

$$\hat{\underline{x}}_{k+1}^{-} = \Phi_{k+1,k} \hat{\underline{x}}_k^{+} \tag{3-18}$$

$$P_{k+1}^{-} = \Phi_{k+1,k} P_k^{+} \Phi_{k+1,k}^T + Q_k \tag{3-19}$$

where the superscript "-" indicates a predicted (or a priori) quantity (i.e. before the measurement update) and the superscript "+" indicates the corrected (or a posteriori) quantity (i.e. after the measurement update). P_k is the covariance matrix of the state vector at epoch t_k.

The second group of equations is the correction equations, which update the state vector and the associated covariance matrix according to the measurement model. The KF update equations are:

$$\underline{\hat{x}}_{k+1}^{+} = \underline{\hat{x}}_{k+1}^{-} + K_{k+1}\underline{\nu}_{k+1} \tag{3-20}$$

$$P_{k+1}^{+} = \left(I - K_{k+1}H_{k+1}\right)P_{k+1}^{-} \tag{3-21}$$

where

K_{k+1} is the Kalman gain matrix at epoch t_{k+1} (defined below) and

$\underline{\nu}_{k+1}$ is the innovation vector at epoch t_{k+1}.

The innovation vector $\underline{\nu}_{k+1}$ is defined as the difference between the actual measurement vector and the predicted measurement vector, in turn defined as the predicted state vector projected on the measurement space:

$$\underline{\nu}_{k+1} = \underline{z}_{k+1} - \underline{\hat{z}}_{k+1} = \underline{z}_{k+1} - H_{k+1}\underline{\hat{x}}_{k+1}^{-} \tag{3-22}$$

The innovation vector can therefore be considered as an indication of the amount of information introduced in the system by the current measurements.

The Kalman gain matrix is a weighting factor, indicating how much the new information contained in the innovation vector influences the final state vector estimate. Practically the gain matrix weights the new information from the measurement against the predicted knowledge of the state (Petovello 2003).

The Kalman gain matrix is obtained minimizing the state vector variance and is defined as:

$$K_{k+1} = P_{k+1}^{-}H_{k+1}^{T}\left(H_{k+1}P_{k+1}^{-}H_{k+1}^{T} + R_{k+1}\right)^{-1} \tag{3-23}$$

The Kalman filter algorithm is illustrated in Figure 3-1.

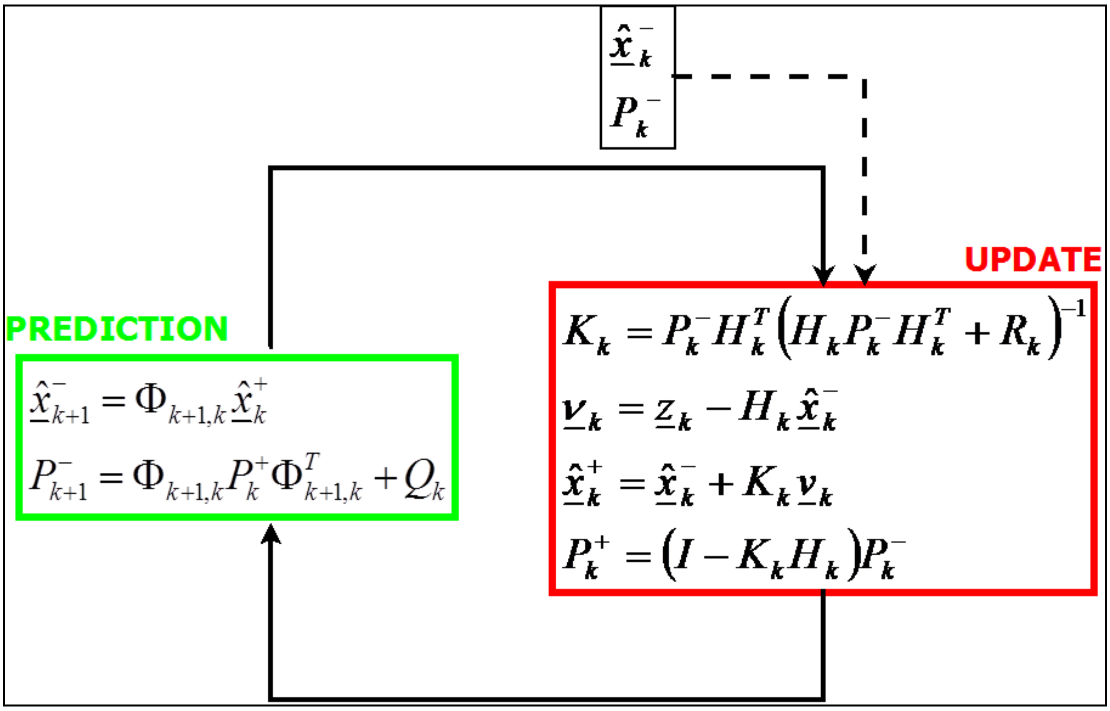

Figure 3-1 – Kalman Filter Algorithm

As mentioned previously, both measurement and process models are often more complicated than (3-1) and (3-2), and it is necessary a linearization process (usually with Taylor expansion) be adopted to reduce the equations to that form. The linearization should be performed around a nominal trajectory $\underline{x}^*(t)$, defined as the time-series of the parameters contained in the state vector. The actual state vector can then be expressed as:

$$\underline{x}(t) = \underline{x}^*(t) + \delta\underline{x}(t) \tag{3-24}$$

where $\delta\underline{x}(t)$ is a perturbation from the nominal trajectory.

After the linearization procedure, the estimation problem becomes estimating the perturbation vector (now state of the system) to add to the nominal state to obtain the “complete” state (by equation (3-24)).

The nominal trajectory $\underline{x}^*(t)$ can be known a priori and in this case a Linearized Kalman Filter (LKF) is performed. It is noted that a reasonable estimate of the trajectory is usually not available, especially with the accuracy necessary to satisfy the linearization assumptions (Petovello 2009). A more common approach is to use as a point of linearization the previous Kalman filter estimate; this approach is adopted in this research and is defined Extended Kalman Filter (EKF). In the EKF if the states are well estimated, the perturbation remains sufficiently small to satisfy the linearization assumptions. The EKF usually operates in a closed-loop mode, that is, every time the state vector $\underline{\delta x}(t)$ is updated, it is used to correct the nominal state. When this happens the state vector is reset to a null vector (Petovello 2009). An important consequence is that the state vector prediction (3-18) is no longer necessary, because the a posteriori state estimate after the correction is reset to zero. In the prediction step, only the covariance propagation must be performed. The state vector update results simplified as showed below:

$$\underline{\delta x}_{k+1}^{+} = \underline{\delta x}_{k+1}^{-} + K_{k+1}\left(\underline{\delta z}_{k+1} - H_{k+1}\underline{\delta x}_{k+1}^{-}\right) = K_{k+1}\underline{\delta z}_{k+1} \tag{3-25}$$

The covariance matrix update is unchanged.

3.2 Reliability Testing

The reliability concept is correlated with the ability to identify and discard the measurement affected by large errors (or blunders), which if undetected would largely corrupt the final system output.

In this research the systems involved are GNSS and INS sensors; the inertial systems are herein considered unaffected by blunders, although their errors are unbounded, because of their inherent characteristics of autonomy and immunity to interferences. GNSS systems instead are stable in the long-term but their short-term accuracy is strongly limited by signal quality. So the blunders are supposed to be essentially originated by GNSS signal corruption during the propagation path, related to multipath, cycle slips, ionospheric scintillation or other unspecified errors. Then the blunder detection and rejection is an essential procedure to improve the accuracy of the navigation parameters, especially in severe scenarios for propagation (as urban canyon, where multipath is the dominant error). In the context of GNSS, the reliability testing is referred to as Receiver Autonomous Integrity Monitoring (RAIM).

In reliability testing usually the measurements are assumed to follow a defined distribution and the presence of a blunder on a measurement means that this measurement no longer belongs to the defined distribution. Actually it is not possible to know for sure if a measurement belongs to the pre-defined distribution or not, so a statistical approach is used, defining a decision variable and threshold to compare against in order to obtain this information with a certain probability. The event that no failure occurs is called Null-Hypothesis H_0, the event that a failure occurs is referred to as Alternate Hypothesis H_a; if the decision variable D does not exceed the threshold T, the Null-Hypothesis is accepted and no blunders are supposed to exist for the considered measurement set, but if D exceeds T, the Alternate-Hypothesis is accepted and a blunder is assumed. Two kinds of errors can occur: a false alarm if D>T in absence of blunders and missed detection if D<T in presence of blunders.

The probability of false alarm P_{FA} and missed detection P_{MD} are expressed as:

$$P_{FA} = P(D \geq T \mid H_0) \tag{3-26}$$

$$P_{MD} = P(D < T \mid H_a) \tag{3-27}$$

where the symbol $P(\bullet)$ indicates the probability of the event between the brackets.

Various procedures can be used to perform a quality control on the measurements, herein the adopted strategies are described (from Kuusniemi etal 2004, Petovello 2003, Petovello 2009).

In the LS case a quality control is performed testing the residuals:

$$\underline{r} = \underline{z} - H \cdot \underline{\hat{x}} \tag{3-28}$$

The residuals, defined as the difference between the actual measurements and the predicted measurements, represent the level of agreement of the measurements to each other and so are suitable to assess the quality of the LS solution.

In the GNSS contest the measurement errors are assumed to be Gaussian with zero-mean and uncorrelated; the decision variable D is defined as the sum of the squares of the residuals, weighted by the associated covariance matrix C_r:

$$D = \underline{r}^T \cdot C_r \cdot \underline{r} \tag{3-29}$$

and is assumed to follow a χ^2 distribution with $(m-n)$ degrees of freedom or redundancy, that is the difference between the number of measurements m and the number of states n.

The threshold T is usually related to the probability of false alarm and to the redundancy as shown in equation (3-30):

$$T = \chi^2_{1-P_{FA},(m-n)} \tag{3-30}$$

where the notation $\chi^2_{1-P_{FA},(m-n)}$ indicates the abscissa corresponding to a probability value $(1-P_{FA})$ of a chi-square distribution of $(m-n)$ order.

A common procedure consists of fixing P_{FA} according to the application requirements and letting the threshold vary with the redundancy number.
A typical value for the probability of false alarm is 0.1% (Petovello 2003).
The described procedure is referred to as the global test and checks the measurements self-consistency and is useful to verify the presence of a blunder among the observations.
To identify the blunder/s in the set a local test can be performed; to this purpose the normalized residuals are defined as:

$$w_i = \left| \frac{r_i}{\sqrt{(C_r)_{ii}}} \right| \tag{3-31}$$

where the index $i = 1:m$, with m number of observations.

The normalized residuals w_i are assumed to be normally distributed in case of lack of blunders and can be tested as follows:

$$\begin{aligned} w_i &\geq n_{1-P_{FA}/2} \\ w_i &< n_{1-P_{FA}/2} \end{aligned} \tag{3-32}$$

where the notation $n_{1-P_{FA}/2}$ indicates the abscissa corresponding to a probability value $(1-P_{FA}/2)$ of a normal distribution.

The largest normalized residual exceeding the considered threshold is suspected to contain a blunder; actually there is no guarantee that the maximum w_i corresponds to an outlier and more than only one blunder can be in the data set. Therefore a recursive application of the global and local tests can be carried out, performing a multiple blunder rejection. In this work only a minimum number of exclusions is desired, because tests are carried out in critical environments as urban canyons, characterized by lack of observations.

In KF case, the measurement quality control is performed testing the innovation vector (3-22), whose properties are to be zero-mean white noise with Gaussian distribution, that is, same as the process noise $\underline{w}_k$ and the measurement noise $\underline{\eta}_k$. Furthermore the covariance matrix of the innovation vector C_{v_k} is (computations details are in Brown and Hwang (1997)):

$$C_{v_k} = H_k P_k^- H_k^T + R_k \tag{3-33}$$

The following blunder detection procedure is detailed in Petovello (2003).
A simplified assumption is made about the presence of a single blunder in the data set. When an observation is affected by a single blunder, the measurement model (3-13) becomes:

$$\underline{z}_k = H_k \cdot \underline{x}_k + \underline{m}_{k_i} \cdot \nabla_{k_i} + \underline{\eta}_k \tag{3-34}$$

where
∇_{k_i} is a scalar expressing the value of the blunder on the i^{th} measurement and
$\underline{m}_{k_i}$ is a vector projecting the blunder on the i^{th} measurement.

The innovation vector becomes biased by the term $\underline{m}_{k_i} \cdot \nabla_{k_i}$ as shown below:

$$\underline{v}_k = \underline{z}_k - H_k \cdot \underline{\hat{x}}_k^- - \underline{m}_{k_i} \cdot \nabla_{k_i} \tag{3-35}$$

and is supposed to maintain the same covariance matrix C_{v_k}.

Considering these proprieties of the innovation vector, a decision variable can be built related to it as:

$$D_i = \frac{\underline{m}_k^T \cdot C_{v_k}^{-1} \cdot \underline{v}_k}{\sqrt{\left(C_{v_k}^{-1}\right)_{ii}}} \tag{3-36}$$

The considered decision variable has Gaussian distribution with zero-mean in the absence of a blunder and is biased in case of a blunder being present. Hence reliability testing can be carried out using as threshold the point of the x-axis corresponding to a probability of $(1 - P_{FA} / 2)$ of a normal distribution (equation (3-37)).

$$\begin{aligned} \left| D_i \right| &\geq n_{1-P_{FA}/2} \\ \left| D_i \right| &< n_{1-P_{FA}/2} \end{aligned} \tag{3-37}$$

The Null-Hypothesis (no blunder on the i^{th} observation) is accepted if the first equation is verified, the Alternate Hypothesis (blunder on the i^{th} observation) is accepted if the second one is verified.

In case of multiple blunders simultaneously, this strategy can be used recursively, rejecting at each step the largest blunder until no more blunders are detected.

Chapter 4 GPS/GLONASS PVT Algorithms

In this chapter the GNSS measurement models are reviewed.

First a single satellite system is considered (GPS or GLONASS) and the algorithms used for PVT (Position-Velocity-Time) estimation are explained. Whenever a concept is different between GPS and GLONASS, it is clearly pointed out. Subsequently the GPS/GLONASS combined model is introduced.

The discussion is taken from Kaplan and Leva 2006 and Axelrad and Brown 1996.

The reviewed measurement models will be used (in the Chapter 5) to perform the GNSS only filter of the loosely coupled integration, which in this research is implemented by a WLS estimator. Moreover the considered models will be used, coupled with suitable process models (described in the Chapter 5), to implement the GNSS/INS filter in the tightly coupled architecture.

4.1 Position Computation using Pseudorange

In this section the algorithm to compute the GPS receiver position from pseudorange measurements is described. The algorithm is valid for GLONASS system too.

Recall the PR measurement equation (2-2), applying all the corrections described in 2.1.3 and including all the residual errors in the term ε_{PR}, yields:

$$PR = d + c\delta t + \varepsilon_{PR} \tag{4-1}$$

where

$c\delta t$ is the receiver clock bias (the subscript "*R*" of the receiver clock offset is omitted when no ambiguity is possible),

the geometric range is expressed as $d = \sqrt{(x_S - x)^2 + (y_S - y)^2 + (z_S - z)^2}$,

(x_S, y_S, z_S) are the satellite coordinates and

(x, y, z) are the receiver coordinates expressed in ECEF frame.

The receiver coordinates and the receiver offset $c\delta t$ form the state vector to be estimated $\underline{x} = [x, y, z, c\delta t]^T$.

The satellite coordinates in the ECEF frame are computed using the ephemeris information contained in the navigation message, according to the algorithm showed in the sections 4.3.

At least four simultaneous visible satellites are necessary to form a set of equations like (4-1) to solve for the unknowns, in closed-form or with iterative techniques based on linearization; in this case a linearization procedure is performed around an approximate position and time bias estimate $\underline{\hat{x}} = [x_0, y_0, z_0, c\delta t_0]^T$.

Expanding in Taylor series the equation (4-1) about the approximate point and truncating the expansion at the first order yields:

$$PR = PR_0 + \left.\frac{\partial PR}{\partial x}\right|_{\underline{\hat{x}}}(x - x_0) + \left.\frac{\partial PR}{\partial y}\right|_{\underline{\hat{x}}}(y - y_0) + \left.\frac{\partial PR}{\partial z}\right|_{\underline{\hat{x}}}(z - z_0) + \left.\frac{\partial PR}{\partial (c\delta t)}\right|_{\underline{\hat{x}}}(c\delta t - c\delta t_0)$$

(4-2)

where

the notation $\left.\frac{\partial PR}{\partial x}\right|_{\underline{\hat{x}}}$ represents the partial derivative of the function PR with respect to the variable x, evaluated in the approximate point $\underline{\hat{x}}$ and

PR_0 is the predicted PR, i.e. the pseudorange evaluated in the approximate point $\underline{\hat{x}}$, computed as $PR_0 = \sqrt{(x_S - x_0)^2 + (y_S - y_0)^2 + (z_S - z_0)^2} + c\delta t_0$.

After some simple computations the equation (4-2) becomes:

$$z = a_X \Delta x + a_Y \Delta y + a_Z \Delta z + \Delta(c\delta t) \tag{4-3}$$

where

$z = PR - PR_0$ is the difference between the measured and the predicted pseudorange,

$\Delta x = x - x_0$, $\Delta y = y - y_0$, $\Delta z = z - z_0$, $\Delta(c\delta t) = c\delta t - c\delta t_0$ are the incremental components from the linearization point,

$a_X = \frac{x_0 - x_S}{d_0}$, $a_Y = \frac{y_0 - y_S}{d_0}$, $a_Z = \frac{z_0 - z_S}{d_0}$ are the direction cosines of the unit vector from the approximate position to the observed satellite.

A set of equations as (4-3) forms the linearized measurement model:

$$\underline{z}_{PR} = H_{PR} \cdot \underline{\Delta x} + \underline{\varepsilon}_{PR} \tag{4-4}$$

where

$\underline{z}_{PR}$ is the vector of the pseudorange measurements corrected by a priori information,

H_{PR} is the geometry matrix, containing the direction cosines defined above,

$\underline{\varepsilon}_{PR}$ is the vector of residual errors,

$\underline{\Delta x} = \left[\Delta x \quad \Delta y \quad \Delta z \quad \Delta\left(c\delta t\right)\right]^T$ is the new unknown vector, which can be estimated using the LS method.

The receiver coordinates and clock offset can be finally computed, after the $\underline{\Delta x}$ estimation, as:

$$\underline{x} = \underline{\hat{x}} + \underline{\Delta x} \tag{4-5}$$

To obtain the user position in latitude, longitude and altitude from the ECEF coordinates different algorithms can be used; herein the Bowring algorithm is adopted (Bowring 1976).

Herein the PR measurement model is implemented in the ENU frame centered in the approximate receiver position $\left(x_0, y_0, z_0\right)$. In the ENU frame the geometric range is expressed as

$$d = \sqrt{\left(E_S - E\right)^2 + \left(N_S - N\right)^2 + \left(U_S - U\right)^2}$$

where $\left(E_S, N_S, U_S\right)$ are the satellite coordinates and $\left(E, N, U\right)$ are the receiver coordinates expressed in the considered ENU frame.

The PR measurement equation (4-1) can be modified as:

$$PR = \sqrt{\left(E_S - E\right)^2 + \left(N_S - N\right)^2 + \left(U_S - U\right)^2} + c\delta t + \varepsilon_{PR} \tag{4-6}$$

and can be linearized around the approximate point $\underline{\hat{x}}$, in turn expressed in the ENU frame as $\underline{\hat{x}} = \left[0,0,0,c\delta t_0\right]^T$, yielding:

$$PR = PR_0 + \left.\frac{\partial PR}{\partial E}\right|_{\underline{\hat{x}}} \Delta E + \left.\frac{\partial PR}{\partial N}\right|_{\underline{\hat{x}}} \Delta N + \left.\frac{\partial PR}{\partial U}\right|_{\underline{\hat{x}}} \Delta U + \left.\frac{\partial PR}{\partial(c\delta t)}\right|_{\underline{\hat{x}}} \Delta(c\delta t) \tag{4-7}$$

After some simple computations the equation (4-7) becomes:

$$z = a_E \Delta E + a_N \Delta N + a_U \Delta U + \Delta(c\delta t) \tag{4-8}$$

where

$z = PR - PR_0$ is the difference between the measured and the predicted pseudorange,

$\Delta E = E$, $\Delta N = N$, $\Delta U = U$, $\Delta(c\delta t) = c\delta t - c\delta t_0$ are the incremental components from the linearization point,

$a_E = \frac{-E_S}{d_0}$, $a_N = \frac{-N_S}{d_0}$, $a_U = \frac{-U_S}{d_0}$ are the direction cosines of the unit vector from the approximate position to the observed satellite.

A set of equations like (4-8) is formally identical to (4-4), with the differences that the geometry matrix contains the new direction cosines and the new unknown vector to be estimated is $\underline{\Delta x} = [\Delta E \quad \Delta N \quad \Delta U \quad \Delta(c\delta t_R)]^T$.

To obtain the user position in latitude, longitude and altitude (φ, λ, h) the relation below must be used (El-Sheimy 2004):

$$\begin{gathered} \varphi = \varphi_0 + \frac{\Delta N}{(\rho + h)} \\ \lambda = \lambda_0 + \frac{\Delta E}{(N + h)\cos\varphi} \\ h = h_0 + \Delta U \end{gathered} \tag{4-9}$$

with

$(\varphi_0, \lambda_0, h_0)$ geographic coordinates of the approximate position,

N prime vertical radius of curvature,

ρ meridian radius of curvature.

4.2 Velocity Computation using Doppler

In the modern GPS receivers the velocity is obtained processing the Doppler observable, which represents the frequency shift produced by the relative motion of the satellite with respect to the receiver (Kaplan and Leva 2006).

The frequency observed at the receiver f_R is related to the transmitted frequency f_T by the classical Doppler equation:

$$f_R = f_T \left[1 - \frac{1}{c} \left(\underline{V}_S - \underline{V} \right) \cdot \frac{\left(\underline{r}_S - \underline{r} \right)}{\left| \underline{r}_S - \underline{r} \right|} \right] \tag{4-10}$$

where

$\underline{r}_S \equiv \left(x_S, y_S, z_S \right)$ is the satellite position vector,

$\underline{r} \equiv \left(x, y, z \right)$ is the receiver position vector,

$\left(\underline{V}_S - \underline{V} \right)$ is the satellite-receiver relative velocity vector, defined as the difference between satellite velocity vector $\underline{V}_S = \left[V_{SX} \quad V_{SY} \quad V_{SZ} \right]^T$ and receiver velocity vector $\underline{V} = \left[V_X \quad V_Y \quad V_Z \right]^T$.

All the vector are expressed in the ECEF frame.

The dot product $\left(\underline{V}_S - \underline{V} \right) \cdot \frac{\left(\underline{r}_S - \underline{r} \right)}{\left| \underline{r}_S - \underline{r} \right|}$ represents the projection of the relative velocity vector on the receiver-satellite direction, i.e. is the range rate $\dot{d}$.

The Doppler shift is:

$$f_R - f_T = -\frac{f_T}{c} \left(\underline{V}_S - \underline{V} \right) \cdot \frac{\left(\underline{r}_S - \underline{r} \right)}{\left| \underline{r}_S - \underline{r} \right|} = -\frac{f_T}{c} \dot{d} \tag{4-11}$$

Scaling the above equation with the signal wavelength λ yields:

$$\dot{d} = -\lambda \cdot \left(f_R - f_T \right) \tag{4-12}$$

The measured range rate (or pseudorange rate) must take into account that the observed frequency is affected by the receiver clock drift and the transmitted frequency is affected by the satellite clock drift and can be defined as:

$$P\dot{R} = -\lambda\left(\hat{f}_R - \hat{f}_T\right) \tag{4-13}$$

where

λ is the signal wavelength (m)

$\hat{f}_R$ is the measured frequency (Hz) related to the ideal received frequency by the relation $\hat{f}_R = f_R + \Delta f_R$

$\hat{f}_T$ is the actual transmitted frequency (Hz) related to the nominal transmitted frequency f_T by the relationship $\hat{f}_T = f_T + \Delta f_T$.

Rearranging the equation (4-13) and considering that $\lambda \cdot \Delta f_R = c\dot{\delta t}_R$ and $\lambda \cdot \Delta f_S = c\dot{\delta t}_S$, yields:

$$P\dot{R} = \dot{d} + c\dot{\delta t}_S - c\dot{\delta t}_R \tag{4-14}$$

Completing the equation with all the error sources affecting the Doppler observable (orbital, propagation, relativistic), returns the range derivative equation (2-4); the satellite clock drift $c\dot{\delta t}_S$ can be determined using the information contained in the navigation message and is usually negligible (Kaplan and Leva 2006). Applying the suitable corrections and collecting the residuals in the term $\varepsilon_{P\dot{R}}$ yields (the subscript "R" is omitted in the receiver clock drift expression for clarity):

$$P\dot{R} = \dot{d} + c\dot{\delta t} + \varepsilon_{P\dot{R}} \tag{4-15}$$

Several approaches can be adopted to estimate the receiver velocity from the equation (4-15) and two of them are described in this section.

The first approach is more immediate, in fact the equation (4-15) can simply be rearranged as:

$$P\dot{R} - \underline{V}_S \cdot \frac{\left(\underline{r}_S - \underline{r}\right)}{\left|\underline{r}_S - \underline{r}\right|} = -\underline{V} \cdot \frac{\left(\underline{r}_S - \underline{r}\right)}{\left|\underline{r}_S - \underline{r}\right|} + c\dot{\delta t} \tag{4-16}$$

Expanding the dot products:

$$\begin{aligned} & P\dot{R} - V_{SX}\frac{x_S - x_0}{d} - V_{SY}\frac{y_S - y_0}{d} - V_{SZ}\frac{z_S - z_0}{d} = \\ & = \frac{x_0 - x_S}{d}V_X + \frac{y_0 - y_S}{d}V_Y + \frac{z_0 - z_S}{d}V_Z + c\dot{\delta t} \end{aligned} \tag{4-17}$$

As it can be noticed, the equation (4-17) is linear for the receiver velocity components and clock drift, which are the unknowns of the problem, so the linearization process is unnecessary. In this approach the receiver position components must be known a priori, by applying the position model (4-4) or can be approximated by a previous state knowledge. The satellite position and velocity have to be known too, determined from ephemeris data. In the considered conditions, to solve for the receiver velocity components and clock drift at least four simultaneous Doppler measurements are necessary.

In the second approach the receiver position is not considered known a priori, but it is included in the set of the unknowns; so a "Doppler positioning" is performed (Axelrad and Brown 1996).

The equation (4-15) is expanded in Taylor series around the approximate state vector $\underline{\hat{x}} = \begin{bmatrix} x_0 & y_0 & z_0 & V_{X0} & V_{Y0} & V_{Z0} & c\dot{\delta t}_0 \end{bmatrix}^T$, which includes receiver position, velocity and clock drift estimate; truncating the expansion at the first order yields:

$$\begin{aligned} P\dot{R} = P\dot{R}_0 & + \left.\frac{\partial P\dot{R}}{\partial x}\right|_{\underline{\hat{x}}}(x - x_0) + \left.\frac{\partial P\dot{R}}{\partial y}\right|_{\underline{\hat{x}}}(y - y_0) + \left.\frac{\partial P\dot{R}}{\partial z}\right|_{\underline{\hat{x}}}(z - z_0) + \\ & + \left.\frac{\partial P\dot{R}}{\partial V_X}\right|_{\underline{\hat{x}}}(V_X - V_{X0}) + \left.\frac{\partial P\dot{R}}{\partial V_Y}\right|_{\underline{\hat{x}}}(V_Y - V_{Y0}) + \left.\frac{\partial P\dot{R}}{\partial V_Z}\right|_{\underline{\hat{x}}}(V_Z - V_{Z0}) + \left.\frac{\partial P\dot{R}}{\partial \left(c\dot{\delta t}\right)}\right|_{\underline{\hat{x}}}\left(c\dot{\delta t} - c\dot{\delta t}_0\right) \end{aligned} \tag{4-18}$$

where

$P\dot{R}_0$ is the predicted pseudorange derivative, i.e. the pseudorange rate evaluated in the approximate point $\underline{\hat{x}}$ and computed as

$$P\dot{R}_0 = \dot{d}_0 + c\dot{\delta t}_0 = \frac{(x_S - x_0)(V_{SX} - V_{X0}) + (y_S - y_0)(V_{SY} - V_{Y0}) + (z_S - z_0)(V_{SZ} - V_{Z0})}{d_0} + c\dot{\delta t}_0$$

After some simple computation the equation (4-18) becomes:

$$z = b_X \cdot \Delta x + b_Y \cdot \Delta y + b_Z \cdot \Delta z + b_{VX} \cdot \Delta V_X + b_{VY} \cdot \Delta V_Y + b_{VZ} \cdot \Delta V_Z + \Delta\left(c\delta\dot{t}\right) \qquad (4\text{-}19)$$

where

$z = P\dot{R} - P\dot{R}_0$ is the difference between the measured and predicted pseudorange rate,

$\Delta x = x - x_0$, $\Delta y = y - y_0$, $\Delta z = z - z_0$, $\Delta V_X = V_X - V_{X0}$, $\Delta V_Y = V_Y - V_{Y0}$, $\Delta V_Z = V_Z - V_{Z0}$, $\Delta\left(c\delta\dot{t}\right) = c\delta\dot{t} - c\delta\dot{t}_0$ are the incremental components from the linearization point and

the coefficients $b_X, b_Y, b_Z, b_{VX}, b_{VY}, b_{VZ}$ are the partial derivatives in equation (4-18) which are given by

$$b_X = \left.\frac{\partial P\dot{R}}{\partial x}\right|_{\underline{\hat{x}}} = \frac{V_{X0} - V_{SX}}{d_0} + \frac{\left(x_0 - x_s\right)\left[\left(x_s - x_0\right)\left(V_{SX} - V_{X0}\right) + \left(y_s - y_0\right)\left(V_{SY} - V_{Y0}\right) + \left(z_s - z_0\right)\left(V_{SZ} - V_{Z0}\right)\right]}{d_0^3}$$

$$b_Y = \left.\frac{\partial P\dot{R}}{\partial y}\right|_{\underline{\hat{x}}} = \frac{V_{Y0} - V_{SY}}{d_0} + \frac{\left(y_0 - y_s\right)\left[\left(x_s - x_0\right)\left(V_{SX} - V_{X0}\right) + \left(y_s - y_0\right)\left(V_{SY} - V_{Y0}\right) + \left(z_s - z_0\right)\left(V_{SZ} - V_{Z0}\right)\right]}{d_0^3}$$

$$b_Z = \left.\frac{\partial P\dot{R}}{\partial z}\right|_{\underline{\hat{x}}} = \frac{V_{Z0} - V_{SZ}}{d_0} + \frac{\left(z_0 - z_s\right)\left[\left(x_s - x_0\right)\left(V_{SX} - V_{X0}\right) + \left(y_s - y_0\right)\left(V_{SY} - V_{Y0}\right) + \left(z_s - z_0\right)\left(V_{SZ} - V_{Z0}\right)\right]}{d_0^3}$$

$$b_{VX} = \left.\frac{\partial P\dot{R}}{\partial V_X}\right|_{\underline{\hat{x}}} = \frac{x_0 - x_S}{d_0}$$

$$b_{VY} = \left.\frac{\partial P\dot{R}}{\partial V_Y}\right|_{\underline{\hat{x}}} = \frac{y_0 - y_S}{d_0},$$

$$b_{VZ} = \left.\frac{\partial P\dot{R}}{\partial V_Z}\right|_{\underline{\hat{x}}} = \frac{z_0 - z_S}{d_0}.$$

The linearized Doppler measurement model, consisting of equations as (4-19), is:

$$\underline{z}_{P\dot{R}} = H_{P\dot{R}} \cdot \underline{\Delta x} + \underline{\varepsilon}_{P\dot{R}} \qquad (4\text{-}20)$$

where

$\underline{z}_{P\dot{R}}$ is the vector of the pseudorange rate measurements corrected by a priori information,

$H_{P\dot{R}}$ is the geometry matrix,

$\underline{\varepsilon}_{P\dot{R}}$ is the vector of residual errors,

$\underline{\Delta x} = \begin{bmatrix} \Delta x & \Delta y & \Delta z & \Delta V_X & \Delta V_Y & \Delta V_Z & \Delta\left(c\dot{\delta}t_0\right) \end{bmatrix}^T$ is the unknown vector, which can be estimated using the LS method.

The receiver position, velocity and clock drift can be finally computed, after the $\underline{\Delta x}$ estimation as:

$$\underline{x} = \underline{\hat{x}} + \underline{\Delta x} \tag{4-21}$$

This approach has the advantage to allow the receiver position estimation, as well as the velocity and clock drift; anyway the Doppler positioning is characterized by an observation geometry weaker than the pseudorange positioning and thus in the context of GPS it is essentially used for initial position estimation (Axelrad and Brown 1996). To solve the equation set (4-20) for the unknown vector at least seven simultaneous Doppler observations are necessary; owing to the above-mentioned “weakness” of this model for the position determination, this model is usually used in conjunction with the PR model as shown in 4.4.

In this research the implementation in ENU frame is preferred.

In the ENU implementation the measurement equation is obtained linearizing around the approximate state vector $\underline{\hat{x}} = \begin{bmatrix} 0 & 0 & 0 & V_{E0} & V_{N0} & V_{U0} & c\dot{\delta}t_0 \end{bmatrix}^T$ as:

$$\begin{aligned} P\dot{R} = P\dot{R}_0 &+ \left.\frac{\partial P\dot{R}}{\partial E}\right|_{\underline{\hat{x}}} \Delta E + \left.\frac{\partial P\dot{R}}{\partial N}\right|_{\underline{\hat{x}}} \Delta N + \left.\frac{\partial P\dot{R}}{\partial U}\right|_{\underline{\hat{x}}} \Delta U + \\ &+ \left.\frac{\partial P\dot{R}}{\partial V_E}\right|_{\underline{\hat{x}}} \Delta V_E + \left.\frac{\partial P\dot{R}}{\partial V_N}\right|_{\underline{\hat{x}}} \Delta V_N + \left.\frac{\partial P\dot{R}}{\partial V_U}\right|_{\underline{\hat{x}}} \Delta V_U + \left.\frac{\partial P\dot{R}}{\partial\left(c\dot{\delta}t\right)}\right|_{\underline{\hat{x}}} \Delta\left(c\dot{\delta}t\right) \end{aligned} \tag{4-22}$$

where

$\left(V_E, V_N, V_U\right)$ are the receiver velocity components in ENU.

After some simple computations the equation (4-22) can be expressed as (4-19) in the form:

$$z = b_E \cdot \Delta E + b_N \cdot \Delta N + b_U \cdot \Delta U + b_{VE} \cdot \Delta V_E + b_{VN} \cdot \Delta V_N + b_{VU} \cdot \Delta V_U + \Delta\left(c\dot{\delta t}\right) \quad (4\text{-}23)$$

where

$z = P\dot{R} - P\dot{R}_0$ is the difference between the measured and predicted pseudorange rate,

$P\dot{R}_0$ is the predicted pseudorange derivative expressed in the ENU frame as $P\dot{R}_0 = \frac{E_S\left(V_{SE} - V_{E0}\right) + N_S\left(V_{SN} - V_{N0}\right) + U_S\left(V_{SU} - V_{U0}\right)}{d_0} + c\dot{\delta t}_0 = \dot{d}_0 + c\dot{\delta t}_0$,

$\left(V_{SE}, V_{SN}, V_{SU}\right)$ are the satellite velocity components in ENU,

$\Delta E = E$, $\Delta N = N$, $\Delta U = U$, $\Delta V_E = V_E - V_{E0}$, $\Delta V_N = V_N - V_{N0}$, $\Delta V_U = V_U - V_{U0}$, $\Delta\left(c\dot{\delta t}\right) = c\dot{\delta t} - c\dot{\delta t}_0$ are the incremental components from the linearization point and the coefficients $b_E, b_N, b_U, b_{VE}, b_{VN}, b_{VU}$ are

$$b_E = \left.\frac{\partial P\dot{R}}{\partial E}\right|_{\hat{\underline{x}}} = \frac{V_{E0} - V_{SE}}{d_0} - \frac{E_S \cdot \dot{d}_0}{d_0^2},$$

$$b_N = \left.\frac{\partial P\dot{R}}{\partial N}\right|_{\hat{\underline{x}}} = \frac{V_{N0} - V_{SN}}{d_0} - \frac{N_s \cdot \dot{d}_0}{d_0^2}$$

$$b_U = \left.\frac{\partial P\dot{R}}{\partial U}\right|_{\hat{\underline{x}}} = \frac{V_{U0} - V_{SU}}{d_0} - \frac{U_s \cdot \dot{d}_0}{d_0^2},$$

$$b_{VE} = \left.\frac{\partial P\dot{R}}{\partial V_E}\right|_{\hat{\underline{x}}} = \frac{-E_S}{d_0}$$

$$b_{VN} = \left.\frac{\partial P\dot{R}}{\partial V_N}\right|_{\hat{\underline{x}}} = \frac{-N_S}{d_0}$$

$$b_{VU} = \left.\frac{\partial P\dot{R}}{\partial V_U}\right|_{\hat{\underline{x}}} = \frac{-U_S}{d_0}.$$

4.3 Satellite Position and Velocity Computation from Ephemeris

As clearly evidenced in the sections 4.1 and 4.2, the determination of the satellite position and velocity is necessary to compute the receiver position and velocity.

The algorithms for GPS and GLONASS are different because the ephemerides are differently parameterized and broadcasted by the two systems (see 2.2.1) and so the two cases are treated separately. In this work the algorithms for the satellite position and velocity are carried out using broadcast ephemerides, stored in the navigation message, and are usable for real-time applications.

The algorithm for the determination of GPS satellite position and velocity is extensively treated in IS-GPS-200 2004 and Remondi 2004 and is reported below.

In GPS system the broadcast ephemeris consists of Keplerian elements and perturbation terms (IS-GPS-200 2004) and are listed in the Table 4-1.

Table 4-1 – GPS Broadcast Ephemeris (adapted by IS-GPS-200 2004)

Parameter	**Description**	**Note**
M_0	Mean Anomaly at Reference Time	Keplerian Element (rad)
Δn	Mean Motion Correction	Perturbation Term (rad/s)
e	Eccentricity	Keplerian Element (dimensionless)
$\sqrt{A}$	Square Root of Semi-Major Axis	Keplerian Element ($m^{1/2}$)
Ω_0	Longitude of Ascending Node at Weekly Epoch	Keplerian Element (rad)
i_0	Inclination Angle at Reference Time	Keplerian Element (rad)
ω	Argument of Perigee	Keplerian Element (rad)
$\dot{\Omega}$	Rate of Right Ascension	Perturbation Term (rad/s)
$IDOT$	Rate of Inclination Angle	Perturbation Term (rad/s)
C_{uc}	Amplitude of the Cosine Harmonic Correction Term to the Argument of Latitude	Perturbation Term (rad)
C_{us}	Amplitude of the Sine Harmonic Correction Term to the Argument of Latitude	Perturbation Term (rad)
C_{rc}	Amplitude of the Cosine Harmonic Correction Term to the Orbit Radius	Perturbation Term (m)
C_{rs}	Amplitude of the Sine Harmonic Correction Term to the Orbit Radius	Perturbation Term (m)
C_{ic}	Amplitude of the Cosine Harmonic Correction Term to the Angle of Inclination	Perturbation Term (rad)

C_{is}	Amplitude of the Sine Harmonic Correction Term to the Angle of Inclination	Perturbation Term (rad)
t_{oe}	Reference Time Ephemeris	(s)

The algorithm to compute the GPS satellite position and velocity in ECEF frame at the epoch t, using the broadcast ephemeris referred to the epoch t_{oe}, is summarized in Table 4-2; the epoch t is the time in which the signal is transmitted by the satellite.

Table 4-2 – Algorithm for the GPS Satellite Position and Velocity Computation (adapted by IS-GPS-200 2004 and Remondi 2004)

$\mu = 3.986005 \cdot 10^{14}$ (m^3/s^2)	Earth's Gravitational Constant
$\dot{\Omega}_e = 7.2921151467 \cdot 10^{-5}$ (rad/s)	Earth's Rotation Rate
$A = \left(\sqrt{A}\right)^2$	Semi-Major Axis
$n_0 = \sqrt{\dfrac{\mu}{A^3}}$	Computed Mean Motion
$\Delta t = t - t_{oe}$	Time from t_{oe}
$n = n_0 + \Delta n$	Corrected Mean Motion
$M = M_0 + n \cdot \Delta t$	Mean Anomaly
$M = E - e\sin\left(E\right)$	Kepler’s Equation (to be solved for E by Iteration)
$\dot{M} = n$	Mean Anomaly Rate
$\dot{E} = \dfrac{\dot{M}}{1 - e\cos\left(E\right)}$	Eccentric Anomaly Rate
$v = 2\arctan\left(\sqrt{\dfrac{1+e}{1-e}}\tan\left(\dfrac{E}{2}\right)\right)$	True Anomaly

$\dot{v} = \frac{\sin(E)\dot{E}(1+e\cdot\cos(v))}{(1-e\cdot\cos(E))\cdot\sin(v)}$	True Anomaly Rate
$\theta = v+\omega$	Argument of Latitude
$u = \theta + C_{us}\sin(2\theta) + C_{uc}\cos(2\theta)$	Corrected Argument of Latitude
$\dot{u} = \dot{v} + 2\left[C_{us}\cos(2\theta) - C_{uc}\sin(2\theta)\right]\dot{v}$	Argument of Latitude Rate
$r = A(1-e\cos(E)) + C_{rs}\sin(2\theta) + C_{rc}\cos(2\theta)$	Corrected Radius
$\dot{r} = Ae\sin(E)\dot{E} + 2\left[C_{rs}\cos(2\theta) - C_{rc}\sin(2\theta)\right]\dot{v}$	Radius Rate
$i = i_0 + IDOT\cdot\Delta t + C_{is}\sin(2\theta) + C_{ic}\cos(2\theta)$	Corrected Inclination
$i' = IDOT + 2\left[C_{is}\cos(2\theta) - C_{ic}\sin(2\theta)\right]\dot{v}$	Inclination Rate
$\Omega = \Omega_0 + \left(\dot{\Omega} - \dot{\Omega}_e\right)\Delta t - \dot{\Omega}_e t_{oe}$	Corrected Longitude of Ascending Node
$\Omega' = \left(\dot{\Omega} - \dot{\Omega}_e\right)$	Longitude of Ascending Node Rate
$x_{orb} = r\cos(u)$ $y_{orb} = r\sin(u)$ $z_{orb} = 0$	Position in Orbital Plane
$\dot{x}_{orb} = \dot{r}\cos(u) - y_{orb}\dot{u}$ $\dot{y}_{orb} = \dot{r}\sin(u) + x_{orb}\dot{u}$ $\dot{z}_{orb} = 0$	Velocity in Orbital Plane
$x = x_{orb}\cos(\Omega) - y_{orb}\cos(i)\sin(\Omega)$ $y = x_{orb}\sin(\Omega) + y_{orb}\cos(i)\cos(\Omega)$ $z_{orb} = y_{orb}\sin(i)$	Position in ECEF

$\dot{x} = \dot{x}_{orb}\cos(\Omega) - \dot{y}_{orb}\cos(i)\sin(\Omega) + y_{orb}\sin(i)\sin(\Omega)i' - y\dot{\Omega}$ $\dot{y} = \dot{x}_{orb}\sin(\Omega) + \dot{y}_{orb}\cos(i)\cos(\Omega) - y_{orb}\sin(i)\cos(\Omega)i' + x\dot{\Omega}$ $\dot{z} = \dot{y}_{orb}\sin(i) + y_{orb}\cos(i)i'$	Velocity in ECEF

The algorithm for the determination of the GLONASS satellite position and velocity is extensively treated in ICD-GLONASS 2008 and is reported below.

The GLONASS broadcast ephemeris contains the satellite position and velocity and the acceleration due to lunar-solar perturbation in the PZ-90.02 ECEF frame (Table 4-3); these data are usually updated every 30 minutes.

Table 4-3 – GLONASS Broadcast Ephemeris

Parameter	**Description**	**Note**
(x, y, z)	Satellite Coordinates at Reference Time	in ECEF (Km)
(V_x, V_y, V_z)	Satellite Velocity Coordinates at Reference Time	in ECEF (Km/s)
$(\ddot{x}, \ddot{y}, \ddot{z})$	Lunar-Solar Acceleration Components	Perturbation Term in ECEF (Km/s^2)
t_b	Reference Time Ephemeris	(s)

To compute the satellite position and velocity at a different epoch from the reference time t_b (usually the epoch of transmission), the satellite motion equations should be numerically integrated using the broadcast parameters as initial values.

The differential equations describing the satellite motion in PZ-90.02 system are:

$$\begin{aligned}
&dx/dt = Vx \\
&dy/dt = Vy \\
&dz/dt = Vz \\
&dV_x/dt = -\frac{\mu}{r^3}x - \frac{3}{2}J_0^2\frac{\mu a_e^2}{r^5}x\left(1 - \frac{5z^2}{r^2}\right) + \omega^2 x + 2\omega V_y + \ddot{x} \\
&dV_y/dt = -\frac{\mu}{r^3}y - \frac{3}{2}J_0^2\frac{\mu a_e^2}{r^5}y\left(1 - \frac{5z^2}{r^2}\right) + \omega^2 y + 2\omega V_y + \ddot{y} \\
&dV_z/dt = -\frac{\mu}{r^3}z - \frac{3}{2}J_0^2\frac{\mu a_e^2}{r^5}z\left(1 - \frac{5z^2}{r^2}\right) + \ddot{z}
\end{aligned} \tag{4-24}$$

where:

$r = \sqrt{x^2 + y^2 + z^2}$ is the distance satellite-Earth's center,

$\mu = 398600.44 \cdot 10^9 \frac{m^3}{s^2}$ is the Earth's Gravitation constant,

$a_e = 6378136m$ is the Earth's semi-major axis;

$J_0^2 = 1082625.7 \cdot 10^{-9}$ is the second zonal harmonic of the geopotential;

$\omega = 7.292115 \cdot 10^{-5}$ is the Earth's rotation rate.

The GLONASS ICD (ICD-GLONASS 2008) recommends using the 4th order Runge-Kutta method for the numerical integration of equation (4-24) and to keep the integration time within the 15 minutes interval around the reference epoch t_b.

The conversion of the satellite positions into WGS84 frame is expressed by formula (2-8).

4.4 GPS PVT Model

In case of GPS only (or GLONASS only) PVT determination using PR and Doppler observables, the measurement models detailed in sections 4.1 and 4.2 can be jointly adopted. Specifically the equations (4-4) and (4-20) are used, implemented in the local level frame ENU; the resulting PVT model can be expressed as:

$$\underline{z} = \begin{pmatrix} \underline{z}_{PR} \\ \underline{z}_{P\dot{R}} \end{pmatrix} = \begin{bmatrix} H_{PR} \\ H_{P\dot{R}} \end{bmatrix} \cdot \underline{\underline{\Delta x}} + \begin{pmatrix} \underline{\varepsilon}_{PR} \\ \underline{\varepsilon}_{P\dot{R}} \end{pmatrix} = H \cdot \underline{\underline{\Delta x}} + \underline{\varepsilon} \qquad (4\text{-}25)$$

where

$\underline{z}$ is the measurement vector, consisting of both *PR* and *PR* derivative measurements corrected by a priori information,

$\underline{\underline{\Delta x}}$ is the state vector, consisting of receiver position, velocity, clock bias and drift error states

$$\underline{\underline{\Delta x}} = \begin{bmatrix} \Delta E & \Delta N & \Delta U & \Delta V_E & \Delta V_N & \Delta V_U & \Delta(c\delta t) & \Delta(c\dot{\delta t}) \end{bmatrix}$$

$\underline{\varepsilon}$ is the vector containing the *PR* and *PR* derivative measurement errors,

H is the geometry matrix, consisting of the *PR* and *PR* derivative geometry matrices H_{PR} and $H_{P\dot{R}}$ in equations (4-8) and (4-23), but properly filled with zeros in correspondence of the missing states as

$$H = \begin{bmatrix} a_E & a_N & a_U & 0 & 0 & 0 & 1 & 0 \\ . & . & . & . & . & . & . & . \\ b_E & b_N & b_U & b_{VE} & b_{VN} & b_{VU} & 0 & 1 \\ . & . & . & . & . & . & . & . \end{bmatrix}$$

To accurately solve the equation (4-25), at least four simultaneous PR measurements and four simultaneous Doppler measurements are necessary.

4.5 GPS/GLONASS Combined PVT Model

In case of combined use of GPS and GLONASS systems, the previous models valid for single system must be slightly changed taking into account that GPS and GLONASS have different time reference scales (see section 2.2.1) (Daly and Misra 1996).

The linearized *PR* measurement equation (4-3) can be re-written differently for GPS and GLONASS systems as:

$$\begin{aligned} z^G &= a_E^G \Delta x + a_N^G \Delta y + a_U^G \Delta z + \Delta\left(c\delta t^G\right) \\ z^R &= a_E^R \Delta x + a_N^R \Delta y + a_U^R \Delta z + \Delta\left(c\delta t^R\right) \end{aligned} \tag{4-26}$$

where the superscripts “G” or “R” indicate that the element is referred to the GPS or GLONASS system.

The term $\Delta\left(c\delta t^G\right)$ is the increment from the linearization point of the offset of the receiver clock with respect to the GPS time and $\Delta\left(c\delta t^R\right)$ is the same for GLONASS.

The *PR* measurement model considering the simultaneous presence of GPS and GLONASS observation is:

$$\underline{z} = \begin{pmatrix} \underline{z}_{PR}^G \\ \underline{z}_{PR}^R \end{pmatrix} = \begin{bmatrix} H_{PR}^G \\ H_{PR}^R \end{bmatrix} \cdot \underline{\Delta x} + \underline{\varepsilon}_{PR} = H \cdot \underline{\Delta x} + \underline{\varepsilon}_{PR} \tag{4-27}$$

where

$\underline{z}$ is the measurement vector, consisting of both GPS and GLONASS *PR* measurements corrected by a priori information,

$\underline{\Delta x}$ is the state vector, consisting of receiver position and clock biases relative to the GPS and GLONASS time

$$\underline{\Delta x} = \left[\Delta E \quad \Delta N \quad \Delta U \quad \Delta\left(c\delta t^G\right) \quad \Delta\left(c\delta t^R\right) \right]^T,$$

$\underline{\varepsilon}_{PR}$ is the vector containing the *PR* errors,

H is the geometry matrix, organized as

$$H = \begin{bmatrix} a_E^G & a_N^G & a_U^G & 1 & 0 \\ \cdot & \cdot & \cdot & \cdot & \cdot \\ a_E^R & a_N^R & a_U^R & 0 & 1 \\ \cdot & \cdot & \cdot & \cdot & \cdot \end{bmatrix}.$$

Usually the system time difference between GPS and GLONASS, herein indicated as δt_{SYS}, is introduced in the second equation of (4-26) (Cai and Gao2009), yielding:

$$\begin{aligned} z^G &= a_E^G \Delta x + a_N^G \Delta y + a_U^G \Delta z + \Delta\left(c\delta t^G\right) \\ z^R &= a_E^R \Delta x + a_N^R \Delta y + a_U^R \Delta z + \Delta\left(c\delta t^G\right) + \Delta\left(c\delta t_{SYS}\right) \end{aligned} \tag{4-28}$$

So in the GPS/GLONASS combined *PR* measurement model (4-27) the state vector $\underline{\Delta x}$ becomes

$$\underline{\Delta x} = \left[\Delta E \quad \Delta N \quad \Delta U \quad \Delta\left(c\delta t^G\right) \quad \Delta\left(c\delta t_{SYS}\right) \right]^T$$

and the geometry matrix H becomes

$$H = \begin{bmatrix} a_E^G & a_N^G & a_U^G & 1 & 0 \\ \cdot & \cdot & \cdot & \cdot & \cdot \\ a_E^R & a_N^R & a_U^R & 1 & 1 \\ \cdot & \cdot & \cdot & \cdot & \cdot \end{bmatrix}.$$

To obtain a combined GPS/GLONASS measurement model, including both *PR* and Doppler observables, equations as (4-23) should be included in the model (4-27); specifically the equation (4-23) should be detailed for GPS and GLONASS cases as:

$$\begin{aligned} z^{G} &= b_{E}^{G}\Delta E + b_{N}^{G}\Delta N + b_{U}^{G}\Delta U + b_{VE}^{G}\Delta V_{E} + b_{VN}^{G}\Delta V_{N} + b_{VU}^{G}\Delta V_{U} + \Delta\left(c\delta\dot{t}^{G}\right) \\ z^{R} &= b_{E}^{R}\Delta E + b_{N}^{R}\Delta N + b_{U}^{R}\Delta U + b_{VE}^{R}\Delta V_{E} + b_{VN}^{R}\Delta V_{N} + b_{VU}^{R}\Delta V_{U} + \Delta\left(c\delta\dot{t}^{R}\right) \end{aligned} \tag{4-29}$$

The receiver clock drifts $c\delta\dot{t}^{G}$ and $c\delta\dot{t}^{R}$ with respect to GPS and GLONASS reference times can be considered the same, because the systems time difference $c\delta t_{SYS}$ is very stable (Cai and Gao 2009) and its derivative can be considered negligible.

The *PR* and Doppler measurement model considering the simultaneous presence of GPS and GLONASS observation is:

$$\underline{z} = \begin{bmatrix} \underline{z}_{PR}^{G} \\ \underline{z}_{PR}^{R} \\ \underline{z}_{P\dot{R}}^{G} \\ \underline{z}_{P\dot{R}}^{R} \end{bmatrix} = \begin{bmatrix} H_{PR}^{G} \\ H_{PR}^{R} \\ H_{P\dot{R}}^{G} \\ H_{P\dot{R}}^{R} \end{bmatrix} \underline{\Delta x} + \underline{\varepsilon} = H \cdot \underline{\Delta x} + \underline{\varepsilon} \tag{4-30}$$

where

$\underline{z}$ is the measurement vector, consisting of both *PR* and *PR* derivative measurements relative to GPS and GLONASS corrected by a priori information,

$\underline{\Delta x}$ is the state vector, consisting of receiver position, velocity, clock bias and drift error states

$$\underline{\Delta x} = \left[\begin{matrix} \Delta E & \Delta N & \Delta U & \Delta V_{E} & \Delta V_{N} & \Delta V_{U} & \Delta\left(c\delta t^{G}\right) & \Delta\left(c\delta\dot{t}\right) & \Delta\left(c\delta t_{SYS}\right) \end{matrix}\right]$$

$\underline{\varepsilon}$ is the vector containing the PR and PR derivative measurement errors of GPS and GLONASS systems,

H is the geometry matrix, consisting of the sub-matrices H_{PR}^{G}, H_{PR}^{R}, $H_{P\dot{R}}^{G}$ and $H_{P\dot{R}}^{R}$ in equations (4-8) and (4-23), but properly filled with zeros in correspondence of the missing states as

$$H = \begin{bmatrix} a_E^G & a_N^G & a_U^G & 0 & 0 & 0 & 1 & 0 & 0 \\ . & . & . & . & . & . & . & . & . \\ a_E^R & a_N^R & a_U^R & 0 & 0 & 0 & 1 & 0 & 1 \\ . & . & . & . & . & . & . & . & . \\ b_E^G & b_N^G & b_U^G & b_{VE}^G & b_{VN}^G & b_{VU}^G & 0 & 1 & 0 \\ . & . & . & . & . & . & . & . & . \\ b_E^R & b_N^R & b_U^R & b_{VE}^R & b_{VN}^R & b_{VU}^R & 0 & 1 & 0 \\ . & . & . & . & . & . & . & . & . \end{bmatrix}$$

The performance of a combined GPS/GLONASS constellation with respect to a single system performance is analyzed in Angrisano et al. 2009a, showing the benefits in terms of coverage and integrity.

Chapter 5 GNSS/INS Integration

In this chapter the main aspects of the GNSS/INS integration are reviewed.

First the complementary nature of the systems is pointed out, then an overview on the different integration strategies and configurations is carried out with details on loose and tight architectures and their differences. Then an implementation approach is provided, describing the measurement and process models for each configuration. Afterwards an algorithm for the direct observation of azimuth is reported and the use of constraints to bound the INS error during GNSS outages is introduced.

All the algorithms adopted in this work are used in real-time; post-processing techniques are only used to build the reference solution to assess the performance of the real-time algorithms and are not described in this work.

5.1 Complementary Nature of GNSS and INS

GNSS and INS systems are complementary in many aspects, shortly described below.

INS short-term errors are relatively small, but they degrade rapidly and are unbounded and so external aiding is necessary (Farrel 2008). On the other hand GNSS systems are more stable in long-term, meaning their errors are effectively time invariant with homogeneous accuracy (Lachapelle 1997). Hence GNSS systems can be used as external aiding to bound INS errors.

INS can provide accurate short-term data with very high rate and can be used to interpolate GNSS trajectory. In addition INS sensors supply data with continuity, while GNSS are subject to outages, caused by signal blocking or interference. For this reasons high-precision inertial sensors (as tactical or superior grade) can be used to bridge GNSS outages; unfortunately this might be not possible with MEMS sensors owing to their large error drift (Abdel-Hamid 2005).

Finally INS systems provide the complete navigation state, including position, velocity and attitude while a single GNSS receiver cannot supply angular information.

5.2 GNSS/INS Integration Strategies

Several approaches can be used to integrate GNSS and INS systems, differing by the “depth” of the interaction and for the shared information between the systems.

The more common strategies are listed below (Petovello 2003):

- Uncoupled Integration
- Loosely Coupled Integration
- Tightly Coupled Integration
- Deep or Ultra-Tight Integration

In the Uncoupled approach, the systems work independently providing two distinct navigation solutions; usually GNSS one is considered more accurate and is adopted when available as system solution. Moreover GNSS solution is used to correct (or reset) the INS solution, but without estimating the causes of the sensor drift (as happens in the other integration approaches). In absence of GNSS data the system solution is entirely supplied by the inertial sensor, which tends to drift rapidly according to its grade. For this limitation the Uncoupled strategy is not commonly used.

The Loosely and Tightly Coupled strategies are the more common integration techniques and are implemented in this research; detailed information on them are in the next sections.

In the Loosely Coupled approach the GNSS solution is merged with the inertial based information to obtain the final output of the integrated system, while in the Tightly approach the integration is “deeper”, because the GNSS raw measurements are directly combined with the INS information in a suitable filter.

In the Ultra-Tight integration the GNSS and INS devices no longer work as independent systems, GNSS measurements are used to estimate INS errors and INS measurements to aid GNSS receiver tracking loops; this integration is clearly at deep level and requires access to receiver’s firmware and so is usually implemented by receiver manufacturers or with software receivers (Petovello 2003, Gautier and Parkinson 2003).

5.2.1 Loosely Coupled Integration

The Loosely Coupled (LC) strategy, also referred to as “decentralized”, is realized including a KF to combine INS and GNSS navigation parameters and another block (a further KF or a LS estimator) is used to estimate the GNSS navigation solution using the raw measurements. The LC scheme is showed in Figure 5-1.

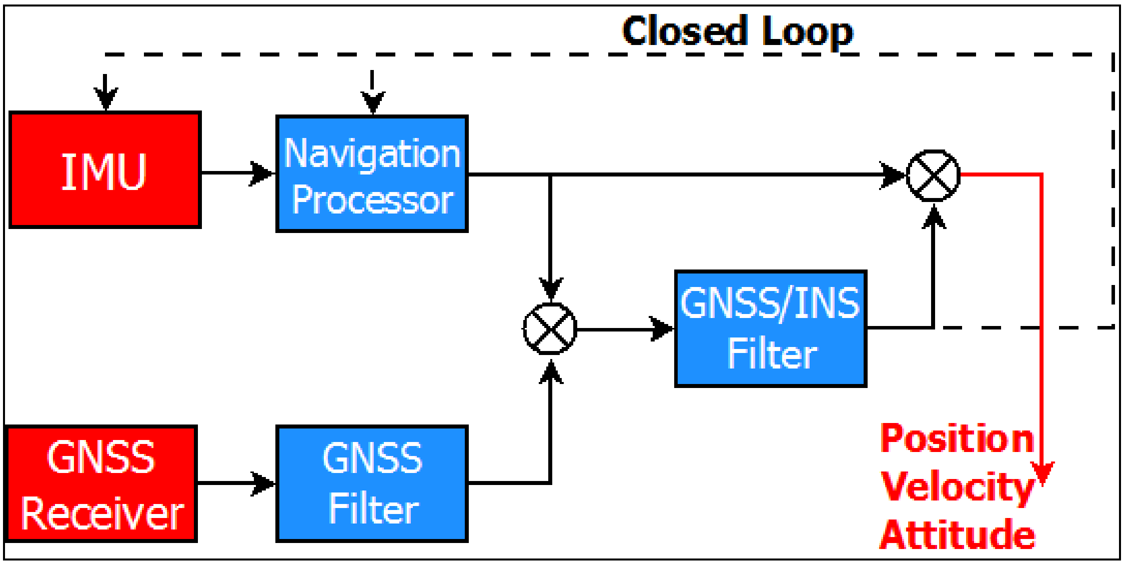

Figure 5-1 – Loosely Coupled Scheme

The raw GNSS measurements from the receiver are independently processed in a dedicated block. Herein a LS estimator is preferred to simplify a direct LC/TC comparison and a single point mode is performed, adopting as raw measurements only pseudorange and Doppler observables.

The inertial solution is obtained applying the mechanization equations (2-18) for a strapdown configuration to the accelerations and angular rates from the IMU. The difference between INS and GNSS position and velocity are used as input measurements to the KF; the associated measurement covariance matrix R input to KF is the LS covariance matrix, taking into account the uncertainty of the aiding source, i.e. the GNSS position and velocity.

Instead of a simple LS estimator, to process the GNSS measurements a WLS estimator can be adopted to take into account the different inherent accuracies of the observables and/or the different “trust” associated to single measurement according to a chosen criterion (e.g. the elevation of a satellite).

The LC scheme in Figure 5-1 operates in closed loop mode, which consists of sending back the estimated INS errors from the KF to the mechanization and IMU blocks; in detail the estimated navigation errors are sent back to correct the INS state and the sensor estimated errors are used to compensate raw IMU measurements according to (2-26). The alternative mode is the open loop mode, where the INS operates independently from the KF estimator and the estimated errors are not sent back to mechanization and IMU blocks; in this way the inertial sensor errors remain uncorrected and inertial navigation state errors grow rapidly introducing large errors in the integrated systems. The open-loop mode can be used only for high-end inertial sensors, characterized by small errors; usually for low-cost or MEMS based inertial systems the closed-loop is necessary (Godha 2006).

5.2.2 Tightly Coupled Integration

The Tightly Coupled (TC) strategy, also referred to as "centralized", is realized processing INS navigation parameters and GNSS raw measurements in a central KF. The TC scheme is showed in Figure 5-2.

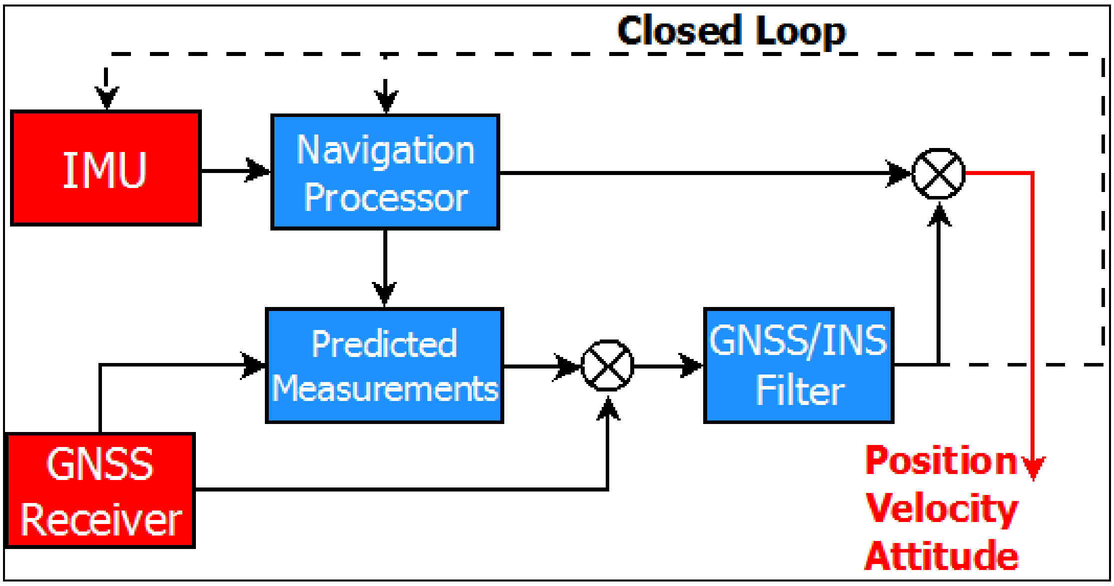

Figure 5-2 – Tightly Coupled Scheme

It can be noticed that the GNSS raw measurements are not processed in a separate filter as in the LC case, but are directly combined in a unique filter.

The difference between PR and Doppler measurements and INS-predicted measurements is used as input of the KF; the associated measurements covariance matrix is defined taking into account the inherent accuracies of the GNSS observables and elevation-dependent accuracy of the single measurements as in the LC case. The INS-predicted measurements (range and range-rate) are computed using the GNSS satellite position and velocity from the ephemerides (section 4.3) and user position and velocity from the INS.

The KF state vector size in the TC approach is increased with respect to the LC case, because the clock states are also included.

The closed and open-loop concepts are valid also in the TC case.

5.2.3 Loose versus Tight

Loose and Tight integrations basically differ for the type of information shared between the individual systems: processed GNSS solution is merged with INS solution in the first strategy and raw GNSS measurements are combined with INS-predicted measurements in the second.

This yields to a different structure of the two architectures, with two separate filters in the Loose coupling and only a centralized filter in the Tight.

The separate filters in the Loose have the advantage to be smaller than the corresponding centralized Tight filter, yielding faster processing times. On the other hand with separate filters in LC (if a Kalman filter is used to perform the GNSS solution), the process noise is added twice, affecting the system performance (Petovello 2003). If a Least Square estimator is used (as in this work) to obtain the GNSS solution, this problem is not present, simplifying the Loosely/Tightly comparison, which is one of the purpose of this research.

Moreover the LC approach is more robust, because INS and GNSS operate separately and so can continue to provide navigation solution also in case of failure of one system (Godha 2006).

On the other hand LC has the great disadvantage to be unable to provide GNSS output in case of partial availability (e.g. less than four PR in GPS only mode); for this reason TC strategy is usually preferred in applications with bad visibility conditions as urban canyons.

5.3 Loosely Coupled Implementation

In this work the LC architecture is implemented adopting a LS estimator to process the raw pseudorange and Doppler measurements in single point positioning mode and in real time; the details of the algorithm are in the section 5.3.1.

The integration GNSS/INS is implemented with a KF described in the section 5.3.2, with details on both the measurement and the process models.

5.3.1 GNSS LS Estimator

The LS estimator to process PR and Doppler observations is based on the measurement model (4-25) in GPS only (or GLONASS only) case and on model (4-30) in combined GPS/GLONASS case.

In a signal-degraded environment (e.g. urban canyons), the estimated variances of the GNSS solution output from an unweighted LS may be overly optimistic due to the lack of redundancy and possible multiple blunders in a single epoch (Mezentsev 2005); this information is unrealistic and strongly affects the integrated navigation solution. It was empirically demonstrated in this research that the WLS approach partially solves this problem.

A WLS approach takes into account the different uncertainty of the measurements (Brogan 1981) and the obtained solution and covariance matrix are:

$$\underline{\Delta\hat{x}}_{WLS} = \left(H^T W H\right)^{-1} H^T W \cdot \underline{z} \tag{5-1}$$

$$C_{\hat{x}} = \left(H^T W H\right)^{-1} \tag{5-2}$$

In literature different weighting criterions have been used, weighting the measurements according to certain observation parameters such as signal-to-noise ratio (Wieser 2001), satellite elevation (Satirapod and Wang 2000) or user equivalent range error (UERE) (Sairo et al. 2003).

In this research the strategy proposed in Petovello 2003 is adopted, scaling the standard deviation of the measurement error at the Zenith by $1/\sin\left(el\right)$, where el is the satellite elevation angle. So the weight associated with the generic measurement is:

$$w_{ii} = \frac{\sin\left(el\right)}{\sigma_m^2} \tag{5-3}$$

where

w_{ii} is the i^{th} element of the diagonal of the matrix W,

σ_m^2 is the measurement variance, equal to the PR variance σ_{PR}^2 or to the Doppler variance $\sigma_{P\dot{R}}^2$.

5.3.2 GNSS/INS Filter

The main aim of the GNSS/INS filter in the LC architecture is to estimate the errors of the INS system and this is accomplished using the GNSS solution as external aiding (Godha 2006). The design of the KF process and measurement models is discussed below.

Process Model

The basic state vector to estimate consists of the nine navigation parameter errors, i.e. the three position errors, the three velocity errors and the three attitude errors and their behavior is expressed by equation (2-28), which is reported below:

$$\delta\dot{\underline{x}}^n = \begin{bmatrix} \delta\dot{\underline{r}}^n \\ \delta\dot{\underline{v}}^n \\ \dot{\underline{\varepsilon}}^n \end{bmatrix} = \begin{bmatrix} F_{rr} & F_{rv} & F_{r\varepsilon} \\ F_{vr} & F_{vv} & F_{v\varepsilon} \\ F_{\varepsilon r} & F_{\varepsilon v} & F_{\varepsilon\varepsilon} \end{bmatrix} \cdot \begin{bmatrix} \delta\underline{r}^n \\ \delta\underline{v}^n \\ \underline{\varepsilon}^n \end{bmatrix} + \begin{bmatrix} 0_{3x1} \\ R_b^n \delta\underline{f}^b \\ R_b^n \delta\underline{w}^b \end{bmatrix} = F \cdot \delta\underline{x}^n + G \cdot \underline{w} \tag{5-4}$$

where

$F = \begin{bmatrix} F_{rr} & F_{rv} & F_{r\varepsilon} \\ F_{vr} & F_{vv} & F_{v\varepsilon} \\ F_{\varepsilon r} & F_{\varepsilon v} & F_{\varepsilon\varepsilon} \end{bmatrix}$ is the dynamic matrix,

$\delta\underline{x}^n = \begin{bmatrix} \delta\underline{r}^n & \delta\underline{v}^n & \underline{\varepsilon}^n \end{bmatrix}^T$ is the state vector, in turn consisting of the position errors $\delta\underline{r}^n = \begin{bmatrix} \delta\varphi & \delta\lambda & \delta h \end{bmatrix}^T$, the velocity errors $\delta\underline{v}^n = \begin{bmatrix} \delta V_E & \delta V_N & \delta V_U \end{bmatrix}^T$ and attitude errors $\underline{\varepsilon}^n = \begin{bmatrix} \varepsilon_E & \varepsilon_N & \varepsilon_U \end{bmatrix}^T$

$G = \begin{bmatrix} 0_{3x3} & 0_{3x3} \\ R_b^n & 0_{3x3} \\ 0_{3x3} & R_b^n \end{bmatrix}$ is the shaping matrix,

$\underline{w} = \begin{bmatrix} \delta\underline{f}^b & \delta\underline{w}^b \end{bmatrix}^T$ is the forcing vector, consisting of the errors in the measured specific force and in the measured angular rates.

Theoretically the equation (5-4) could be used as process model in the KF, but this not normally done because the inertial measurement errors do not meet the KF assumptions of zero-mean white noise and Gaussian behavior (Petovello 2003). Additional states must be added to the INS error model in order to account for the effects of the inertial sensor errors and the process of adding these states is called state augmentation (Gaylor 2003).

The inertial sensor errors are described in section 2.3.4; typically for high-end IMUs only the bias drift and the noise have to be considered and the measurement errors in equation (5-4) can be expressed as:

$$\begin{aligned} \underline{\delta f}^b &= \underline{\delta b}_a + \underline{\eta}_a \\ \underline{\delta w}^b &= \underline{\delta b}_g + \underline{\eta}_g \end{aligned} \tag{5-5}$$

where

$\underline{\delta b}_a = \begin{bmatrix} \delta b_{ax} & \delta b_{ay} & \delta b_{az} \end{bmatrix}^T$ and $\underline{\delta b}_g = \begin{bmatrix} \delta b_{gx} & \delta b_{gy} & \delta b_{gz} \end{bmatrix}^T$ are the accelerometer and the gyro biases,

$\underline{\eta}_a = \begin{bmatrix} \eta_{ax} & \eta_{ay} & \eta_{az} \end{bmatrix}^T$ and $\underline{\eta}_g = \begin{bmatrix} \eta_{gx} & \eta_{gy} & \eta_{gz} \end{bmatrix}^T$ are the accelerometer and the gyro noises, whose spectral densities are $\underline{q}_a$ and $\underline{q}_g$.

The bias drift must be modeled as an appropriate stochastic process and is often modeled as a first-order Gauss-Markov process (Petovello 2003) represented by the equations:

$$\begin{aligned} \delta \dot{b}_{ai} &= -\frac{1}{\tau_{bai}} \delta b_{ai} + \eta_{bai} \\ \delta \dot{b}_{gi} &= -\frac{1}{\tau_{bgi}} \delta b_{gi} + \eta_{bgi} \end{aligned} \tag{5-6}$$

where

the subscript “*i*” indicates the axis, i.e. it can be $i = x, y, z$,

$\underline{\tau}_{ba} = \begin{bmatrix} \tau_{bax} & \tau_{bay} & \tau_{baz} \end{bmatrix}^T$ are the correlation times for the accelerometers,

$\underline{\tau}_{bg} = \begin{bmatrix} \tau_{bgx} & \tau_{bgy} & \tau_{bgz} \end{bmatrix}^T$ are the correlation times for the gyros,

$\underline{\eta}_{ba} = \begin{bmatrix} \eta_{bax} & \eta_{bay} & \eta_{baz} \end{bmatrix}^T$ and $\underline{\eta}_{bg} = \begin{bmatrix} \eta_{bgx} & \eta_{bgy} & \eta_{bgz} \end{bmatrix}^T$ are the Gauss-Markov process driving noises, whose spectral densities are $\underline{q}_{ba} = \begin{bmatrix} q_{bax} & q_{bay} & q_{baz} \end{bmatrix}^T$ and $\underline{q}_{bg} = \begin{bmatrix} q_{bgx} & q_{bgy} & q_{bgz} \end{bmatrix}^T$.

The Gauss-Markov correlation time and temporal standard deviation can be obtained using the autocorrelation analysis (Nassar 2003, El-Sheimy 2004) and the spectral density of the Gauss-Markov process driving noise can be computed as:

$$
\begin{aligned}
q_{bai} &= \frac{2\sigma_{bai}^2}{\tau_{bai}} \\
q_{bgi} &= \frac{2\sigma_{bgi}^2}{\tau_{bgi}}
\end{aligned}
\tag{5-7}
$$

where

$\underline{\sigma}_{ba} = \begin{bmatrix} \sigma_{bax} & \sigma_{bay} & \sigma_{baz} \end{bmatrix}^T$ and $\underline{\sigma}_{bg} = \begin{bmatrix} \sigma_{bgx} & \sigma_{bgy} & \sigma_{bgz} \end{bmatrix}^T$ are the Gauss-Markov process temporal standard deviations.

Augmenting the basic state vector with the sensor bias states yields a 15 states filter, whose process model is:

$$
\begin{bmatrix} \underline{\delta \dot{r}}^n \\ \underline{\delta \dot{v}}^n \\ \underline{\dot{\varepsilon}}^n \\ \underline{\delta \dot{b}}_a \\ \underline{\delta \dot{b}}_g \end{bmatrix} = \begin{bmatrix} F_{rr} & F_{rv} & F_{r\varepsilon} & 0_3 & 0_3 \\ F_{vr} & F_{vv} & F_{v\varepsilon} & R_b^n & 0_3 \\ F_{\varepsilon r} & F_{\varepsilon v} & F_{\varepsilon\varepsilon} & 0_3 & R_b^n \\ 0_3 & 0_3 & 0_3 & \beta_{ba} & 0_3 \\ 0_3 & 0_3 & 0_3 & 0_3 & \beta_{bg} \end{bmatrix} \cdot \begin{bmatrix} \underline{\delta r}^n \\ \underline{\delta v}^n \\ \underline{\varepsilon}^n \\ \underline{\delta b}_a \\ \underline{\delta b}_g \end{bmatrix} + \begin{bmatrix} 0_3 & 0_3 & 0_3 & 0_3 \\ R_b^n & 0_3 & 0_3 & 0_3 \\ 0_3 & R_b^n & 0_3 & 0_3 \\ 0_3 & 0_3 & I_3 & 0_3 \\ 0_3 & 0_3 & 0_3 & I_3 \end{bmatrix} \cdot \begin{bmatrix} \underline{\eta}_a \\ \underline{\eta}_g \\ \underline{\eta}_{ba} \\ \underline{\eta}_{bg} \end{bmatrix}
\tag{5-8}
$$

where

$$
\beta_{ba} = \begin{bmatrix} -1/\tau_{bax} & 0 & 0 \\ 0 & -1/\tau_{bay} & 0 \\ 0 & 0 & -1/\tau_{baz} \end{bmatrix} \text{ and } \beta_{bg} = \begin{bmatrix} -1/\tau_{bgx} & 0 & 0 \\ 0 & -1/\tau_{bgy} & 0 \\ 0 & 0 & -1/\tau_{bgz} \end{bmatrix}.
$$

$\underline{\delta x} = \begin{bmatrix} \underline{\delta r}^n & \underline{\delta v}^n & \underline{\varepsilon}^n & \underline{\delta b}_a & \underline{\delta b}_g \end{bmatrix}^T$ is the 15 parameters state vector.

Typically for low cost MEMS inertial sensors, the turn on bias and the scale factor errors are high and must be taken into account; although deterministic in nature, they vary from one turn on to another and a calibration procedure should be necessary before each mission. However it is not feasible to calibrate the sensors so frequently and so a possible solution is to stochastically model these errors and to include them in the process model of a KF in order to estimate them (Godha 2006).

The turn on bias can be modeled as a random constant process, because it remains constant for a particular run (Godha 2006). An alternative approach can be to include both turn on bias and bias drift in a single term; this idea is supported by their high correlation (Bancroft 2008), which shows that they represent the same phenomenon.

This approach is convenient from the computational point of view, because it introduces a saving of six states (three turn on accelerometer biases and three turn on gyro biases) and the KF process model remains formally identical to (5-8).

Usually it is not possible to split the bias and the scale factor error to model them separately; a possible way can be to lump them together and model them collectively or alternatively to use some a priori information about the parameters (e.g. as discussed in general terms in Petovello 2009). The second approach is herein used in which the scale factor is assumed to be slowing varying with time and so it can be modeled as first-order Gauss-Markov process with large correlation time (Godha 2006), whose equation is:

$$\begin{aligned} \delta\dot{S}_{ai} &= -\frac{1}{\tau_{sai}}\delta S_{ai} + \eta_{sai} \\ \delta\dot{S}_{gi} &= -\frac{1}{\tau_{sgi}}\delta S_{gi} + \eta_{sgi} \end{aligned} \tag{5-9}$$

where

$\underline{\delta S}_a = \begin{bmatrix} \delta S_{ax} & \delta S_{ay} & \delta S_{az} \end{bmatrix}^T$ and $\underline{\delta S}_g = \begin{bmatrix} \delta S_{gx} & \delta S_{gy} & \delta S_{gz} \end{bmatrix}^T$ are the accelerometer and the gyro scale factors,

$\underline{\tau}_{sa} = \begin{bmatrix} \tau_{sax} & \tau_{say} & \tau_{saz} \end{bmatrix}^T$ are the correlation times for the accelerometer scale factors,

$\underline{\tau}_{sg} = \begin{bmatrix} \tau_{sgx} & \tau_{sgy} & \tau_{sgz} \end{bmatrix}^T$ are the correlation times for the gyro scale factors,

$\underline{\eta}_{sa} = \begin{bmatrix} \eta_{sax} & \eta_{say} & \eta_{saz} \end{bmatrix}^T$ and $\underline{\eta}_{sg} = \begin{bmatrix} \eta_{sgx} & \eta_{sgy} & \eta_{sgz} \end{bmatrix}^T$ are the Gauss-Markov process driving noises, whose spectral densities $\underline{q}_{sa} = \begin{bmatrix} q_{sax} & q_{say} & q_{saz} \end{bmatrix}^T$ and $\underline{q}_{sg} = \begin{bmatrix} q_{sgx} & q_{sgy} & q_{sgz} \end{bmatrix}^T$ can be computed as:

$$\begin{aligned} q_{sai} &= \frac{2\sigma_{sai}^2}{\tau_{sai}} \\ q_{sgi} &= \frac{2\sigma_{sgi}^2}{\tau_{sgi}} \end{aligned} \tag{5-10}$$

where

$\underline{\sigma}_{sa} = \begin{bmatrix} \sigma_{sax} & \sigma_{say} & \sigma_{saz} \end{bmatrix}^T$ and $\underline{\sigma}_{sg} = \begin{bmatrix} \sigma_{sgx} & \sigma_{sgy} & \sigma_{sgz} \end{bmatrix}^T$ are the Gauss-Markov process temporal standard deviations.

Augmenting the 15 state model (5-8) with the scale factor states yields a 21 states model as shown below:

$$\begin{bmatrix} \underline{\delta\dot{r}}^n \\ \underline{\delta\dot{v}}^n \\ \underline{\dot{\varepsilon}}^n \\ \underline{\delta\dot{b}}_a \\ \underline{\delta\dot{b}}_g \\ \underline{\delta\dot{S}}_a \\ \underline{\delta\dot{S}}_g \end{bmatrix} = \begin{bmatrix} F_{rr} & F_{rv} & F_{r\varepsilon} & 0_3 & 0_3 & 0_3 & 0_3 \\ F_{vr} & F_{vv} & F_{v\varepsilon} & R_b^n & 0_3 & R_b^n \cdot F^b & 0_3 \\ F_{\varepsilon r} & F_{\varepsilon v} & F_{\varepsilon\varepsilon} & 0_3 & R_b^n & 0_3 & R_b^n \cdot W^b \\ 0_3 & 0_3 & 0_3 & \beta_{ba} & 0_3 & 0_3 & 0_3 \\ 0_3 & 0_3 & 0_3 & 0_3 & \beta_{bg} & 0_3 & 0_3 \\ 0_3 & 0_3 & 0_3 & 0_3 & 0_3 & \beta_{sa} & 0_3 \\ 0_3 & 0_3 & 0_3 & 0_3 & 0_3 & 0_3 & \beta_{sg} \end{bmatrix} \cdot \begin{bmatrix} \underline{\delta r}^n \\ \underline{\delta v}^n \\ \underline{\varepsilon}^n \\ \underline{\delta b}_a \\ \underline{\delta b}_g \\ \underline{\delta S}_a \\ \underline{\delta S}_g \end{bmatrix}$$

$$+ \begin{bmatrix} 0_3 & 0_3 & 0_3 & 0_3 & 0_3 & 0_3 \\ R_b^n & 0_3 & 0_3 & 0_3 & 0_3 & 0_3 \\ 0_3 & R_b^n & 0_3 & 0_3 & 0_3 & 0_3 \\ 0_3 & 0_3 & I_3 & 0_3 & 0_3 & 0_3 \\ 0_3 & 0_3 & 0_3 & I_3 & 0_3 & 0_3 \\ 0_3 & 0_3 & 0_3 & 0_3 & I_3 & 0_3 \\ 0_3 & 0_3 & 0_3 & 0_3 & 0_3 & I_3 \end{bmatrix} \cdot \begin{bmatrix} \underline{\eta}_a \\ \underline{\eta}_g \\ \underline{\eta}_{ba} \\ \underline{\eta}_{bg} \\ \underline{\eta}_{sa} \\ \underline{\eta}_{sg} \end{bmatrix} \qquad (5\text{-}11)$$

where

$$\beta_{sa} = \begin{bmatrix} -1/\tau_{sax} & 0 & 0 \\ 0 & -1/\tau_{say} & 0 \\ 0 & 0 & -1/\tau_{saz} \end{bmatrix} \text{ and } \beta_{sg} = \begin{bmatrix} -1/\tau_{sgx} & 0 & 0 \\ 0 & -1/\tau_{sgy} & 0 \\ 0 & 0 & -1/\tau_{sgz} \end{bmatrix},$$

$$F^b = diag\left(\underline{f}^b\right) = \begin{bmatrix} f_x & 0 & 0 \\ 0 & f_y & 0 \\ 0 & 0 & f_z \end{bmatrix} \text{ and } W^b = diag\left(\underline{w}^b\right) = \begin{bmatrix} w_x & 0 & 0 \\ 0 & w_y & 0 \\ 0 & 0 & w_z \end{bmatrix},$$

the notation $diag(\bullet)$ represents a diagonal matrix whose diagonal elements are the components of the vector between the brackets,

$\underline{\delta x} = \begin{bmatrix} \underline{\delta r}^n & \underline{\delta v}^n & \underline{\varepsilon}^n & \underline{\delta b}_a & \underline{\delta b}_g & \underline{\delta S}_a & \underline{\delta S}_g \end{bmatrix}^T$ is the 21 parameters state vector.

The corresponding process noise spectral density matrix is expressed as:

$$Q = \begin{bmatrix} \underline{q}_a & 0_3 & 0_3 & 0_3 & 0_3 & 0_3 \\ 0_3 & \underline{q}_g & 0_3 & 0_3 & 0_3 & 0_3 \\ 0_3 & 0_3 & \underline{q}_{ba} & 0_3 & 0_3 & 0_3 \\ 0_3 & 0_3 & 0_3 & \underline{q}_{bg} & 0_3 & 0_3 \\ 0_3 & 0_3 & 0_3 & 0_3 & \underline{q}_{sa} & 0_3 \\ 0_3 & 0_3 & 0_3 & 0_3 & 0_3 & \underline{q}_{sg} \end{bmatrix} \tag{5-12}$$

In this work the experimentation is carried out on a specific low cost MEMS-based IMU, i.e. the Crista IMU sensor from the Cloud Cap Technology (Crista Interface/Operation Document 2004).

The elements of the spectral density matrix (5-12) for Crista IMU are obtained using the methods defined in the current section and in 2.3.4 and are (Godha 2006, Li 2009):

$$\begin{aligned}
&\sqrt{\underline{q}_a} = 300e-6 \quad g/\sqrt{Hz} \\
&\sqrt{\underline{q}_g} = 220 \quad (\deg/h)/\sqrt{Hz} \\
&\left.\begin{aligned} \sigma_{ba} &= 0.0077 \quad (m/s^2) \\ \tau_{ba} &= 270 \quad s \end{aligned}\right\} \quad \sqrt{\underline{q}_{ba}} = 6.62e-4 \\
&\left.\begin{aligned} \sigma_{bg} &= 192 \quad (\deg/h) \\ \tau_{bg} &= 350 \quad s \end{aligned}\right\} \quad \sqrt{\underline{q}_{bg}} = 0.004 \\
&\left.\begin{aligned} \sigma_{sa} &= 10000 \quad (PPM) \\ \tau_{sa} &= 18000 \quad s \end{aligned}\right\} \quad \sqrt{\underline{q}_{sa}} = 1.0541e-4 \\
&\left.\begin{aligned} \sigma_{sg} &= 10000 \quad (PPM) \\ \tau_{sg} &= 18000 \quad s \end{aligned}\right\} \quad \sqrt{\underline{q}_{sg}} = 1.0541e-4
\end{aligned} \tag{5-13}$$

Measurement Model

The measurement model of the GNSS/INS filter in the LC architecture has the typical form:

$$\underline{\delta z} = H \cdot \underline{\delta x} + \underline{\eta} \tag{5-14}$$

The measurement vector consists of the differences between the GNSS position and velocity and the INS position and velocity as shown below:

$$\underline{\delta z} = \begin{bmatrix} \underline{r}^n_{GNSS} - \underline{r}^n_{INS} \\ \underline{V}^n_{GNSS} - \underline{V}^n_{INS} \end{bmatrix} \tag{5-15}$$

The geometry matrix is designed in order to observe directly the position and velocity misclosures as shown below:

$$H = \begin{bmatrix} I_3 & 0_3 & 0_{3x(n-6)} \\ 0_3 & I_3 & 0_{3x(n-6)} \end{bmatrix} \tag{5-16}$$

where n is the number of states of the filter.

The measurement noise $\underline{\eta}$ is characterized by a spectral density R assumed equal to the position/velocity covariance matrix from the GNSS only filter (equation (5-2).

5.3.3 Kalman Filter State Vector Transformation

Position error states expressed in radians are typically very small and can cause numerical instability inside the Kalman filter computations (Shin 2001), so it is preferred to express the position error states in East, North and Up coordinates.

In general a state vector transformation involves a change in the process and in the measurement models.

Recall the process model in the linear form (3-2):

$$\underline{\dot{x}} = F \cdot \underline{x} + G \cdot \underline{w} \tag{5-17}$$

$\underline{x}$ is the "old" state vector, i.e. the state vector before the transformation.

Call $\underline{x}'$ the "new" state vector, i.e. the state vector after the transformation; the transformation between the two state vectors is performed by the matrix T according to the equations:

$$\begin{aligned} \underline{x}' &= T \cdot \underline{x} \\ \underline{x} &= T^{-1} \cdot \underline{x}' \end{aligned} \tag{5-18}$$

Taking the derivative of the first equation of (5-18) and substituting the second of (5-18) and the equation (5-17), yields:

$$\begin{aligned}\dot{\underline{x}}' &= \dot{T}\underline{x} + T\dot{\underline{x}} = \dot{T}T^{-1}\underline{x}' + TF\underline{x} + TG\underline{w} = \\ &= \left(\dot{T}T^{-1} + TFT^{-1}\right)\underline{x}' + TG\underline{w} = F'\underline{x}' + G'\underline{w}\end{aligned} \tag{5-19}$$

where

F' and G' are the new dynamic matrix and shaping matrix respectively.

In the specific case of the GNSS/INS filter in the LC approach, the old and the new state vectors are (21 states):

$$\begin{aligned}\underline{x} &= \left[\underline{\delta r}^n \quad \underline{\delta v}^n \quad \underline{\varepsilon}^n \quad \underline{\delta b}_a \quad \underline{\delta b}_g \quad \underline{\delta S}_a \quad \underline{\delta S}_g\right]^T \\ \underline{x}' &= \left[\underline{\delta P}^n \quad \underline{\delta v}^n \quad \underline{\varepsilon}^n \quad \underline{\delta b}_a \quad \underline{\delta b}_g \quad \underline{\delta S}_a \quad \underline{\delta S}_g\right]^T\end{aligned} \tag{5-20}$$

and the transformation matrix T is:

$$T = \begin{bmatrix} A & 0_{3x(n-3)} \\ 0_{(n-3)x3} & I_{n-3} \end{bmatrix} \tag{5-21}$$

where

$\underline{\delta P}^n = \left[\delta E \quad \delta N \quad \delta U\right]^T$ is the position error state expressed in the ENU frame and

$A = \begin{bmatrix} 0 & (N+h)\cos\varphi & 0 \\ M+h & 0 & 0 \\ 0 & 0 & 1 \end{bmatrix}$ is the matrix to transform $\underline{\delta r}^n$ in $\underline{\delta P}^n$ as shown below

$$\begin{bmatrix} \delta E \\ \delta N \\ \delta U \end{bmatrix} = \begin{bmatrix} 0 & (N+h)\cos\varphi & 0 \\ M+h & 0 & 0 \\ 0 & 0 & 1 \end{bmatrix} \cdot \begin{bmatrix} \delta\varphi \\ \delta\lambda \\ \delta h \end{bmatrix}.$$

The process model with the new state vector, obtained applying the equation (5-19), is:

$$\begin{bmatrix} \underline{\delta \dot{P}}^n \\ \underline{\delta \dot{v}}^n \\ \underline{\dot{\varepsilon}}^n \\ \underline{\delta \dot{b}}_a \\ \underline{\delta \dot{b}}_g \\ \underline{\delta \dot{S}}_a \\ \underline{\delta \dot{S}}_g \end{bmatrix} = \begin{bmatrix} F_{PP} & F_{Pv} & F_{P\varepsilon} & 0_3 & 0_3 & 0_3 & 0_3 \\ F_{vP} & F_{vv} & F_{v\varepsilon} & R_b^n & 0_3 & R_b^n \cdot F^b & 0_3 \\ F_{\varepsilon P} & F_{\varepsilon v} & F_{\varepsilon\varepsilon} & 0_3 & R_b^n & 0_3 & R_b^n \cdot W^b \\ 0_3 & 0_3 & 0_3 & \beta_{ba} & 0_3 & 0_3 & 0_3 \\ 0_3 & 0_3 & 0_3 & 0_3 & \beta_{bg} & 0_3 & 0_3 \\ 0_3 & 0_3 & 0_3 & 0_3 & 0_3 & \beta_{sa} & 0_3 \\ 0_3 & 0_3 & 0_3 & 0_3 & 0_3 & 0_3 & \beta_{sg} \end{bmatrix} \cdot \begin{bmatrix} \underline{\delta P}^n \\ \underline{\delta v}^n \\ \underline{\varepsilon}^n \\ \underline{\delta b}_a \\ \underline{\delta b}_g \\ \underline{\delta S}_a \\ \underline{\delta S}_g \end{bmatrix}$$

$$+ \begin{bmatrix} 0_3 & 0_3 & 0_3 & 0_3 & 0_3 & 0_3 \\ R_b^n & 0_3 & 0_3 & 0_3 & 0_3 & 0_3 \\ 0_3 & R_b^n & 0_3 & 0_3 & 0_3 & 0_3 \\ 0_3 & 0_3 & I_3 & 0_3 & 0_3 & 0_3 \\ 0_3 & 0_3 & 0_3 & I_3 & 0_3 & 0_3 \\ 0_3 & 0_3 & 0_3 & 0_3 & I_3 & 0_3 \\ 0_3 & 0_3 & 0_3 & 0_3 & 0_3 & I_3 \end{bmatrix} \cdot \begin{bmatrix} \underline{\eta}_a \\ \underline{\eta}_g \\ \underline{\eta}_{ba} \\ \underline{\eta}_{bg} \\ \underline{\eta}_{sa} \\ \underline{\eta}_{sg} \end{bmatrix} \qquad (5\text{-}22)$$

where

$$F_{PP} = \begin{pmatrix} 0 & \dfrac{V_E \tan\varphi}{M+h} & \dfrac{-V_E}{N+h} \\ 0 & 0 & \dfrac{-V_N}{M+h} \\ 0 & 0 & 0 \end{pmatrix},$$

$$F_{Pv} = I_3,$$

$$F_{P\varepsilon} = 0_3,$$

$$F_{vP} = \begin{pmatrix} 0 & \dfrac{2\sigma\left(V_U \sin\varphi + V_N \cos\varphi\right)}{M+h} + \dfrac{V_E V_N}{(M+h)(N+h)\cos^2\varphi} & \dfrac{V_E V_U - V_E V_N \tan\varphi}{(N+h)^2} \\ 0 & \dfrac{-2\sigma V_E \cos\varphi}{M+h} - \dfrac{V_E^2}{(M+h)(N+h)\cos^2\varphi} & \dfrac{V_N V_U}{(M+h)^2} + \dfrac{V_E^2 \tan\varphi}{(N+h)^2} \\ 0 & \dfrac{-2\sigma V_E \sin\varphi}{M+h} & \dfrac{-V_E^2}{(N+h)^2} - \dfrac{V_N^2}{(M+h)^2} + \dfrac{2g}{R+h} \end{pmatrix},$$

$$F_{\varepsilon P}=\begin{pmatrix} 0 & 0 & \dfrac{-V_N}{(M+h)^2} \\ 0 & \dfrac{\sigma\sin\varphi}{M+h} & \dfrac{V_E}{(N+h)^2} \\ 0 & \dfrac{-\sigma\cos\varphi}{M+h}-\dfrac{V_E}{(M+h)(N+h)\cos^2\varphi} & \dfrac{V_E\tan\varphi}{(N+h)^2} \end{pmatrix}.$$

In the measurement model (5-14), the measurements vector can be transformed as:

$$\underline{\delta z}=\begin{bmatrix} \underline{P}^n_{GNSS}-\underline{P}^n_{INS} \\ \underline{V}^n_{GNSS}-\underline{V}^n_{INS} \end{bmatrix} \tag{5-23}$$

and the design matrix remains as in (5-16), considering the new state vector expression (second equation in (5-20)). The units of $\left(\underline{P}^n_{GNSS}-\underline{P}^n_{INS}\right)$ are meters.

The spectral density of the measurement noise must take into account that the position error states are expressed in the ENU frame.

5.4 Tightly Coupled Implementation

In this work the TC architecture is implemented adopting a central KF to process the un-differenced GNSS raw pseudorange and Doppler measurements and the INS-derived corresponding observations; the details on both the measurement and the process models are in the section 5.4.1.

5.4.1 GNSS/INS Filter

The main aim of the GNSS/INS filter in the TC architecture is to estimate the errors of the INS system to correct the INS solution and to compensate the IMU sensor errors (Figure 5-2), using GNSS measurement as external aiding.

Since the processing is centralized the GNSS/INS filter must account for the GNSS states too (Godha 2006), hence the LC GNSS/INS filter state vector should be augmented with the receiver clock states.

The 15 parameters state vector in the LC architecture becomes:

a 17 parameters state vector in GPS-only case

$$\underline{\delta x}=\left[\underline{\delta r}^n \quad \underline{\delta v}^n \quad \underline{\varepsilon}^n \quad \underline{\delta b}_a \quad \underline{\delta b}_g \quad \delta\left(c\delta t_{offset}\right) \quad \delta\left(c\delta t_{drift}\right)\right]^T$$

or

a 18 parameters state vector in GPS/GLONASS case

$$\underline{\delta x} = \left[\underline{\delta r}^n \quad \underline{\delta v}^n \quad \underline{\varepsilon}^n \quad \underline{\delta b}_a \quad \underline{\delta b}_g \quad \delta\left(c\delta t_{offset}\right) \quad \delta\left(c\delta t_{drift}\right) \quad \delta\left(c\delta t_{sys}\right) \right]^T .$$

Similarly the 21 parameters state vector becomes:

a 23 parameters state vector in GPS-only case

$$\underline{\delta x} = \left[\underline{\delta r}^n \quad \underline{\delta v}^n \quad \underline{\varepsilon}^n \quad \underline{\delta b}_a \quad \underline{\delta b}_g \quad \underline{\delta S}_a \quad \underline{\delta S}_g \quad \delta\left(c\delta t_{offset}\right) \quad \delta\left(c\delta t_{drift}\right) \right]^T$$

or

a 24 parameters state vector in GPS/GLONASS case

$$\underline{\delta x} = \left[\underline{\delta r}^n \quad \underline{\delta v}^n \quad \underline{\varepsilon}^n \quad \underline{\delta b}_a \quad \underline{\delta b}_g \quad \underline{\delta S}_a \quad \underline{\delta S}_g \quad \delta\left(c\delta t_{offset}\right) \quad \delta\left(c\delta t_{drift}\right) \quad \delta\left(c\delta t_{sys}\right) \right]^T .$$

Process Model

The receiver clock states dynamic equations can be written as (Brown and Hwang 1997):

$$\begin{aligned} \delta\left(c\dot{\delta t}_{offset}\right) &= \delta\left(c\delta t_{drift}\right) + \eta_{offset} \\ \delta\left(c\dot{\delta t}_{drift}\right) &= \eta_{drift} \end{aligned} \qquad (5\text{-}24)$$

where

η_{offset} is the clock offset driving noise with spectral density q_{offset} and

η_{drift} is the clock drift driving noise with spectral density q_{drift}.

The clock error spectral densities can be computed as (Brown and Hwang 1997):

$$q_{offset} = c^2 \cdot \frac{h_0}{2}$$

$$q_{drift} = c^2 \cdot 2\pi^2 \cdot h_{-2}$$

where h_0 and h_{-2} are Allan variance parameters describing the clock errors; typical values for compensated crystal clock can be $2.0e-19$ and $2.0e-20$ respectively (Brown and Hwang 1997).

The process model of the GNSS/INS KF in TC architecture with 23 states is obtained including equations (5-24) in the model (5-22):

$$\begin{bmatrix} \underline{\delta\dot{P}}^n \\ \underline{\delta\dot{v}}^n \\ \underline{\dot{\varepsilon}}^n \\ \underline{\delta\dot{b}}_a \\ \underline{\delta\dot{b}}_g \\ \underline{\delta\dot{S}}_a \\ \underline{\delta\dot{S}}_g \\ \delta(c\dot{\delta}t_{offset}) \\ \delta(c\dot{\delta}t_{drift}) \end{bmatrix} = \begin{bmatrix} F_{PP} & F_{Pv} & F_{P\varepsilon} & 0_3 & 0_3 & 0_3 & 0_3 & 0_{3x1} & 0_{3x1} \\ F_{vP} & F_{vv} & F_{v\varepsilon} & R_b^n & 0_3 & R_b^n \cdot F^b & 0_3 & 0_{3x1} & 0_{3x1} \\ F_{\varepsilon P} & F_{\varepsilon v} & F_{\varepsilon\varepsilon} & 0_3 & R_b^n & 0_3 & R_b^n \cdot W^b & 0_{3x1} & 0_{3x1} \\ 0_3 & 0_3 & 0_3 & \beta_{ba} & 0_3 & 0_3 & 0_3 & 0_{3x1} & 0_{3x1} \\ 0_3 & 0_3 & 0_3 & 0_3 & \beta_{bg} & 0_3 & 0_3 & 0_{3x1} & 0_{3x1} \\ 0_3 & 0_3 & 0_3 & 0_3 & 0_3 & \beta_{sa} & 0_3 & 0_{3x1} & 0_{3x1} \\ 0_3 & 0_3 & 0_3 & 0_3 & 0_3 & 0_3 & \beta_{sg} & 0_{3x1} & 0_{3x1} \\ 0_{1x3} & 0_{1x3} & 0_{1x3} & 0_{1x3} & 0_{1x3} & 0_{1x3} & 0_{1x3} & 0 & 1 \\ 0_{1x3} & 0_{1x3} & 0_{1x3} & 0_{1x3} & 0_{1x3} & 0_{1x3} & 0_{1x3} & 0 & 0 \end{bmatrix} \cdot \begin{bmatrix} \underline{\delta P}^n \\ \underline{\delta v}^n \\ \underline{\varepsilon}^n \\ \underline{\delta b}_a \\ \underline{\delta b}_g \\ \underline{\delta S}_a \\ \underline{\delta S}_g \\ \delta(c\delta t_{offset}) \\ \delta(c\delta t_{drift}) \end{bmatrix}$$

$$+ \begin{bmatrix} 0_3 & 0_3 & 0_3 & 0_3 & 0_3 & 0_3 & 0_{3x1} & 0_{3x1} \\ R_b^n & 0_3 & 0_3 & 0_3 & 0_3 & 0_3 & 0_{3x1} & 0_{3x1} \\ 0_3 & R_b^n & 0_3 & 0_3 & 0_3 & 0_3 & 0_{3x1} & 0_{3x1} \\ 0_3 & 0_3 & I_3 & 0_3 & 0_3 & 0_3 & 0_{3x1} & 0_{3x1} \\ 0_3 & 0_3 & 0_3 & I_3 & 0_3 & 0_3 & 0_{3x1} & 0_{3x1} \\ 0_3 & 0_3 & 0_3 & 0_3 & I_3 & 0_3 & 0_{3x1} & 0_{3x1} \\ 0_3 & 0_3 & 0_3 & 0_3 & 0_3 & I_3 & 0_{3x1} & 0_{3x1} \\ 0_{1x3} & 0_{1x3} & 0_{1x3} & 0_{1x3} & 0_{1x3} & 0_{1x3} & 1 & 0 \\ 0_{1x3} & 0_{1x3} & 0_{1x3} & 0_{1x3} & 0_{1x3} & 0_{1x3} & 0 & 1 \end{bmatrix} \cdot \begin{bmatrix} \underline{\eta}_a \\ \underline{\eta}_g \\ \underline{\eta}_{ba} \\ \underline{\eta}_{bg} \\ \underline{\eta}_{sa} \\ \underline{\eta}_{sg} \\ \eta_{offset} \\ \eta_{drift} \end{bmatrix} \qquad (5\text{-}25)$$

Similarly is obtained the process model with 17 states.

The time difference between GPS and GLONASS systems is very stable (Cai and Gao 2009) and so it can be modeled as random constant process, whose equation is:

$$\delta\left(c\dot{\delta}t_{sys}\right) = 0 \qquad (5\text{-}26)$$

The 24 states process model is obtained simply adding the equation (5-26) in the model (5-25):

$$
\begin{bmatrix} \underline{\delta\dot{P}}^n \\ \underline{\delta\dot{v}}^n \\ \underline{\dot{\varepsilon}}^n \\ \underline{\delta\dot{b}}_a \\ \underline{\delta\dot{b}}_g \\ \underline{\delta\dot{S}}_a \\ \underline{\delta\dot{S}}_g \\ \delta(c\dot{\delta}t_{offset}) \\ \delta(c\dot{\delta}t_{drift}) \\ \delta(c\dot{\delta}t_{sys}) \end{bmatrix} =
\begin{bmatrix}
F_{PP} & F_{Pv} & F_{P\varepsilon} & 0_3 & 0_3 & 0_3 & 0_3 & 0_{3x1} & 0_{3x1} & 0_{3x1} \\
F_{vP} & F_{vv} & F_{v\varepsilon} & R_b^n & 0_3 & R_b^n \cdot F^b & 0_3 & 0_{3x1} & 0_{3x1} & 0_{3x1} \\
F_{\varepsilon P} & F_{\varepsilon v} & F_{\varepsilon\varepsilon} & 0_3 & R_b^n & 0_3 & R_b^n \cdot W^b & 0_{3x1} & 0_{3x1} & 0_{3x1} \\
0_3 & 0_3 & 0_3 & \beta_{ba} & 0_3 & 0_3 & 0_3 & 0_{3x1} & 0_{3x1} & 0_{3x1} \\
0_3 & 0_3 & 0_3 & 0_3 & \beta_{bg} & 0_3 & 0_3 & 0_{3x1} & 0_{3x1} & 0_{3x1} \\
0_3 & 0_3 & 0_3 & 0_3 & 0_3 & \beta_{sa} & 0_3 & 0_{3x1} & 0_{3x1} & 0_{3x1} \\
0_3 & 0_3 & 0_3 & 0_3 & 0_3 & 0_3 & \beta_{sg} & 0_{3x1} & 0_{3x1} & 0_{3x1} \\
0_{1x3} & 0_{1x3} & 0_{1x3} & 0_{1x3} & 0_{1x3} & 0_{1x3} & 0_{1x3} & 0 & 1 & 0 \\
0_{1x3} & 0_{1x3} & 0_{1x3} & 0_{1x3} & 0_{1x3} & 0_{1x3} & 0_{1x3} & 0 & 0 & 0 \\
0_{1x3} & 0_{1x3} & 0_{1x3} & 0_{1x3} & 0_{1x3} & 0_{1x3} & 0_{1x3} & 0 & 0 & 0
\end{bmatrix} \cdot
\begin{bmatrix} \underline{\delta P}^n \\ \underline{\delta v}^n \\ \underline{\varepsilon}^n \\ \underline{\delta b}_a \\ \underline{\delta b}_g \\ \underline{\delta S}_a \\ \underline{\delta S}_g \\ \delta(c\delta t_{offset}) \\ \delta(c\delta t_{drift}) \\ \delta(c\delta t_{sys}) \end{bmatrix}
$$

$$
+\begin{bmatrix}
0_3 & 0_3 & 0_3 & 0_3 & 0_3 & 0_3 & 0_{3x1} & 0_{3x1} \\
R_b^n & 0_3 & 0_3 & 0_3 & 0_3 & 0_3 & 0_{3x1} & 0_{3x1} \\
0_3 & R_b^n & 0_3 & 0_3 & 0_3 & 0_3 & 0_{3x1} & 0_{3x1} \\
0_3 & 0_3 & I_3 & 0_3 & 0_3 & 0_3 & 0_{3x1} & 0_{3x1} \\
0_3 & 0_3 & 0_3 & I_3 & 0_3 & 0_3 & 0_{3x1} & 0_{3x1} \\
0_3 & 0_3 & 0_3 & 0_3 & I_3 & 0_3 & 0_{3x1} & 0_{3x1} \\
0_3 & 0_3 & 0_3 & 0_3 & 0_3 & I_3 & 0_{3x1} & 0_{3x1} \\
0_{1x3} & 0_{1x3} & 0_{1x3} & 0_{1x3} & 0_{1x3} & 0_{1x3} & 1 & 0 \\
0_{1x3} & 0_{1x3} & 0_{1x3} & 0_{1x3} & 0_{1x3} & 0_{1x3} & 0 & 1
\end{bmatrix} \cdot
\begin{bmatrix} \underline{\eta}_a \\ \underline{\eta}_g \\ \underline{\eta}_{ba} \\ \underline{\eta}_{bg} \\ \underline{\eta}_{sa} \\ \underline{\eta}_{sg} \\ \eta_{offset} \\ \eta_{drift} \end{bmatrix} \qquad (5\text{-}27)
$$

Measurement Model

In tightly coupled approach the measurement model of the GNSS/INS filter is the same as the measurement model of the GNSS LS estimator described in Chapter 4, i.e. equation (4-25) in GPS-only case and equation (4-30) in combined GPS/GLONASS case (the columns of the geometry matrix in correspondence of the states $\underline{\delta b}_a, \underline{\delta b}_g, \underline{\delta S}_a, \underline{\delta S}_g$ are filled with zeros).

The only difference is the linearization point, which is obtained from INS mechanization; the measurements are:

$$
\underline{\delta z} = \begin{bmatrix} PR - PR_{INS} \\ \cdots \\ P\dot{R} - P\dot{R}_{INS} \\ \cdots \end{bmatrix} \qquad (5\text{-}28)
$$

where

PR_{INS} is the predicted pseudorange using INS-derived information,

$\dot{PR}_{INS}$ is the predicted pseudorange derivative using INS-derived information.

As in the LC GNSS filter (5.3.1), the measurements are weighted according to their elevation and considering also the inherent accuracy related to the PR or Doppler observables (formula (5-3)).

5.5 External Heading Aiding

To improve the heading estimation an external heading aiding can be used; for instance measurements from magnetometers, gyrocompass or GPS can be adopted as external source (Shin 2001, Nayak 2000, Godha 2006). To incorporate external heading measurements into the measurement model of the GNSS/INS filter, an equation relating the heading errors with the system error states is required (Godha 2006). Such an error equation is derived starting from the expression of the azimuth as function of the elements of the rotation matrix $\hat{R}_b^n$ (third of equations (2-17)), written with the hats on the top to remark that the quantities are estimated:

$$\hat{\psi} = \arctan\left(\frac{\hat{R}_n^b(2,1)}{\hat{R}_n^b(2,2)}\right) = \arctan\left(\frac{\hat{R}_b^n(1,2)}{\hat{R}_b^n(2,2)}\right) \tag{5-29}$$

From equations (2-27) and the third of (2-16), equation (5-29) becomes:

$$\hat{\psi} = \arctan\left(\frac{\hat{R}_b^n(1,2)}{\hat{R}_b^n(2,2)}\right) = \arctan\left(\frac{R_b^n(1,2) + \varepsilon_U R_b^n(2,2) - \varepsilon_N R_b^n(3,2)}{-\varepsilon_U R_b^n(1,2) + R_b^n(2,2) + \varepsilon_E R_b^n(3,2)}\right) = \arctan\left(\frac{N_\Psi}{D_\Psi}\right) \tag{5-30}$$

where

N_Ψ and D_Ψ are the numerator and the denominator respectively of the $\arctan(\;)$ object.

The heading error equation can be expressed as:

$$\delta\hat{\psi} = \frac{\partial\hat{\psi}}{\partial\varepsilon_E}\delta\varepsilon_E + \frac{\partial\hat{\psi}}{\partial\varepsilon_N}\delta\varepsilon_N + \frac{\partial\hat{\psi}}{\partial\varepsilon_U}\delta\varepsilon_U \tag{5-31}$$

where

$$\frac{\partial\hat{\psi}}{\partial\varepsilon_E} = -\frac{\hat{R}_b^n(1,2)\,R_b^n(3,2)}{\left[\hat{R}_b^n(2,2)\right]^2 + \left[\hat{R}_b^n(1,2)\right]^2} \approx -\frac{\hat{R}_b^n(1,2)\,\hat{R}_b^n(3,2)}{\left[\hat{R}_b^n(2,2)\right]^2 + \left[\hat{R}_b^n(1,2)\right]^2},$$

$$\frac{\partial\hat{\psi}}{\partial\varepsilon_N} = -\frac{\hat{R}_b^n(2,2)R_b^n(3,2)}{\left[\hat{R}_b^n(2,2)\right]^2+\left[\hat{R}_b^n(1,2)\right]^2} \approx -\frac{\hat{R}_b^n(2,2)\hat{R}_b^n(3,2)}{\left[\hat{R}_b^n(2,2)\right]^2+\left[\hat{R}_b^n(1,2)\right]^2},$$

$$\frac{\partial\hat{\psi}}{\partial\varepsilon_U} = \frac{\hat{R}_b^n(1,2)R_b^n(1,2)+\hat{R}_b^n(2,2)R_b^n(2,2)}{\left[\hat{R}_b^n(2,2)\right]^2+\left[\hat{R}_b^n(1,2)\right]^2} \approx 1.$$

The values of $\frac{\partial\hat{\psi}}{\partial\varepsilon_E}$ and $\frac{\partial\hat{\psi}}{\partial\varepsilon_N}$ are very close to zero, and $\frac{\partial\hat{\psi}}{\partial\varepsilon_U}$ is approximately one, because an observation of azimuth is effectively an observation of ε_U directly.

The geometry matrix for the external heading aiding is:

$$H_\psi = \begin{bmatrix} 0_{1x3} & 0_{1x3} & \frac{\partial\hat{\psi}}{\partial\varepsilon_E} & \frac{\partial\hat{\psi}}{\partial\varepsilon_N} & \frac{\partial\hat{\psi}}{\partial\varepsilon_U} & 0_{1x(n-9)} \end{bmatrix} \tag{5-32}$$

The measurement vector is:

$$\delta\psi = \left[\psi_{INS} - \psi_{External}\right] \tag{5-33}$$

In this work the external heading aiding is obtained using horizontal components of the GPS-derived velocity and so the external azimuth source is (Shin 2005):

$$\psi_{External} = \arctan\left(\frac{V_E}{V_N}\right) \tag{5-34}$$

and the associated variance is (Godha 2006):

$$\sigma_\psi^2 = \frac{\sigma_{V_{GPS}}^2}{V_{H_{GPS}}^2} \tag{5-35}$$

where

$\sigma_{V_{GPS}}^2$ is the variance of the GPS-derived velocity and

$V_{H_{GPS}}^2$ is the horizontal GPS-derived velocity.

As it can be noticed in (5-35), the heading accuracy is inversely proportional to the horizontal velocity; for this reason, GPS heading is used only in case of sufficient speed (more than 5 m/s) (Godha 2006).

5.6 Motion Constraints

In absence of GNSS measurements, the INS performance degrades rapidly according to its grade. Moreover, navigation in scenarios such as urban canyons is characterized by long periods of lack of observable satellites. In these conditions the performance degradation with MEMS sensors is particularly severe owing to their large errors and noise levels (Godha 2006).

In vehicular navigation a possible approach to avoid the INS error accumulation is to derive observations from the motion of the vehicle, i.e. it is possible to generate constraint equations reflecting the behavior of the vehicle during navigation (Shin 2001, Sukkarieh 2000).

A first set of constraint equations can be derived considering that a vehicle essentially moves in the forward direction. A second constraint equation can be generated considering the fact that the height does not change significantly in land navigation during short time periods. Further details about the considered constraint equations are provided in the following sections.

5.6.1 Velocity Constraints

During typical vehicular navigation it can be assumed that the vehicle does not slip sideways or jump/bounce and so the motion is essentially in the forward direction. Recalling the definition of the body frame (Figure 2-2), these assumptions about the velocity can be described mathematically by the equations:

$$\begin{gathered} v_x^b \approx 0 \\ v_z^b \approx 0 \end{gathered} \tag{5-36}$$

where

v_x^b and v_z^b are components of the vehicle velocity perpendicular to the forward direction (expressed in the body frame).

To better represent the uncertainty in the considered assumptions, the equations (5-36) can be rearranged as:

$$\begin{aligned} v_x^b &= \eta_x \\ v_z^b &= \eta_z \end{aligned} \tag{5-37}$$

where

η_x and η_z are the (fictitious) measurement noises denoting the possible discrepancies in the above stated assumptions.

To be used in the KF context, the velocity constraint equations must be expressed in the measurement model form (3-13). The measurement vector can thus be defined as:

$$\underline{z} = \begin{bmatrix} \delta v_x^b \\ \delta v_z^b \end{bmatrix} = \begin{bmatrix} v_x^b - v_{INSx}^b \\ v_z^b - v_{INSz}^b \end{bmatrix} = \begin{bmatrix} 0 - v_{INSx}^b \\ 0 - v_{INSz}^b \end{bmatrix} \tag{5-38}$$

where

v_{INSx}^b and v_{INSz}^b are the INS velocity components.

In literature the standard deviation of the associated measurement noise $\sigma_{Vconstr}$ is assumed to be equal to the projection of the forward velocity v_y^b in the lateral and up directions, because of the misalignment angle θ (Godha 2006, Shin 2001):

$$\sigma_{Vconstr} = v_y^b \cdot \sin\theta$$

In this research a different approach is carried out and a fixed value for the standard deviation is used, avoiding to relate the constraint uncertainty with the estimation of the velocity.

Moreover the velocity constraint equations are adopted typically in vehicular navigation (Sukkarieh 2000); in this research the motion constrain equations are applied in pedestrian navigation context too, to assess the performance in this application; to adapt this aiding to the pedestrian case, the constraint uncertainty is increased with respect to the vehicular case.

The standard deviation of the measurement noise in the vehicular application is empirically set to 0.5 m/s, while in the pedestrian application is set to 1 m/s.

In order to relate the measurement vector (5-38) to the state vector, the relationship between the velocity vector in the body and the ENU frames is perturbed:

$$\begin{aligned}&\underline{V}^b = R_n^b \underline{V}^n = \left(R_b^n\right)^T \underline{V}^n = \\ &= \underline{\hat{V}}^b + \delta\underline{V}^b = \left[\left(I + E^n\right)\hat{R}_b^n\right]^T \left(\underline{\hat{V}}^n + \delta\underline{V}^n\right) = \\ &= \left[\hat{R}_n^b\left(I - E^n\right)\right]\left(\underline{\hat{V}}^n + \delta\underline{V}^n\right)\end{aligned} \tag{5-39}$$

and only the first order terms are collected:

$$\delta\underline{V}^b = \hat{R}_n^b \delta\underline{V}^n + \hat{R}_n^b \underline{\hat{V}}^n \times \underline{\varepsilon}^n \tag{5-40}$$

From the first and the last rows of equation (5-40) the design matrix is obtained:

$$H = \begin{bmatrix} 0_{1x3} & \hat{R}_{11} & \hat{R}_{12} & \hat{R}_{13} & \hat{R}_{12}\hat{V}_U - \hat{R}_{13}\hat{V}_N & \hat{R}_{13}\hat{V}_E - \hat{R}_{11}\hat{V}_U & \hat{R}_{11}\hat{V}_N - \hat{R}_{12}\hat{V}_E & 0_{1x(n-9)} \\ 0_{1x3} & \hat{R}_{31} & \hat{R}_{32} & \hat{R}_{33} & \hat{R}_{32}\hat{V}_U - \hat{R}_{33}\hat{V}_N & \hat{R}_{33}\hat{V}_E - \hat{R}_{31}\hat{V}_U & \hat{R}_{31}\hat{V}_N - \hat{R}_{32}\hat{V}_E & 0_{1x(n-9)} \end{bmatrix} \tag{5-41}$$

where

$\hat{R}_{ij}$ is the element (i,j) of the matrix $\hat{R}_n^b$.

The velocity constraint equations can be used when no GNSS measurements are available; in that case a complementary Kalman filter is implemented to merge inertial and constraint-derived information to prevent INS error unlimited growth. The scheme of the filter is shown in the Figure 5-3.

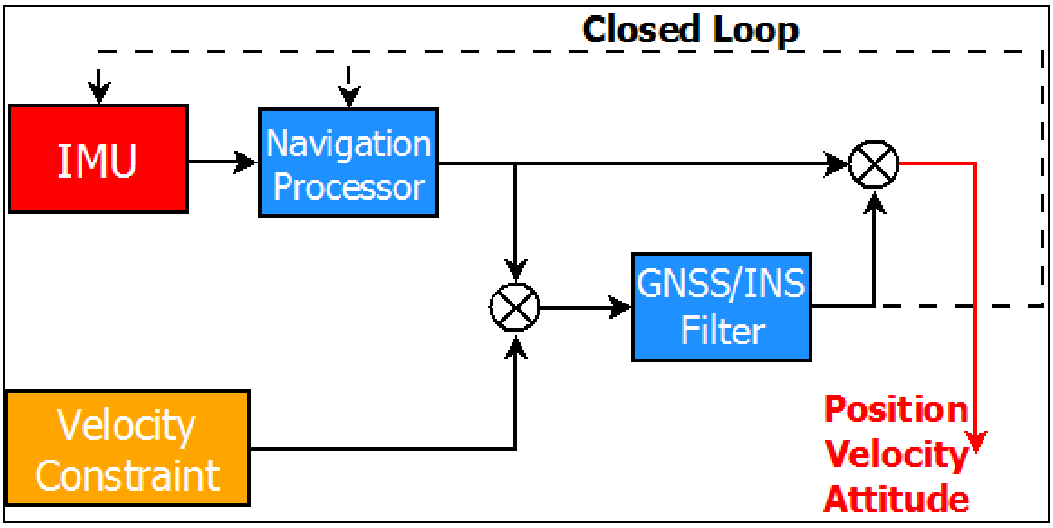

Figure 5-3 – Velocity Constraint Kalman Filter

5.6.2 Height Constraint

During a typical session of land navigation, the vehicle stays on the road and the height usually varies only few meters in a small region. So in case of lack of GNSS measurements the height of the vehicle can be considered equal to a predefined value (defined according to the topography of the territory) or to the last height estimation obtained in good measurement conditions (e.g. with a good DOP value).

This assumption can be used to implement an alternative Kalman filter in case of GNSS outage, whose measurement vector is defined as:

$$z = \left[h_{ref} - h_{INS} \right] \tag{5-42}$$

where

h_{ref} is the reference height and

h_{INS} is the INS-derived height.

The measurement noise standard deviation for these measurements depends on how the reference height is derived. If the height information is a predefined value, then the measurement uncertainty depends on the knowledge of the actual height variation for a particular region. If the height information is derived from a GNSS computation in good visibility condition, then the measurement standard deviation can be set to a relatively low value (few meters) for short GNSS outages.

The design matrix is:

$$H = \left[0 \quad 0 \quad 1 \quad 0_{1x(n-3)} \right] \tag{5-43}$$

The proposed measurement model is particularly simple to implement owing to the INS mechanization in the ENU frame. The scheme of the filter using the height constraint is showed in Figure 5-4.

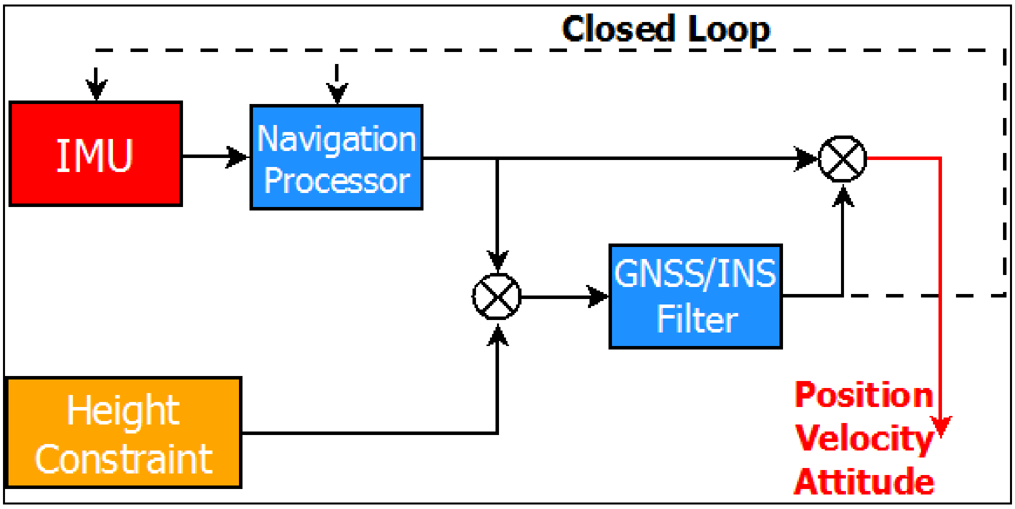

Figure 5-4 – Height Constraint Kalman Filter

The velocity and height constraints can be use alternatively as showed in the Figure 5-3 and Figure 5-4 or jointly during the GNSS outages; both constraint equations can also be used when GNSS measurements are available (Godha 2006).

Chapter 6 Test and Results

This chapter describes some tests carried out with details about the adopted equipment, the operational environment and the implemented algorithms. The considered scenarios are the pedestrian and the vehicular navigation in urban canyon context.

The GNSS only (single point positioning) results are presented to demonstrate the lack of continuity and accuracy of the solution in a signal degraded environment; then the navigation solution of an integrated system consisting of GNSS and INS MEMS-based sensors is shown, considering the configurations described in Chapter 4 and Chapter 5. The results obtained are compared with a reference solution achieved using an higher grade inertial sensor (specifically a tactical grade INS) and post-processing procedures.

6.1 Pedestrian Test

The term Pedestrian Navigation generally refers to navigation systems developed for a person on foot (Mezentsev 2005) and the MEMS sensors are suitable for pedestrian applications owing to their very small size and light weight (De Agostino 2010).

A common pedestrian configuration (called PDR Pedestrian Dead Reckoning) uses the accelerometer signals to detect the steps (as a “step counter”), the gyro signals to determine the heading and the GNSS measurements to estimate the step length and to calibrate PDR parameters (step length and heading) in order to improve the navigation during GNSS absence (Godha et al 2006, Groves 2008).

Another approach involves the use of conventional GNSS/INS algorithms, mitigating the large INS errors by placing the inertial unit on the foot to apply the ZUPT (Zero Velocity Updates) technique when the foot is at rest during the stance phase of the gait cycle (Bancroft et al 2008, Godha et al 2006).

In this research conventional GNSS/INS navigation algorithms are used and the equipment is placed in an aluminum box and is brought back by a pedestrian as shown in Figure 6-1. To bound the large INS MEMS errors, frequent GNSS (both GPS and GLONASS) updates are used (20 Hz) and the motion constraint equations, described in 5.6.1 and 5.6.2 and usually adopted in vehicular navigation, are applied (to be more suitable for pedestrian application, the constraint uncertainty is increased with respect to the vehicular application).

Figure 6-1 – Pedestrian Test Equipment

6.1.1 Equipment

The MEMS inertial unit used is a Crista IMU, produced by the US company Cloud Cap Technology Inc. The main characteristics of the IMU are in listed Table 2-2. The Crista IMU is a very small (2.05” x 1.55” x 1.00”) and light (36.8 grams) three axis inertial sensor, able to provide temperature compensated accelerometer and gyroscopic data. The measurement range is 300°/s and 10g for accelerometers and gyros respectively and the analog signals are sampled with a 16 bit A/D converter; the data are provided via serial interfaces. The Crista IMU has a built-in GPS pulse per second (PPS) interface which allows the accurate time synchronization of IMU and GPS data (Crista Interface/Operation Document 2004).

The receiver used is a NovAtel ProPak-V3 belonging to the OEMV family, and is a high-performance device able to provide L1 and L2 GPS+GLONASS positioning; the connected antenna is a high performance NovAtel 702 antenna.

The Crista IMU and the NovAtel ProPak-V3 are the devices used to test the proposed algorithms for the GNSS/INS integrated system.

A low cost GNSS/INS integrated system should include both a low cost IMU and a low cost receiver; in this research a high grade receiver is used and so the results are expected to be optimistic with respect to a completely low cost integrated system (which will be the object of future work).

The device used for generating a reference solution for error analysis is the NovAtel SPAN (Synchronous Position, Attitude and Navigation) system, consisting of a Honeywell HG1700 IMU and an OEM4 GPS receiver. The HG1700 IMU is a tactical grade inertial sensor providing low noise angular and acceleration data whose main characteristics are in listed Table 2-2; the inertial data are time tagged internally by the OEM4 receiver. Both the NovAtel ProPak-V3 and OEM4 receiver are connected to the same antenna through a signal splitter. The reference solution is computed in post-mission, processing the inertial and the GPS data with the NovAtel Inertial Explorer software using the tightly coupled strategy and the double difference technique; the GPS base station for differential processing is equipped with a dual-frequency NovAtel OEM4 receiver connected to a high performance NovAtel 702 antenna, placed on the roof top of a building 6-7 km away from the test location. The reference solution accuracy in these conditions (as estimated by the NovAtel software) is summarized in Table 6-1.

Table 6-1 – Reference Solution Accuracy

Reference Accuracy	
<u>Position</u>	dm level
<u>Velocity</u>	cm/s level
<u>Attitude</u>	<1deg

The collected data are stored in a laptop; all the described devices and the batteries necessary to power them are placed in an aluminum backpack (Figure 6-1).

6.1.2 Test Description

The pedestrian test was conducted on May 14 2010 in early morning in downtown Calgary (Canada), which is characterized by tall buildings, blocking GNSS signals and creating multipath condition, and so is an example of urban canyon.

Data collection begins in a parking lot with a static period of about 4 minutes (the aluminum box is placed on the ground) and good visibility condition (10 GPS and 6 GLONASS satellites available).

Then the walking test continues among the downtown blocks for about half an hour, following the trajectory shown in Figure 6-2.

First a small loop of about 600 meters, including one block, is covered in about 10 minutes; afterward a loop of about 1 km, including two blocks is covered in 20 minutes, with a static period of two minutes in a relatively open area in between (in a small parking lot). The data collection is concluded in the starting point.

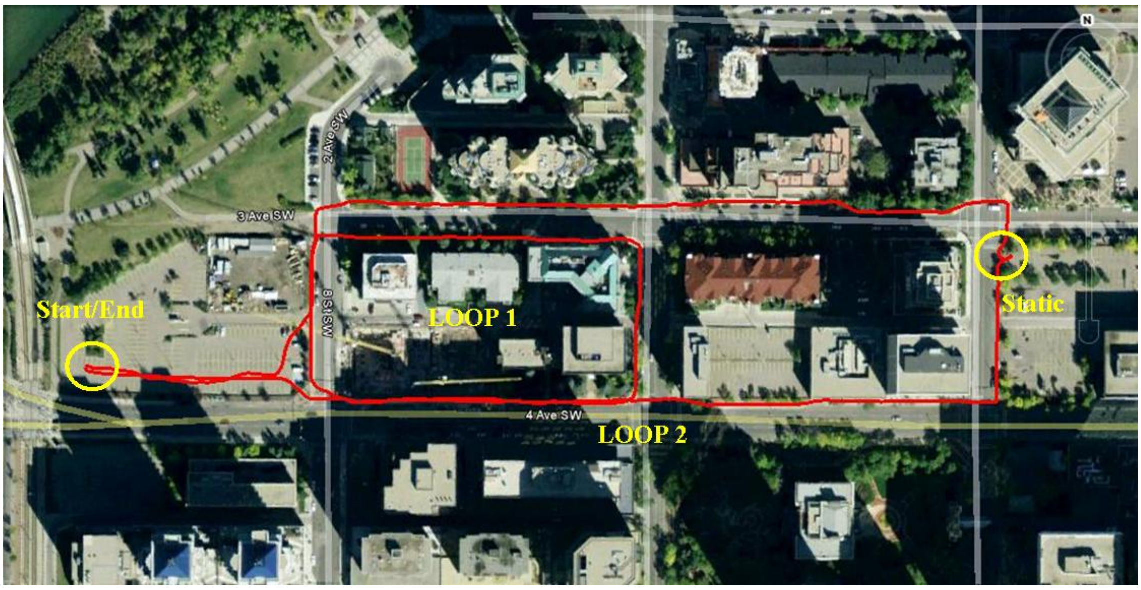

Figure 6-2 – Pedestrian Test Trajectory

6.1.3 GNSS Solution

In this section the results of the GNSS only positioning are presented and compared with the reference solution. A single point positioning is obtained by processing pseudorange and Doppler observables epoch by epoch. Specifically the WLS algorithm described in Chapter 4 is used.

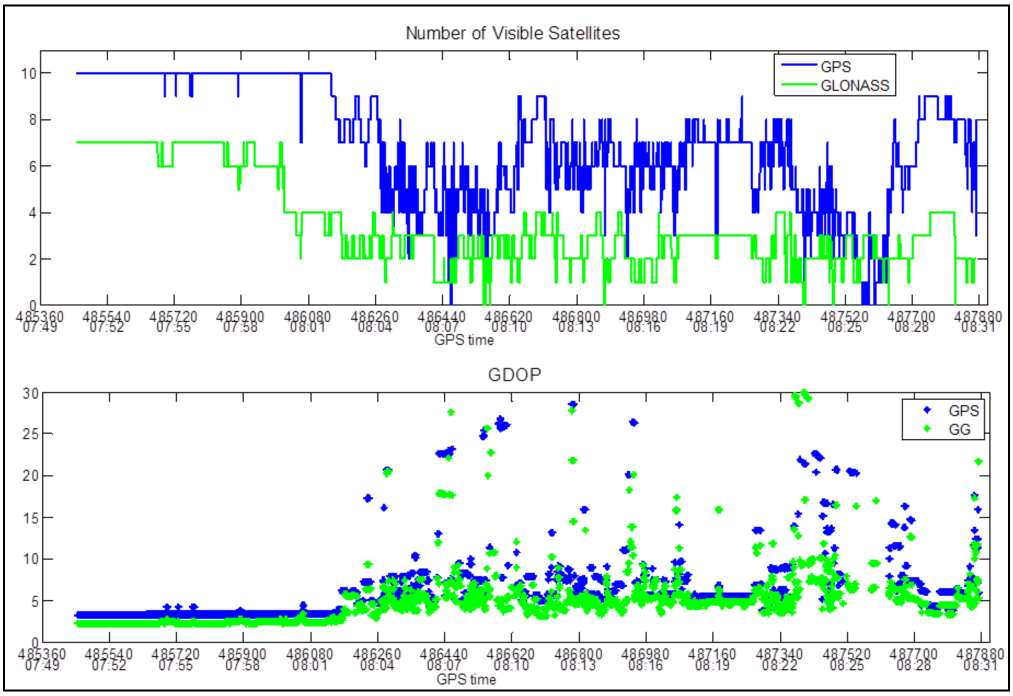

Figure 6-3 – Pedestrian Test: Visibility and GDOP

In Figure 6-3 the number of visible GPS and GLONASS satellites and the corresponding GDOP values for GPS only and GPS/GLONASS combined constellation (indicated with GG) are shown. At the beginning, the number of visible satellites is large and the GDOP value low as the receiver is in a relatively open area (the parking lot). Going inside the downtown area, the number of visible satellites decreases, varying between 8 and 0 for GPS and between 4 and 0 for GLONASS; the GDOP values increase noticeably, reaching peaks of more than 100 (not shown in the figure for clarity). In the GPS only case, the reduced visibility (less than 4 satellites) and the poor geometry make the environment very demanding for navigation. Including the GLONASS satellites yields great benefits in both visibility and geometry (indeed the GDOP values are always lower in GG case).

The benefit of including GLONASS can be seen in Figure 6-4 and Figure 6-5, showing the East, North and Up component errors in position and velocity respectively (the absolute values of the errors are plotted). The error, especially during the first minutes of the test, is nearly the same in both cases. The main benefit is in terms of solution continuity, as the GPS only solution is often unavailable for lack of satellites or bad geometry (solution with GDOP>30 are discarded) whereas the GG solution is more often available. To quantify this, the GPS only solution availability is about 82% and the GPS/GLONASS 90%.

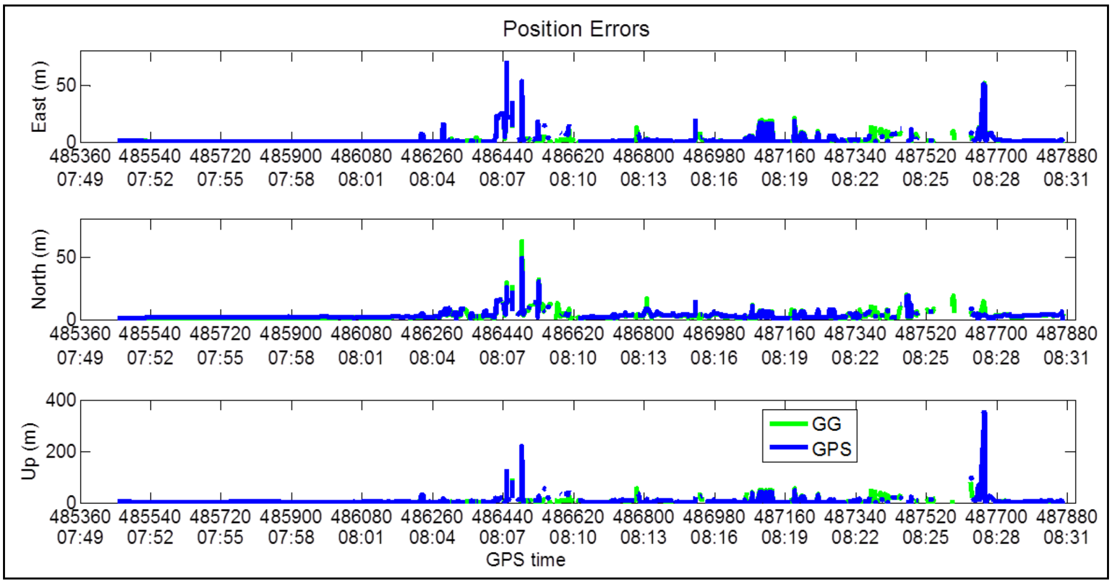

Figure 6-4 – Pedestrian Test: GNSS only Position Error

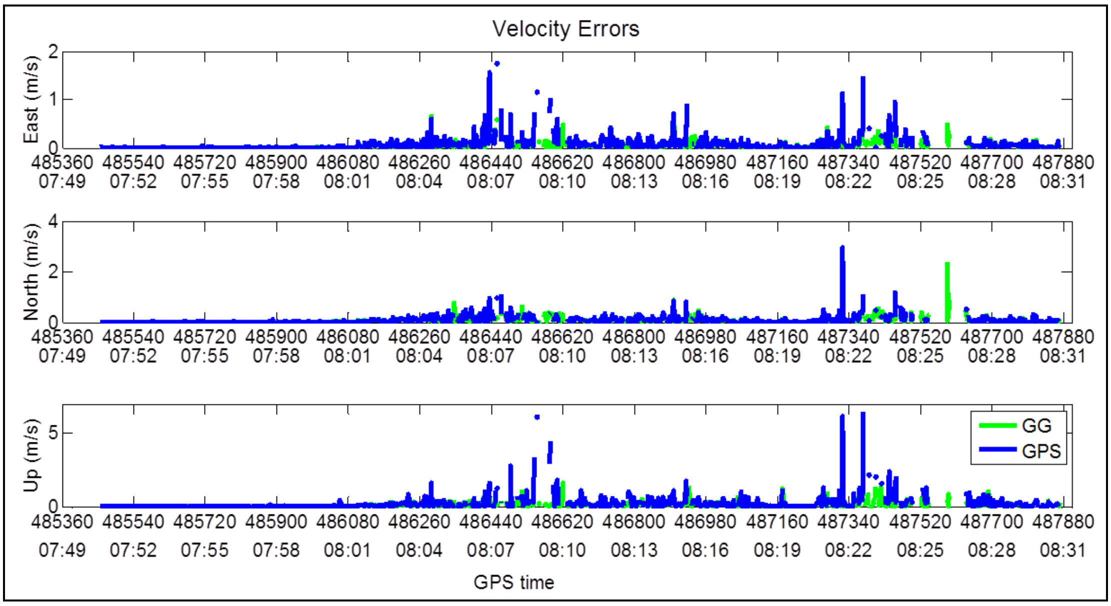

Figure 6-5 – Pedestrian Test: GNSS only Velocity Error

The Table 2-1 summarizes the accuracy of the solutions, showing the maximum and RMS position and velocity errors. It can be noted that the accuracies in the GPS only and GPS/GLONASS cases are quite similar. The GG solution shows a larger maximum error is the North direction (shown in the middle subplot of Figure 6-4 around 08:07), affecting the corresponding RMS component; a smaller maximum error is shown on the Up direction of the GG solution. The velocity obtained with GPS and GLONASS shows slightly better results on all the components.

Table 6-2 – Pedestrian Test: RMS and Maximum Errors of GPS and GPS/GLONASS

		RMS Error			***Maximum Error***		
		East	*North*	*Up*	*East*	*North*	*Up*
GPS	*Position (m)*	6,6	4,9	30,0	71,9	49,1	353,2
	Velocity (m/s)	0,2	0,2	0,6	1,8	3,0	6,4
GPS/ GLONASS	*Position (m)*	6,2	5,2	25,1	71,9	62,3	303,8
	Velocity (m/s)	0,1	0,2	0,4	1,4	2,4	6,2

The RAIM algorithm described in 3.2 is applied, performing the global test on the residuals (3-28), to check the self-consistency of the measurements and the local test to identify possible blunders.

The tested urban environment is often characterized by lack of redundancy necessary to identify possible blunders. Frequently during the test, it happens that 5-6 GPS satellites are available; although this number of satellites is sufficient to reject possible blunders and to compute solution, a more prudent approach is carried out wherein possible blunders are simply de-weighted

6.1.4 GNSS/INS Integrated Results

In this section the results of the GNSS/INS(MEMS) integration are presented and compared with the reference solution. The integrated system will provide a 100% solution availability as the navigation solution is bridged by INS prediction during GPS outages (Godha 2006). Hence the availability is not a meaningful indicator of system performance as in the GNSS only case, and the errors from the reference are more meaningful.

The loose and the tight integrations are treated separately. First the results obtained with LC strategy are shown, considering different configurations (e.g. with a 15 or 21-states filter, with or without GLONASS, with or without aiding). Afterwards a similar approach is followed for the TC strategy and finally the results obtained with LC and TC integrations are compared.

In each considered case the blunder detection strategy described in the previous section is carried out.

Results with Loosely Coupled Integration

Herein the results obtained with LC strategy are presented, considering and comparing different configurations; specifically the following cases are discussed:

- GPS/INS with a 15-state filter,
- GPS/INS with a 21-state filter,
- GG/INS with a 21-state filter,
- GG/INS with a 21-state filter and velocity constraints and
- GG/INS with a 21 state filter and velocity and height constraints.

In the first configuration the GPS only and INS measurements are integrated with the LC strategy using a 15-state filter (the configuration is indicated as LC GPS/INS 15). This configuration can be considered as a basic configuration. From the obtained trajectory, shown in Figure 6-6, it can be noted that the configuration is able to follow the reference trajectory for most of the time; this happens when the number of visible satellites is sufficient to perform a GPS fix, correcting the INS errors and not allowing errors to grow and is facilitated by the GPS high rate (20 Hz).

Great errors are only in the south zones of both Loops 1 and 2; these areas are critical because they are characterized by partial (1 to 3 satellites) or complete GPS outages (0 satellites).

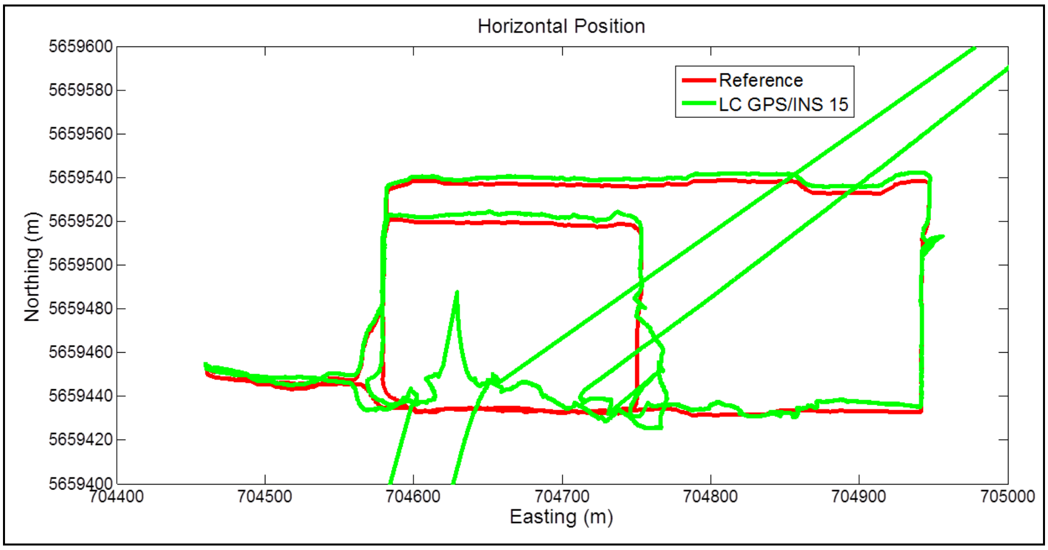

Figure 6-6 – Pedestrian Test: Trajectory of LC GPS/INS 15 Configuration

In Figure 6-7 the horizontal error (East and North error components) obtained with the LC GPS/INS 15 configuration and the “GPS Flag” parameter, indicating when the GPS fix is performed, are shown around the critical area. The Figure 6-7 clearly demonstrates that when the GPS fix is performed, the horizontal error is small, whereas the number of available satellites or the observation geometry do not allow to perform an accurate GPS fix for several seconds, the position errors tend to increase. It can be noticed that after 08:26 a GPS outage of about 45 seconds begins and the horizontal error increases to more than 600 meters until the outage is broken by a few fixes and the errors jump back to few meters.

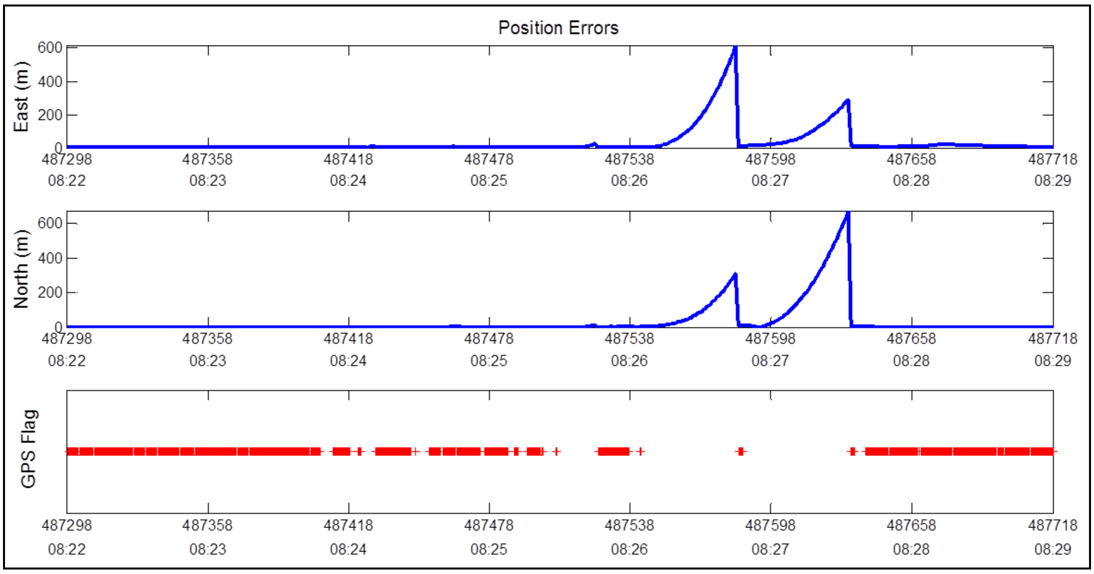

Figure 6-7 – Pedestrian Test: Horizontal Errors of LC GPS/INS 15 Configuration and GPS Availability

In Figure 6-8 the number of visible GPS satellites is plotted on the trajectory and the mentioned critical areas are circled.

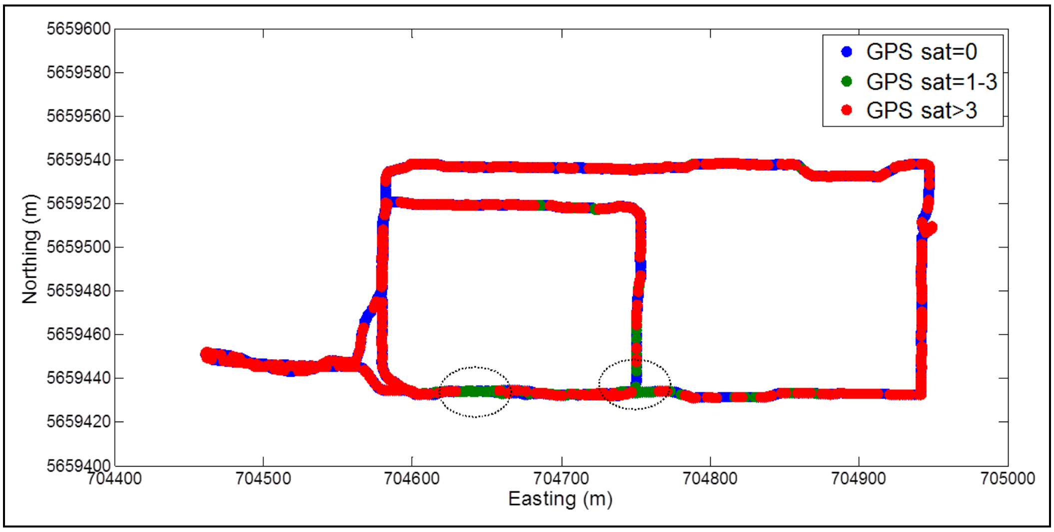

Figure 6-8 – Pedestrian Test: Number of Visible GPS Satellites on the Trajectory

A more complete overview of the obtained performance is provided by Table 6-3, showing the position and velocity maximum and RMS errors. The maximum position errors are of several hundred meters and occur during the above-defined critical areas.

Table 6-3 – Pedestrian Test: RMS and Maximum Errors of LC GPS/INS 15 Configuration

	RMS Error			***Maximum Error***		
	East	*North*	*Up*	*East*	*North*	*Up*
Position (m)	40,6	46,8	18,3	614,9	670,1	117,7
Velocity (m/s)	3,1	3,0	0,4	39,3	32,3	2,9

A typical approach to improve the integrated GPS/INS system performance during GPS outage is better model the INS errors to prevent error accumulation, for example including the sensor scale factors in the state vector. The trajectory obtained from the GPS/INS integration with a 21-state filter in LC architecture (indicated as LC GPS/INS 21) is shown in Figure 6-9. The position results in this case are similar to the previous case, especially in areas with good visibility. In the above-mentioned critical areas the system performance is enhanced (relative to the 15 state case) as indicated by the maximum position errors in Table 6-4.

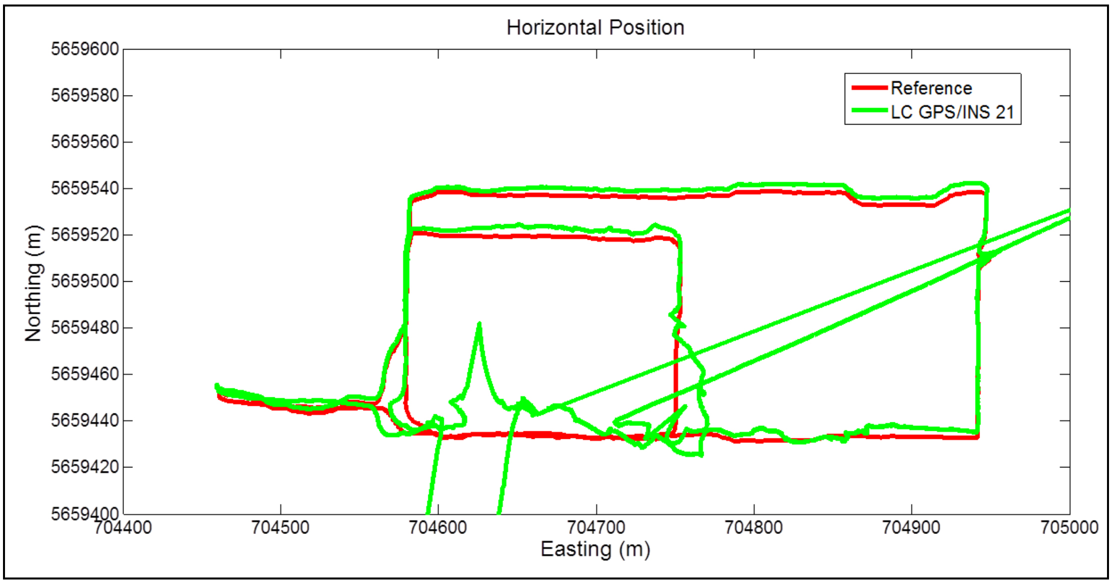

Figure 6-9 – Pedestrian Test: Trajectory of LC GPS/INS 21 Configuration

Table 6-4 – Pedestrian Test: RMS and Maximum Errors of LC GPS/INS 21 Configuration

	RMS Error			***Maximum Error***		
	East	*North*	*Up*	*East*	*North*	*Up*
Position (m)	24,4	27,0	15,9	395,6	388,7	120,9
Velocity (m/s)	1,8	1,6	0,4	24,7	17,1	2,1

The maximum horizontal position errors are almost halved and this performance can be attributed to a superior sensor error compensation with a 21-state filter; the maximum velocity errors are reduced significantly too.

Including the GLONASS satellites, the GNSS solution availability increases significantly as shown in section 6.1.3; the type of positioning according to the visible satellites is plotted on the trajectory in Figure 6-10, showing that the coverage in the above-mentioned critical areas is improved. The trajectory obtained from the GPS-GLONASS/INS integration with a 21-state filter in LC architecture (indicated as LC GG/INS 21) is presented in Figure 6-11 and shows a better agreement with the reference solution with respect to the other considered configurations.

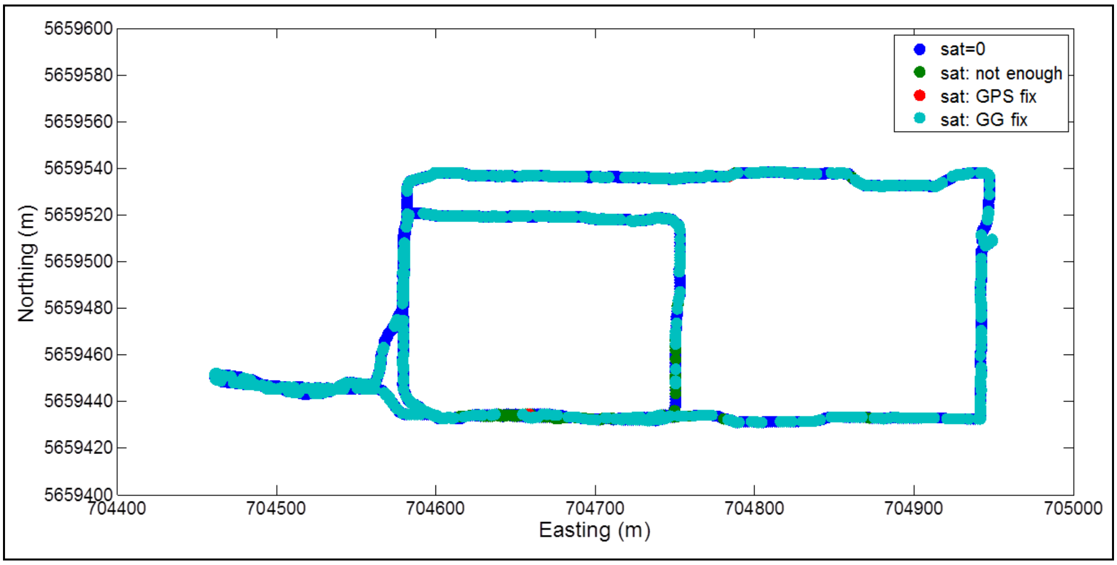

Figure 6-10 – Pedestrian Test: GPS/GLONASS Positioning on the Trajectory

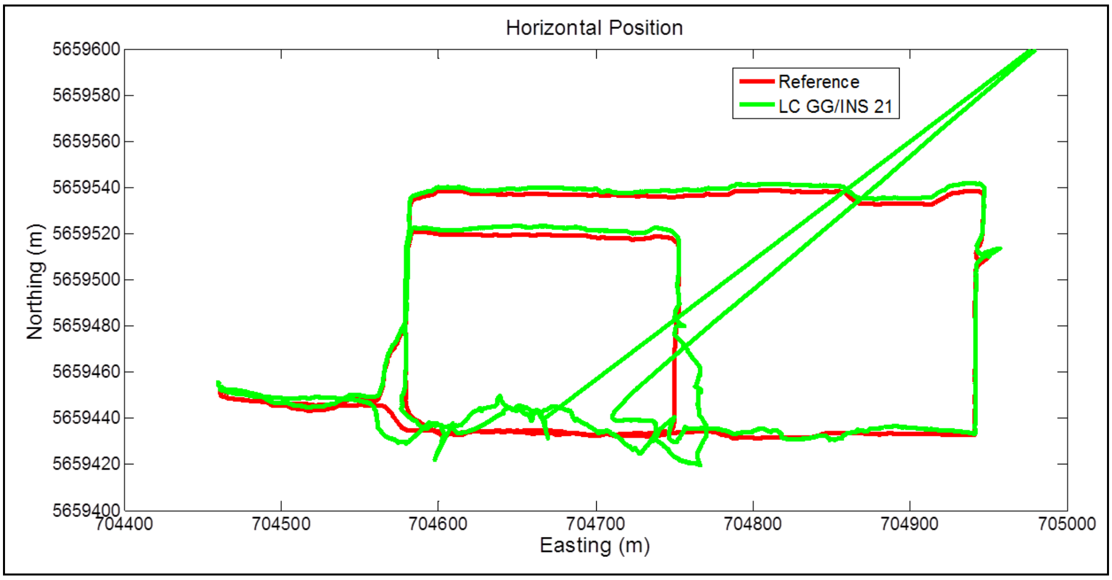

Figure 6-11 – Pedestrian Test: Trajectory of LC GG/INS 21 Configuration

The benefits of including GLONASS in the critical areas are evident in Table 6-5: the maximum horizontal errors are meaningfully reduced, affecting the RMS position errors too. Moreover both the RMS and maximum velocity errors benefit from the GPS/GLONASS combination.

Table 6-5 – Pedestrian Test: RMS and Maximum Errors of LC GG/INS 21 Configuration

	RMS Error			***Maximum Error***		
	East	*North*	*Up*	*East*	*North*	*Up*
Position (m)	19,9	11,1	12,3	333,2	178,1	110,6
Velocity (m/s)	1,5	0,8	0,2	21,1	10,5	1,5

Despite remarkable improvements obtained with LC GG/INS 21 configuration relative to LC GPS/INS 21 in terms of maximum and RMS position errors (Table 6-4 and Table 6-5), the trajectory in Figure 6-11 shows a large drift in the critical area. In Figure 6-12 the East and North error components obtained with the LC GG/INS 21 configuration and the “GNSS Flag” parameter, indicating when the GNSS fix is performed, are shown around the critical area; the errors during the GNSS outage just after 08:26 is reduced relative to GPS only case and the horizontal errors increase up to about 350 meters. The other long outage between 08:27 and 08:28 is reduced to about 30 seconds and is well bridged with the considered configuration.

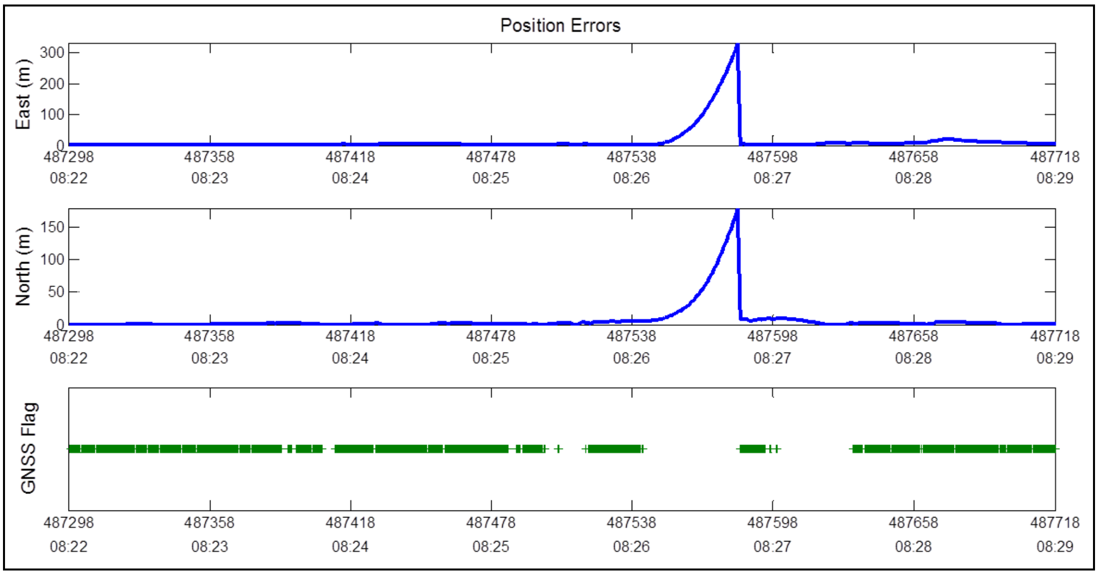

Figure 6-12 – Pedestrian Test: Horizontal Errors of LC GG/INS 21 Configuration and GNSS Availability

In the section 5.6 the use of motion constraints is introduced as a possible approach to reduce INS error accumulation during GNSS outages. In literature this specific approach is typically adopted in vehicular navigation (Godha 2006, Shin 2001, Sukkarieh 2000) as in this application the assumed motion constraint equations properly represent the actual motion.

In this research the motion constrain equations are applied in pedestrian navigation context too, to assess the performance in this application; to adopt this approach the constraint uncertainty is increased with respect to the vehicular case. The standard deviation of the measurement noise in the vehicular application is empirically set to 0.5 m/s, while in the pedestrian application is set to 1 m/s.

The results obtained from the GG/INS integration with a 21-state filter in LC architecture and with the aid of the velocity constraints (section 5.6.1) is presented below (indicated as LC GG/INS 21 V).

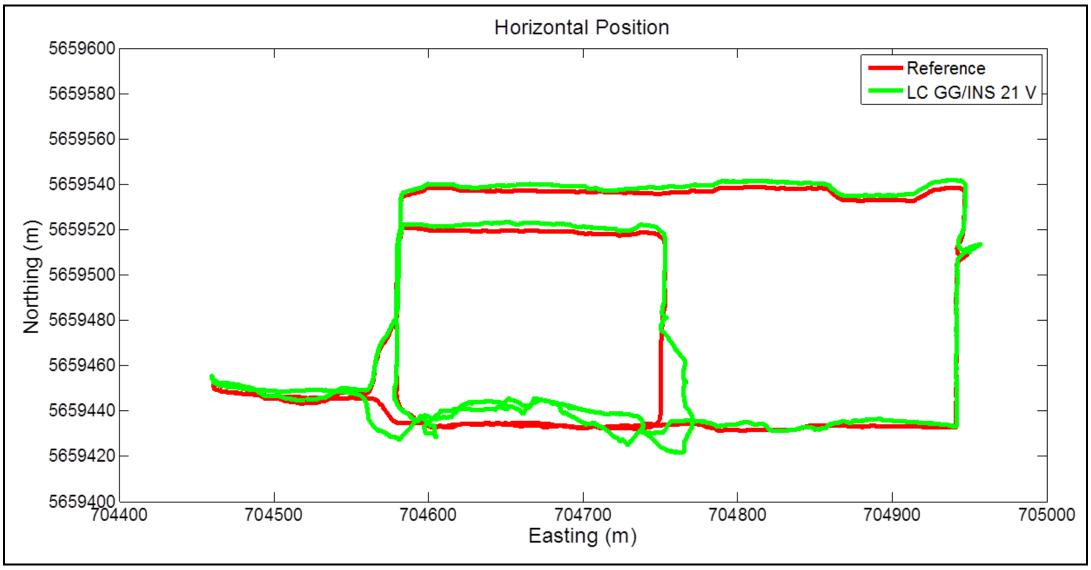

Figure 6-13 – Pedestrian Test: Trajectory of LC GG/INS 21 V Configuration

The trajectory obtained with the velocity constraints (Figure 6-13) shows remarkable improvements with respect to the other considered configurations; the large drift errors are no longer present as confirmed in Table 6-6, where the maximum horizontal errors are about 15-20 meters and the RMS errors only a few meters (one order of magnitude less than the other configurations). The velocity RMS and maximum errors are noticeably reduced too. The only critical parameters remains the altitude, whose maximum error is almost 100 meters, which is still less than the other cases by several meters.

Table 6-6 – Pedestrian Test: RMS and Maximum Errors of LC GG/INS 21 V Configuration

	RMS Error			***Maximum Error***		
	East	*North*	*Up*	*East*	*North*	*Up*
Position (m)	3,5	3,3	10,9	21,0	15,0	96,1
Velocity (m/s)	0,2	0,2	0,2	1,8	1,2	1,2

The results obtained with LC GG/INS 21 V (shown in Figure 6-13 and Table 6-6) demonstrate the effectiveness of the velocity constraints (properly adapted) in a particular pedestrian application too; however it must be pointed out that these results are obtained in a specific arrangement with the IMU fixed on a box, brought back by a pedestrian (which somehow acts as a vehicle). More tests are necessary to demonstrate a more general effectiveness of this method in the pedestrian context.

The final configuration with LC architecture includes the height constraint in addition to the velocity constraint (indicated as LC GG/INS 21 VH). The obtained solution is summarized in Table 6-7. The height reference information is derived from a GNSS computation in good visibility condition (i.e. with low DOP value) and the measurement standard deviation is set to a relatively low value (5 meters).

From the reference solution, the terrain has a range of altitude of few meters.

Table 6-7 – Pedestrian Test: RMS and Maximum Errors of LC GG/INS 21 VH Configuration

	RMS Error			***Maximum Error***		
	East	*North*	*Up*	*East*	*North*	*Up*
<u>Position</u> (m)	4,0	3,5	3,1	35,5	17,7	4,4
<u>Velocity</u> (m/s)	0,3	0,2	0,2	2,1	1,2	1,0

Including the height constraint equation (section 5.6.2) too, the horizontal position degrades slightly (maximum error about 10 meters and RMS error half meter), but in return, the maximum and RMS altitude errors are reduced to few meters.

A comparison between the altitude obtained using all the considered configurations so far is shown in Figure 6-14; it can be noted that each new component in the configuration yields a performance enhancement on the altitude too. The best altitude solution is obtained with the LC GG/INS 21 VH configuration, whose behavior is in agreement with the reference solution.

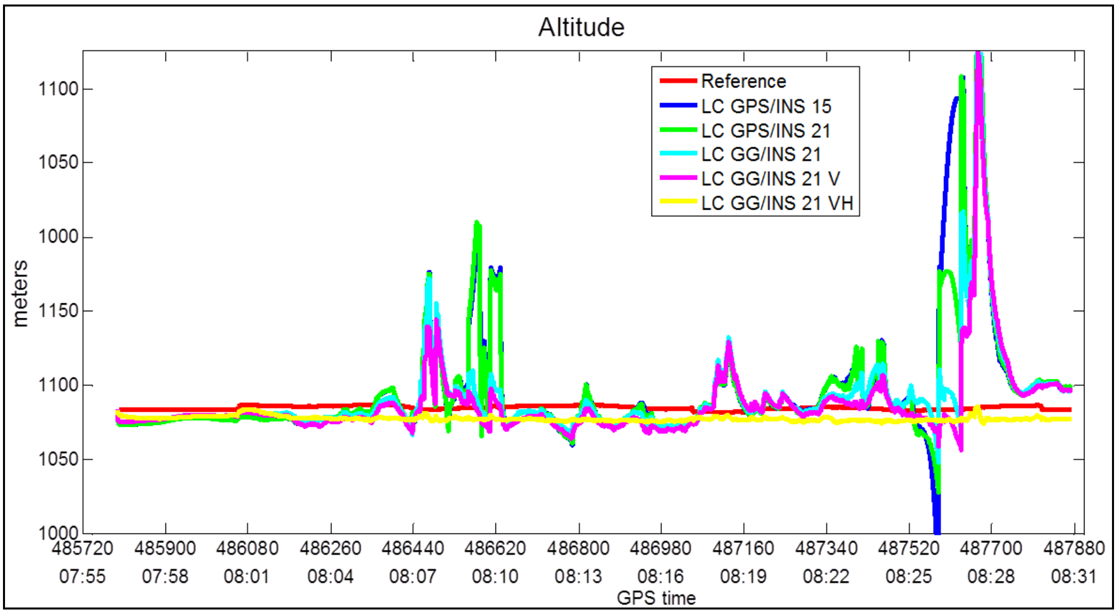

Figure 6-14 – Pedestrian Test: Altitude Comparison between LC Configurations

A comparison among the trajectories obtained from the considered implementations of the GNSS/INS integration in loosely coupled architecture are presented in Figure 6-15. The horizontal solution of the configurations including GPS only shows very large errors during the GPS outages, evidently reduced including the GLONASS measurements. The more accurate solutions are obtained including the velocity and height constraints, showing small disagreements with the reference in the critical area too. Between the two considered configurations with constraint aiding, i.e. LC GG/INS 21 V and LC GG/INS 21 VH, a slight better horizontal solution is obtained in the first case which shows a smaller disagreement in the South-West corner of the trajectory.

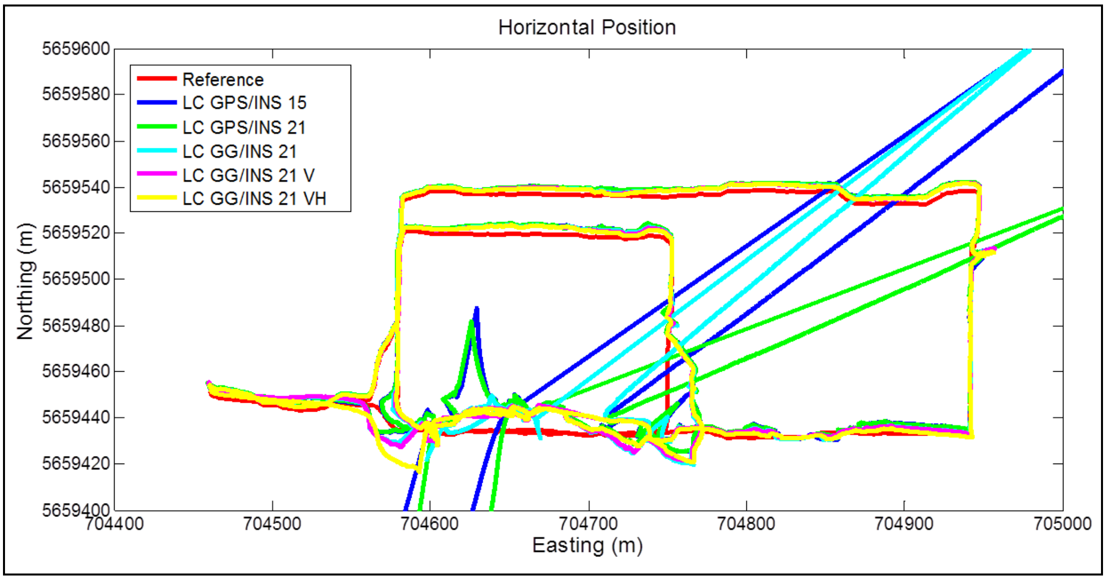

Figure 6-15 – Pedestrian Test: Trajectories obtained with the LC Architecture

To perform a concise comparison among the more meaningful configurations with LC architecture, the RMS errors of position and velocity are represented with a bar chart in Figure 6-16. Including GLONASS measurements, the improvements (relative to GPS only) in terms of all the considered parameters result evident. The configurations including the constraints show superior performances in terms of both position and velocity errors. The configurations including velocity constraints only and velocity/height constraints show similar errors in horizontal position, but the last shows better performance in altitude, influencing the 3D error too; the velocity errors are very similar for LC GG/INS 21 V and LC GG/INS 21 VH configurations.

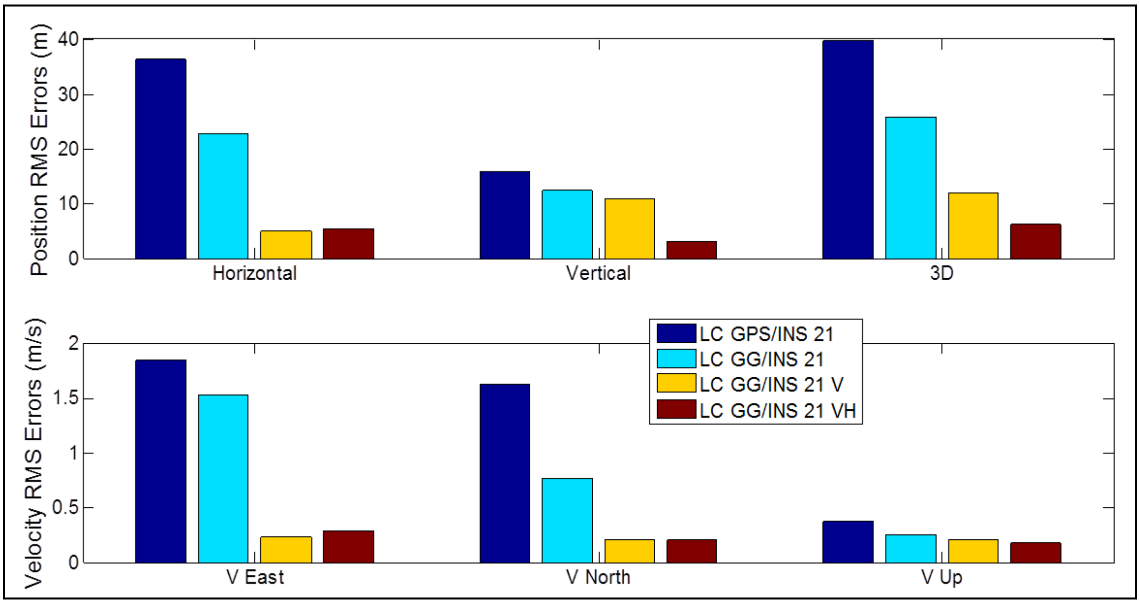

Figure 6-16 – Pedestrian Test: Comparison between LC Configurations in terms of Position and Velocity RMS Errors

Results with Tightly Coupled Integration

Now the results obtained with TC integration strategy are presented and compared with the just shown LC performance.

The basic TC configuration includes the integration of GPS only and INS with a 17-state filter (and is indicated as TC GPS/INS 17). The trajectory obtained in this configuration is shown in Figure 6-17. The solution is quite accurate during almost the whole test and degrades clearly in the critical areas described before because of the lack of GPS measurements; the maximum errors (Table 6-8) quantify the amount of the disagreement in the critical areas.

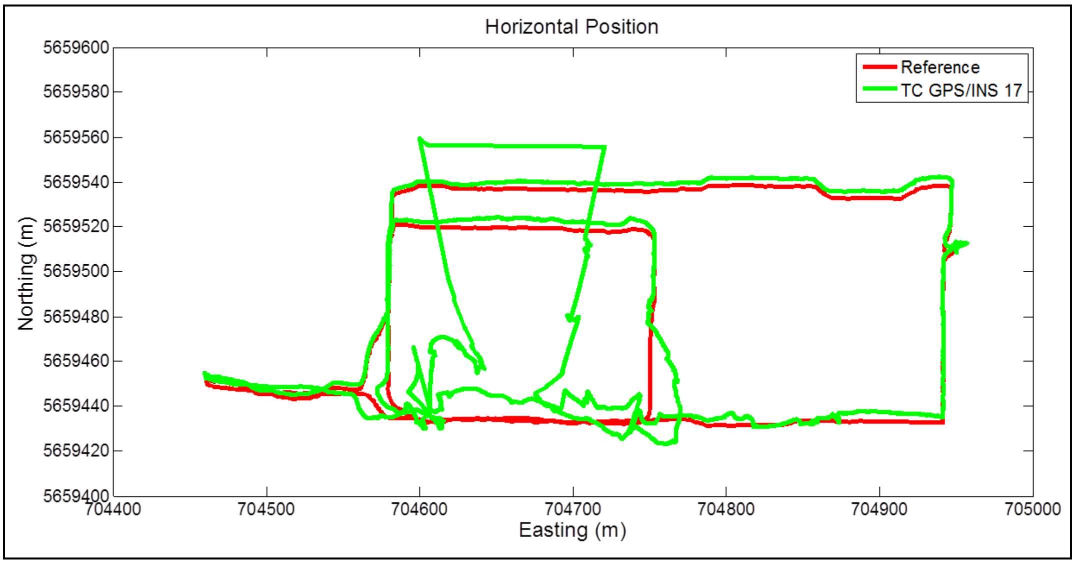

Figure 6-17 – Pedestrian Test: Trajectory of TC GPS/INS 17 Configuration

Table 6-8 – Pedestrian Test: RMS and Maximum Errors of TC GPS/INS 17 Configuration

	RMS Error			***Maximum Error***		
	East	*North*	*Up*	*East*	*North*	*Up*
Position (m)	6,2	8,0	24,4	51,4	116,3	143,1
Velocity (m/s)	0,4	0,7	0,5	4,5	9,4	4,1

A comparison of the two basic configurations for the loose and tight strategies, i.e. LC GPS/INS 15 and TC GPS/INS 17, is performed to assess the basic performance of the two architectures. Comparing Figure 6-6 and Figure 6-17 and Table 6-3 and Table 6-8, it can be noted that the TC integration results are characterized by much smaller maximum errors both in position and velocity because with a tightly strategy it is possible to compute an integrated solution during partial GPS outages. In contrast, the LC strategy can carry out an integrated solution only if the number of available satellites allows to perform a GPS only positioning (or in general GNSS positioning). The position error comparison between the two configurations is presented in Figure 6-18, where the better TC performance is evident. In the critical areas, around 08:09 and 08:27, the TC configuration is able to restrain the East error within 50 meters, whereas in the LC case the errors are much larger; the North error of TC configuration is larger than 100 meters, but much smaller than the LC case (around 08:26).

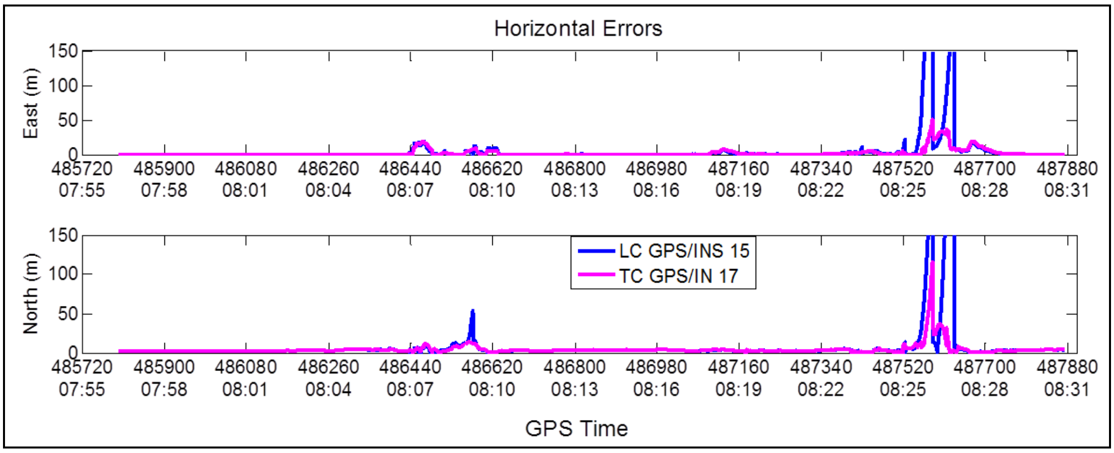

Figure 6-18 – Pedestrian Test: Horizontal Error Comparison between LC GPS/INS 15 and TC GPS/INS 17

The integration of GPS and INS in a TC strategy, including in the state vector the scale factors of the INS sensors, uses a 23-state filter and shows results very similar to the 17-state case. The TC GPS/INS 23 results are compared with LC GPS/INS 21 and LC

GG/INS 21 in terms of position and velocity RMS errors in the bar chart in Figure 6-19. The TC GPS/INS 23 configuration shows definitely smaller horizontal errors, but slightly larger altitude errors (relative to the two LC considered configurations). In can be noted that TC GPS/INS 23 and LC GG/INS 21 show similar 3D RMS errors, indicating comparable performances; this can suggest that including GLONASS satellites in LC architecture can change the role of loosely coupling in urban navigation (where usually the tight integration is preferred).

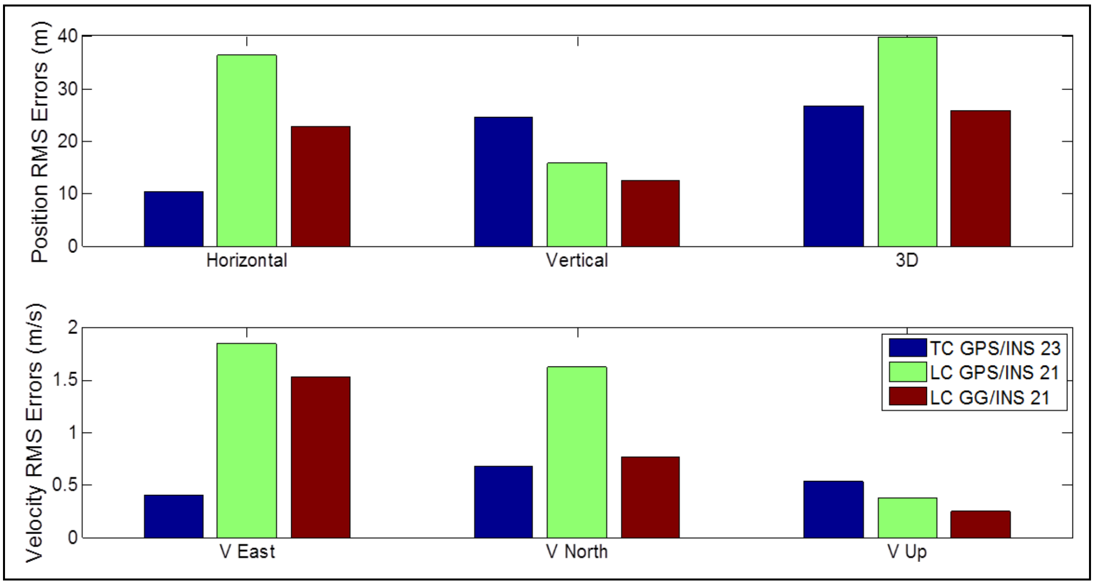

Figure 6-19 – Pedestrian Test: Comparison between TC GPS/INS 23, LC GPS/INS 21 and LC GG/INS 21 Configurations in terms of Position and Velocity RMS Errors

The results obtained including both GPS and GLONASS satellites in a TC integrated system GNSS/INS, adopting a 24-state filter (including the sensor scale factors) are now presented (the configuration is indicated as TC GG/INS 24). The obtained trajectory is shown in Figure 6-20 and exhibits an evident improvement in the position solution (relative to TC GPS/INS 17 and TC GPS/INS 23 cases), owing to the increased satellite availability. The position and velocity RMS and maximum errors are summarized in Table 6-9, showing few meters of RMS horizontal error and about 20 meters of maximum error; the maximum altitude error is large (about 100 meters).

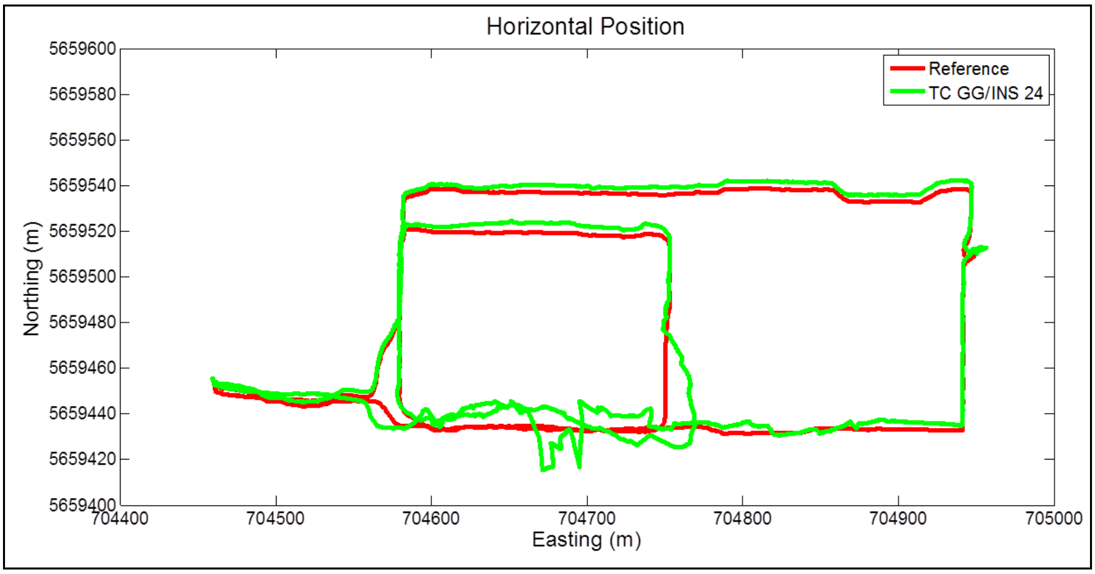

Figure 6-20 – Pedestrian Test: Trajectory of TC GG/INS 24 configuration

Table 6-9 – Pedestrian Test: RMS and Maximum Errors of TC GG/INS 24 Configuration

	RMS Error			***Maximum Error***		
	East	*North*	*Up*	*East*	*North*	*Up*
Position (m)	3,1	3,6	12,5	19,1	18,2	106,5
Velocity (m/s)	0,2	0,3	0,2	0,9	2,7	1,5

A comparison between the TC GG/INS 24 configuration and the corresponding loose coupling solution, i.e. the LC GG/INS 21 configuration, is carried out to emphasize the difference of performances of the two integration architectures in case of GLONASS inclusion. For this purpose the position errors are directly compared on the Figure 6-21, which clearly indicates the benefit of including GLONASS in this context too; only the altitude error remains large.

In Figure 6-21 the superior performance of the TC GG/INS 24 configuration relative to the corresponding loose case is demonstrated; a further comparison can be carried out with the loose integration cases including the motion constraints, i.e. LC GG/INS 21 V and LC GG/INS 21 VH to assess the effectiveness of loose approach in urban environment.

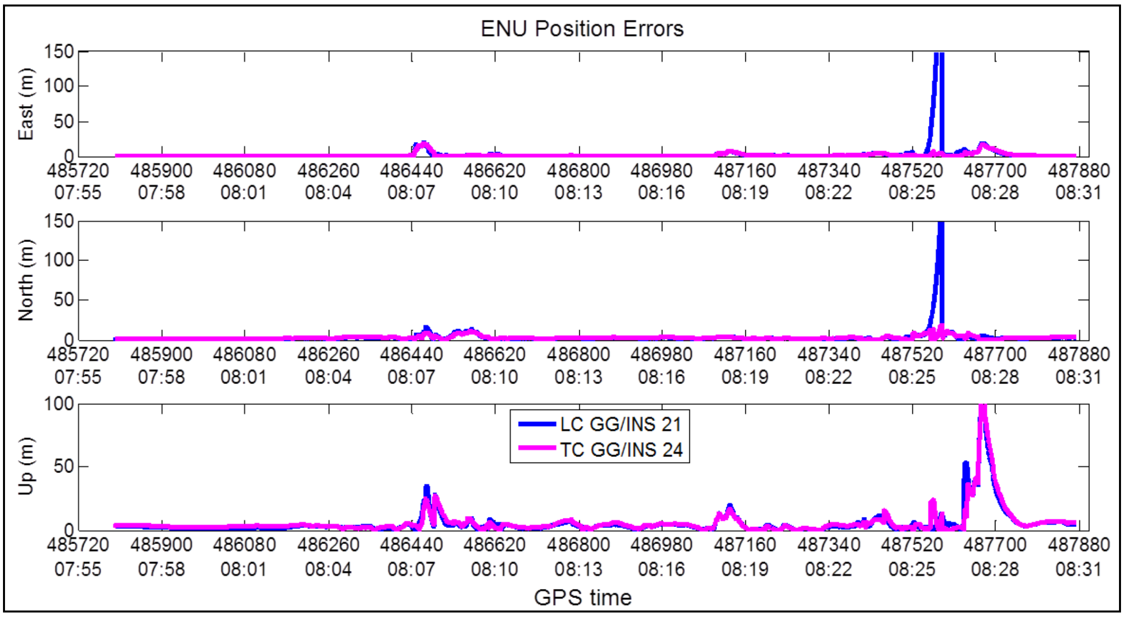

Figure 6-21 – Pedestrian Test: Position Error Comparison between LC GG/INS 21 and TC GG/INS 24 Configurations

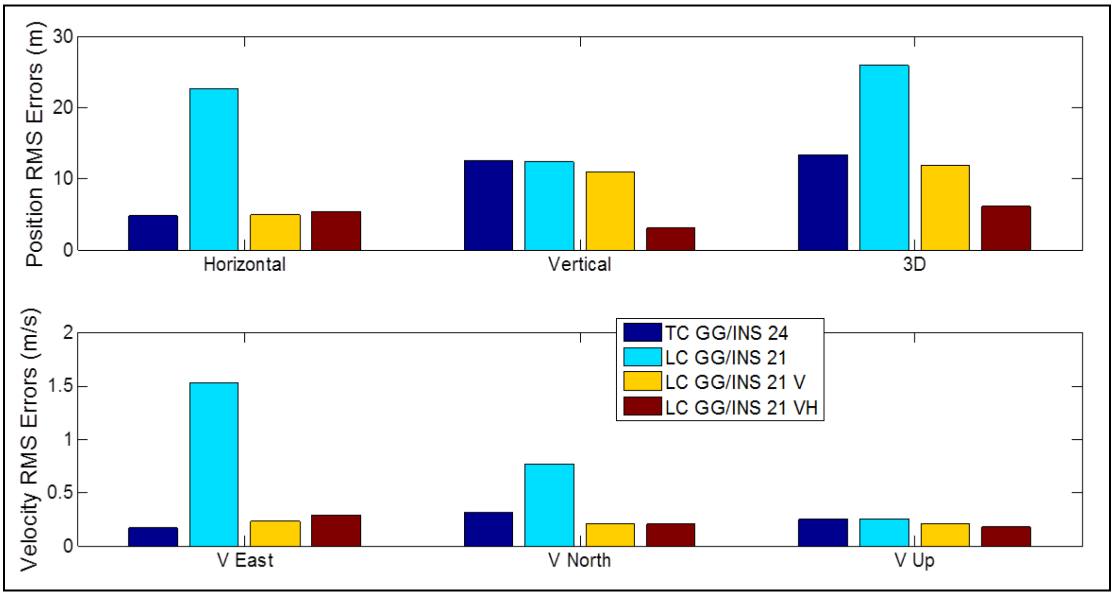

Figure 6-22 – Pedestrian Test: Comparison between TC GG/INS 24, LC GG/INS 21, LC GG/INS 21 V and LC GG/INS 21 VH Configurations in terms of Position and Velocity RMS Errors

In Figure 6-22 it is shown that adding velocity constraints to the LC GG/INS integration yields performance comparable with TC GG/INS case and adding height constraints too produces further improvements in terms of altitude and consequently of 3D RMS errors. This can make preferable to use LC architecture respect to TC, considering the modularity and flexibility of LC and that the motion constraints do not involve further cost, not involving actual sensors (Klein et al. 2010).

The final case is the integration of GPS-GLONASS and INS measurements in TC strategy with a 24-state filter and with the combined use of velocity and height motion constraints (indicated as TC GG/INS 24 VH); the obtained trajectory is shown in Figure 6-23 and the errors are summarized in Table 6-10. The use of the motion constraints further improve the performance of the integrated system, bringing the RMS errors to about 3 meters on horizontal position and 4.5 on altitude and RMS velocity errors to 0.2 m/s.

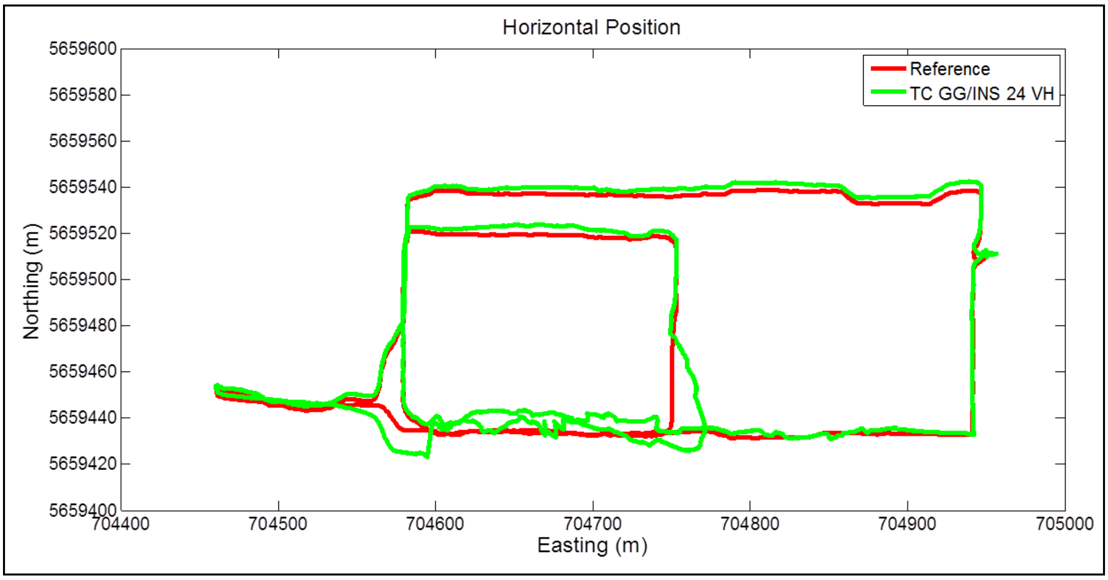

Figure 6-23 – Pedestrian Test: Trajectory of TC GG/INS 24 VH Configuration

Table 6-10 – Pedestrian Test: RMS and Maximum Errors of TC GG/INS 24 VH Configuration

	RMS Error			***Maximum Error***		
	East	*North*	*Up*	*East*	*North*	*Up*
Position (m)	2,5	3,2	4,5	21,1	11,4	6,6
Velocity (m/s)	0,2	0,2	0,2	0,9	1,3	1,1

To conclude this section a comparison is carried out between the best configurations obtained with LC and TC approaches, i.e. LC GG/INS 21 and TC GG/INS 24 both with velocity and height constraint aiding.

A position error comparison is carried out in Figure 6-24, showing a slightly better result for the TC approach on the East and North components and a slight advantage for the LC approach on the Up component.

A velocity error comparison is carried out in Figure 6-25, showing a quite similar error behavior of all the three components with only lower spikes in the East component of the TC case.

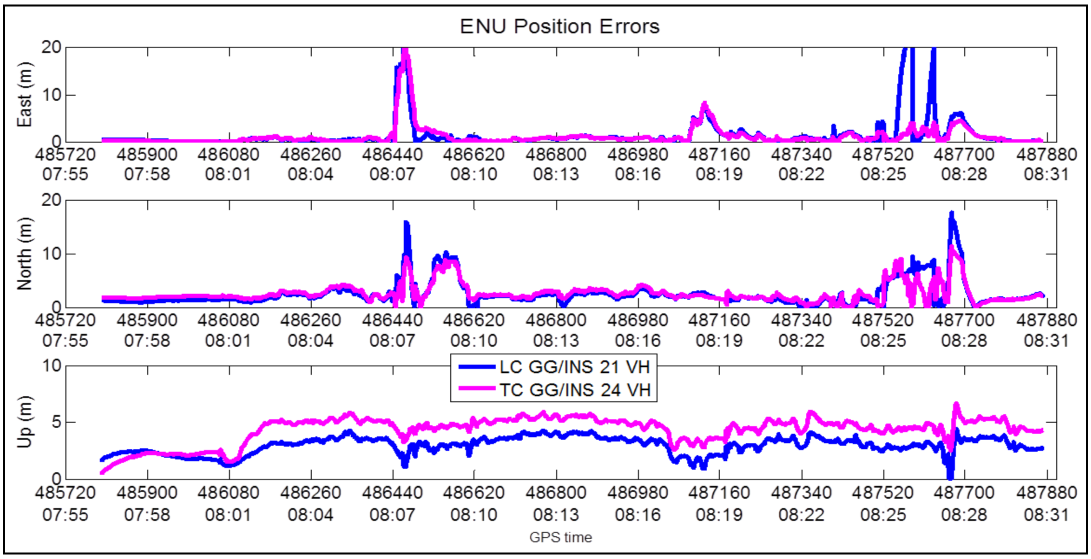

Figure 6-24 – Pedestrian Test: Position Error Comparison between LC GG/INS 21 VH and TC GG/INS 24 VH Configurations

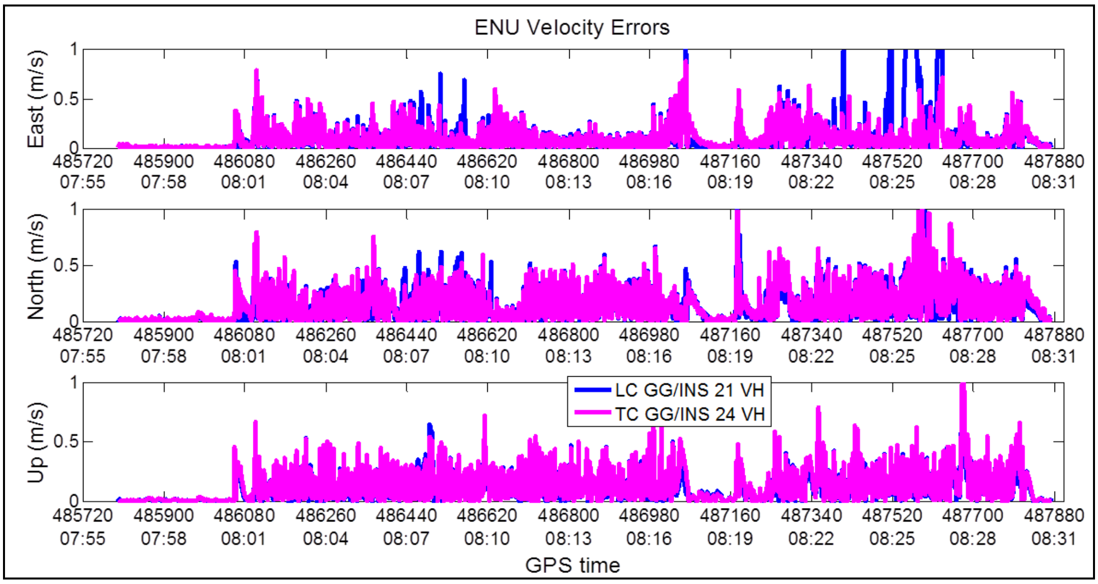

Figure 6-25 – Pedestrian Test: Velocity Error Comparison between LC GG/INS 21 VH and TC GG/INS 24 VH Configurations

In Table 6-11 a position error analysis is performed, considering the maximum and RMS horizontal, vertical and 3D error. From Table 6-11 it can be noted that the global performances of the two configurations are very similar; the TC configuration has a lower RMS horizontal error but a larger vertical error (only a difference of 1 meter in both cases). More interesting is the difference in the maximum error: the TC configuration has a maximum horizontal error (and consequently a 3D error) about 15 meters lower than LC.

Table 6-11 – Pedestrian Test: LC GG/INS 21 VH versus TC GG/INS 24 VH (Position Error Analysis)

	RMS Error (m)			*Maximum Error (m)*		
	Horizontal	*Vertical*	*3D*	*Horizontal*	*Vertical*	*3D*
LC GG/INS 21 VH	5,3	3,1	6,1	36,1	4,4	36,2
TC GG/INS 24 VH	4,1	4,5	6,0	22,6	6,6	22,9

To summarize the performances obtained in the pedestrian test, the more meaningful configurations considered with LC and TC architectures are compared in Figure 6-26.

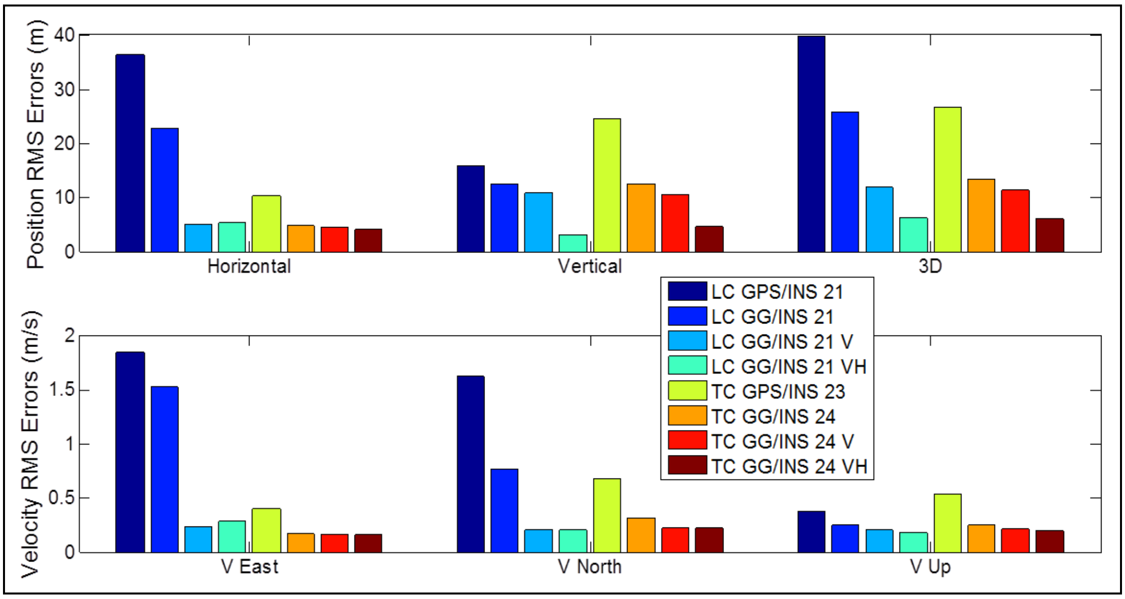

Figure 6-26 – Pedestrian Test: Comparison between LC and TC Architectures in terms of Position and Velocity RMS Errors

The main remarks deduced from the errors overview in Figure 6-26 are:

- In case of GPS/INS integration, TC architecture provides significantly better horizontal solution and slightly worse altitude result than LC;
- Including GLONASS observations in the integrated system GPS/INS provides meaningful performance improvements for both LC and TC architectures and for both position and velocity estimation;

- In case of GG/INS integration, TC architecture provides a better horizontal solution and similar altitude result relative to LC;
- The configurations LC GG/INS 21 and TC GPS/INS 23 provide very similar performance suggesting that the former might be a good (and relatively simple) replacement for the latter;
- Including velocity and height constraints produces significant improvements of LC and TC performance in terms of both position and velocity;
- The results obtained with the configurations LC GG/INS 21 V and TC GG/INS 24 V are very similar;
- The results obtained with the configurations LC GG/INS 21 VH and TC GG/INS 24 VH are very similar.

6.2 Vehicular Test

In this section a vehicular test is described and the results of different GNSS/INS configurations are presented. An similar approach to that adopted in the pedestrian experiment is carried out for the data analysis. First the GNSS only solution is presented and the satellite visibility is analyzed. Then an integrated basic configuration is analyzed and the various constraints are applied to find the best solution.

In the vehicular navigation context the attitude angles (especially the azimuth angle) become significant and are therefore analyzed in addition to position and velocity of the vehicle. The typical speeds characterizing the car navigation allow the use of the GNSS external heading aiding described in 5.6.

6.2.1 Equipment and Test Description

The adopted equipment used for this test is essentially the same used in the pedestrian test described in 6.1.2, namely:

- a Crista IMU device (MEMS-based) and
- a NovAtel ProPak-V3 receiver (GPS/GLONASS)

to test the proposed algorithms for the GNSS/INS integration and

- the NovAtel SPAN integrated system

to generate a reference solution with the accuracy summarized in Table 6-1 (processing the SPAN data in post-mission as described in 6.1.1).

All the equipment is placed on the roof of the car as shown in Figure 6-27.

Figure 6-27 – Vehicular Test Equipment

The data collection was carried out in a vehicle in downtown Calgary, Canada on 22nd July 2010 in the afternoon (about 2:00 pm local time). As previously mentioned downtown Calgary is a typical urban scenario, characterized by skyscrapers and so it is a difficult environment for satellite navigation because of blocking and multipath problems. The test begins in a small parking lot with a static period of 4 minutes, characterized by good visibility condition (9 GPS and 5 GLONASS available satellites) and continues into the downtown core where the number of visible satellites decreases significantly. The test finishes outside downtown with good visibility conditions. The total duration of the test is about 23 minutes; the speed of the vehicle varies from 0-50 km/h with frequent stops due to the traffic lights and the total distance travelled is about 10 km. The trajectory followed by the car is shown in Figure 6-28.

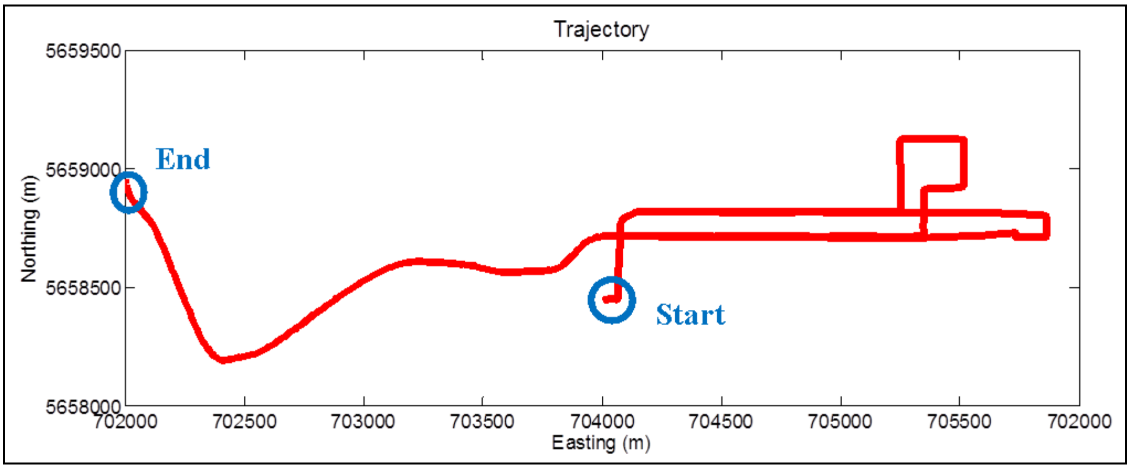

Figure 6-28 – Vehicular Test Trajectory

6.2.2 GNSS Solution

In this section the epoch by epoch single point GNSS only solution, obtained processing the pseudorange and Doppler observables with the WLS method, is provided. The number of visible GPS and GLONASS satellites is shown in Figure 6-29, with the corresponding GDOP behavior in the GPS only and GPS/GLONASS cases.

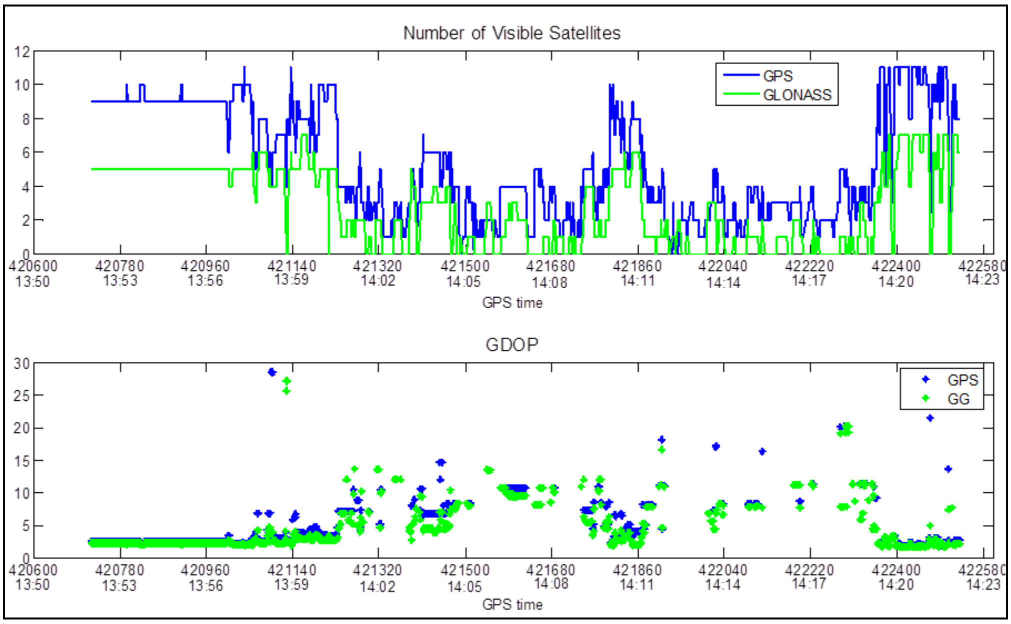

Figure 6-29 – Vehicular Test: Visibility and GDOP

The beginning of the test in a relatively open area is characterized by a large number of visible satellites and a low GDOP values, i.e. a good observation geometry. The test continues in a severe environment with a number of visible satellites decreases to between 6 and 0 for GPS and between 4 and 0 for GLONASS, with a noticeably degraded observation geometry (GDOP values larger than 30 are not plotted). The final part of the test is again in an open sky scenario (more than 10 available GPS satellites).

The test environment is very demanding for GPS only navigation, which is often inaccurate (owing to the bad geometry) or impossible (owing to the lack of observations); the inclusion of GLONASS improves the solution availability.

The GPS only solution availability is about 63% and the GPS/GLONASS availability is 68%, showing that the considered environment is very demanding (more so than the scenario considered in 6.1.2). This is primarily attributed to the fact that the previous test was conducted mostly on the edge of the downtown core, whereas this test passes directly through the center.

6.2.3 GNSS/INS Integrated Results

In this section the results obtained by integrating GNSS and INS MEMS-based data are discussed. To facilitate the data analysis, three segments of trajectory are considered and examined separately (Figure 6-30).

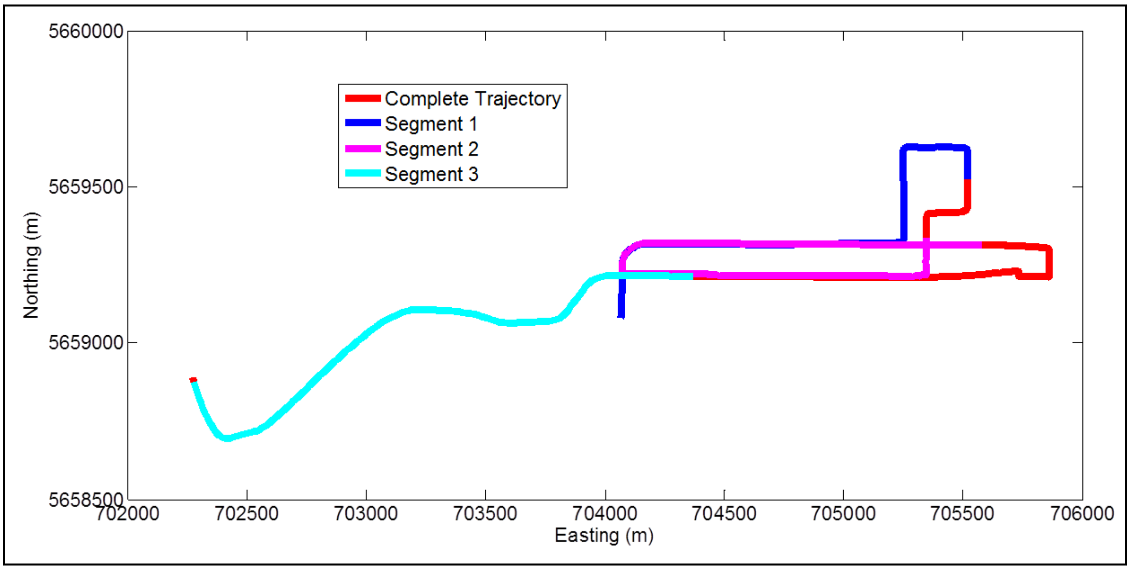

Figure 6-30 – Vehicular Test: Segments of Trajectory

Segment 1

The segment 1 is approximately 2.5 km long, and was travelled in about 7 minutes. The first part is characterized by a good visibility (5-11 GPS satellites and 0-7 GLONASS satellites), followed by an area with few visible satellites (0-4 GPS and 0-2 GLONASS); in the final part of the segment 6 GPS satellites and 3 GLONASS are in view (Figure 6-31).

The GPS solution availability is about 73% and the GPS/GLONASS solution availability is about 81%.

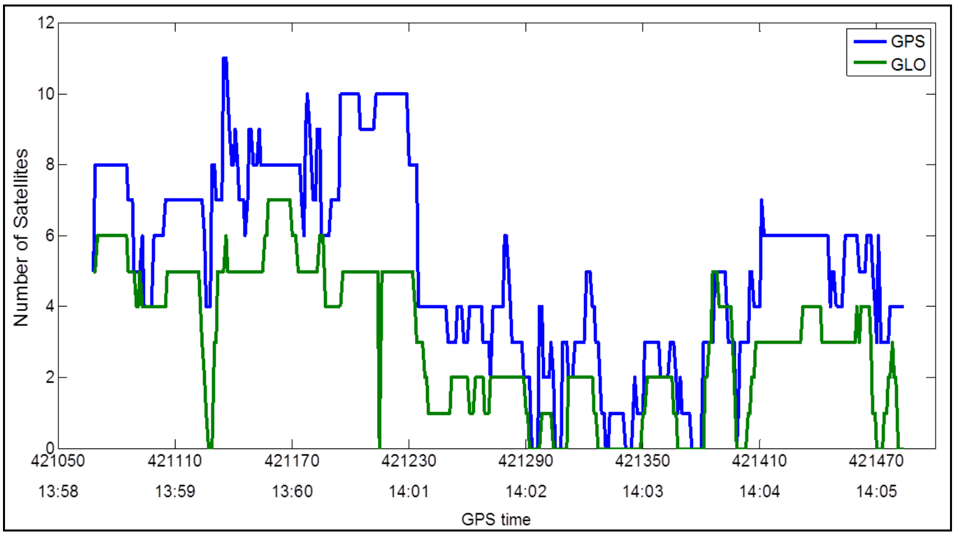

Figure 6-31 – Vehicular Test: Visibility (Segment 1)

The number of visible GPS satellites is plotted on the segment trajectory in Figure 6-32, showing frequent partial and total GPS outages, particularly in the second part of the long straight stretch and around the second and third turn (located near the center of downtown Calgary); the longest GPS outage (less than 4 satellites) duration is about 60 seconds between the just mentioned turns (highlighted by a dotted circle in Figure 6-32).

In case of GLONASS satellite inclusion, the above-mentioned outage is interrupted by a combined GPS/GLONASS fix as shown in Figure 6-33.

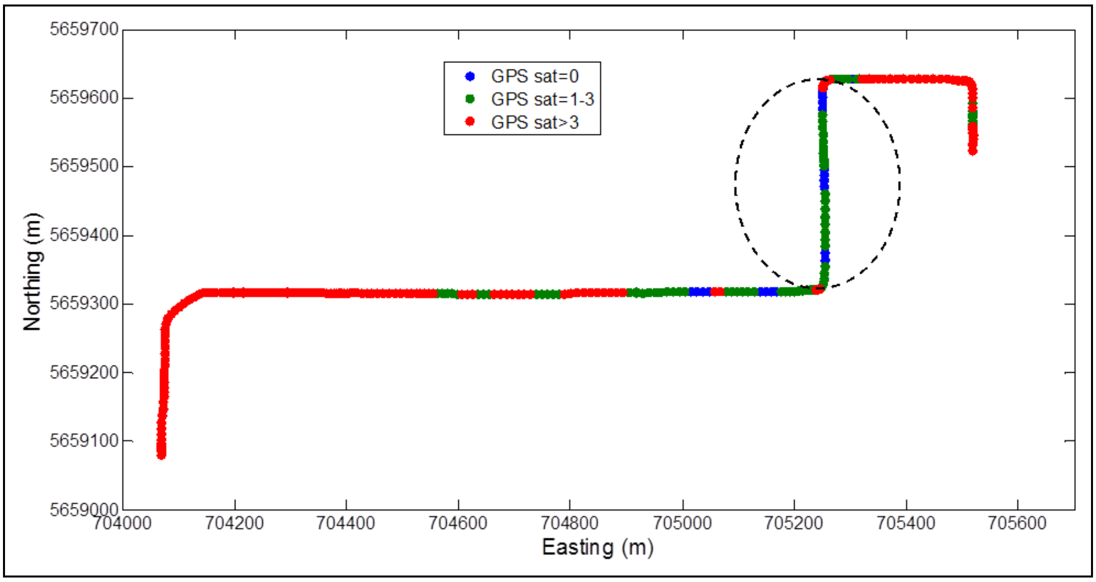

Figure 6-32 – Vehicular Test: Number of Visible GPS Satellites on Trajectory (Segment 1)

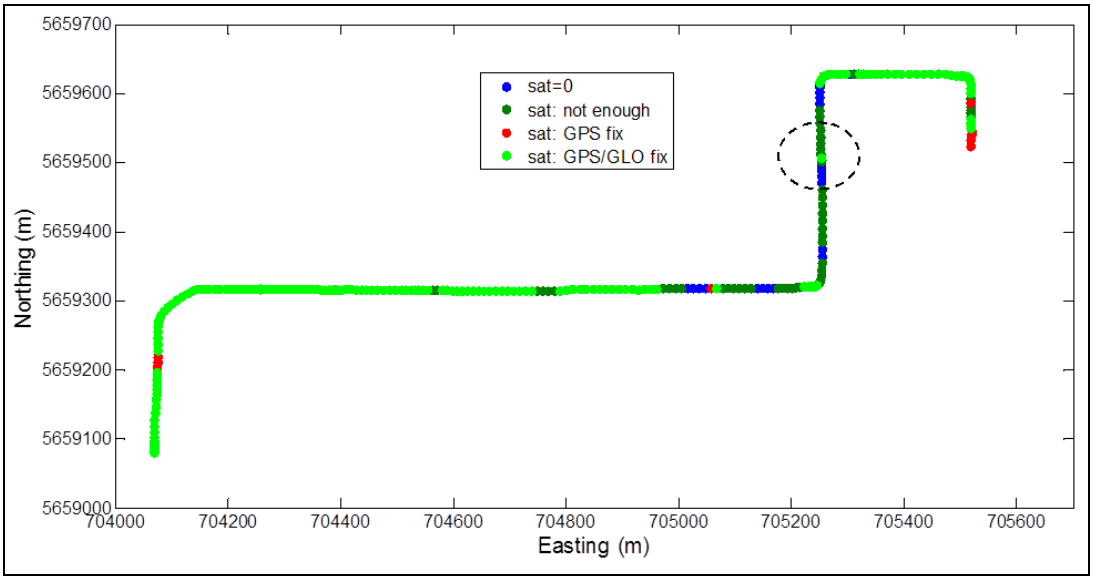

Figure 6-33 – Vehicular Test: GPS/GLONASS Positioning on the Trajectory (Segment 1)

With this in mind, the benefit of GLONASS inclusion is clear in Figure 6-34, showing the trajectories obtained with the LC GPS/INS 21 and LC GG/INS 21 configurations. The isolated GPS/GLONASS fix (circled in Figure 6-33) which interrupts the largest GPS outage, allows the trajectory to stay relatively near the reference between the second and the third turns, whereas without GLONASS large errors occur. The LC GG/INS 21 configuration provides better performance also during the second part of the long straight stretch (between easting values of 705000 and 705200), where LC GPS/INS 21 error tends to grow owing to short GPS only outages (15-20 seconds duration).

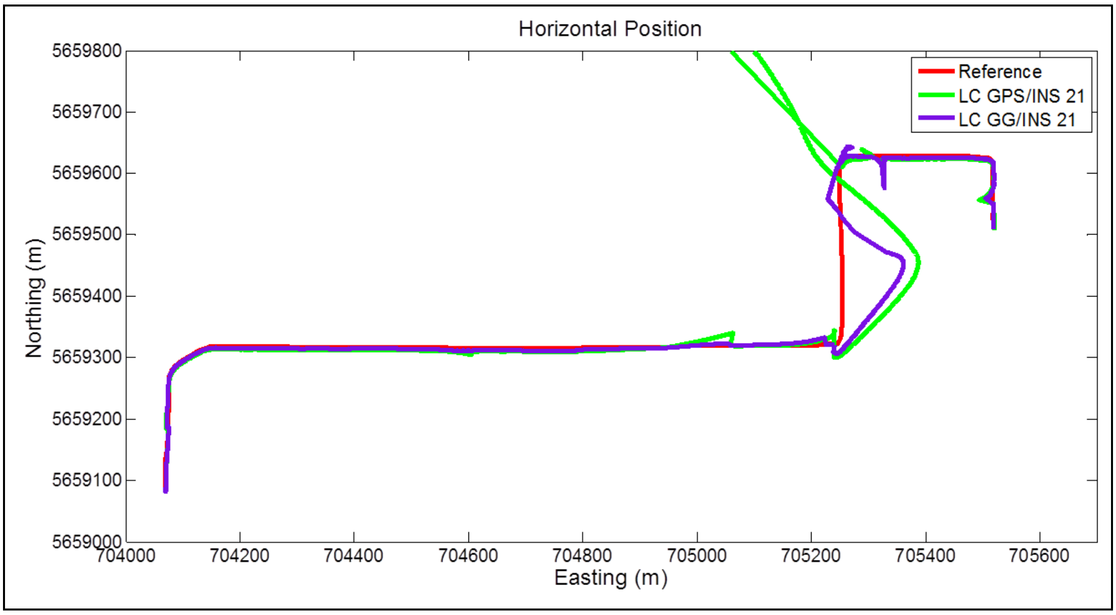

Figure 6-34 – Vehicular Test: Trajectory of LC GPS/INS 21 and LC GG/INS 21 Configurations (Segment 1)

Table 6-12 and Table 6-13 summarize the comparison between the considered configurations, providing the position, velocity and attitude errors (RMS and maximum). The configuration including GLONASS measurements shows significantly better performance in terms of all the considered parameters.

Table 6-12 – Vehicular Test: RMS and Maximum Errors of LC GPS/INS 21 Configuration (Segment 1)

	RMS Error			*Maximum Error*		
	East	*North*	*Up*	*East*	*North*	*Up*
Position (m)	48,4	48,7	16,3	347,0	341,2	48,0
Velocity (m/s)	4,6	3,6	0,3	26,5	22,4	1,1
	Roll	*Pitch*	*Yaw*	*Roll*	*Pitch*	*Yaw*
Attitude (deg)	1,4	1,7	34,5	4,2	7,4	79,9

Table 6-13 – Vehicular Test: RMS and Maximum Errors of LC GG/INS 21 Configuration (Segment 1)

	RMS Error			*Maximum Error*		
	East	*North*	*Up*	*East*	*North*	*Up*
Position (m)	20,2	15,0	8,0	109,6	51,2	34,4
Velocity (m/s)	1,6	1,2	0,3	7,7	9,6	1,4
	Roll	*Pitch*	*Yaw*	*Roll*	*Pitch*	*Yaw*
Attitude (deg)	1,4	1,2	24,5	4,1	7,4	65,6

In the above error tables it is notable that the maximum yaw error (and thus the RMS error) is very large relative to roll and pitch; this is because in the absence of horizontal acceleration (stationary vehicle) the yaw errors are not very well observable and thus the error grows (Godha 2006). However, when the vehicle moves, the yaw tends to converge, but the converged value, owing to large sensor noise and poor observability, has large errors.

A possible approach to improve the accuracy of the estimated yaw and to aid the convergence process is to explicitly use GNSS-derived yaw as an external aid (as explained in 5.5). The GNSS-derived yaw is computed using the formula (5-34) and its accuracy is expressed by (5-35), so the yaw accuracy is inversely proportional to the GNSS-derived horizontal velocity. From Figure 6-35 it is shown that when GNSS-derived horizontal velocity is larger than 5 m/s, the GNSS-derived yaw agrees well with the reference and only in that case the considered yaw aiding is used.

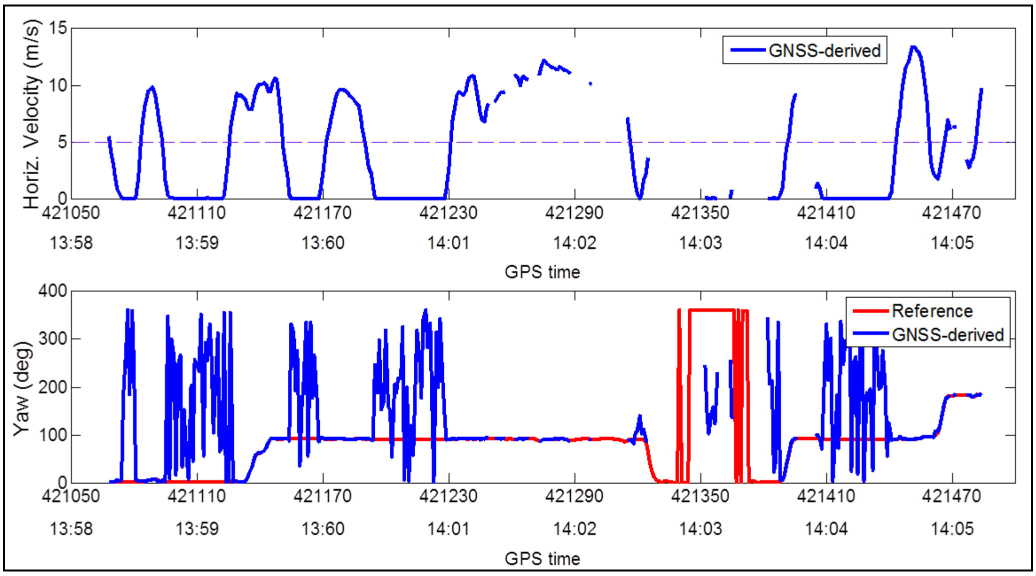

Figure 6-35 – Vehicular Test: GNSS-derived Horizontal Velocity and Yaw

The effectiveness of the GNSS-derived yaw aiding is shown by assessing the navigation solution obtained in the configuration LC GG/INS 21 with yaw aiding (indicated as LC GG 21 Y) and comparing it with the no yaw aiding case. The trajectories obtained with the two configurations are shown in Figure 6-36; the yaw external aiding yields solution improvements, reducing the disagreements with the reference. The spike on the trajectory obtained without the aiding (circled in Figure 6-36) is smoothed. Table 6-14 summarizes the errors, and shows improvements on all the navigation parameters relative to Table 6-13.

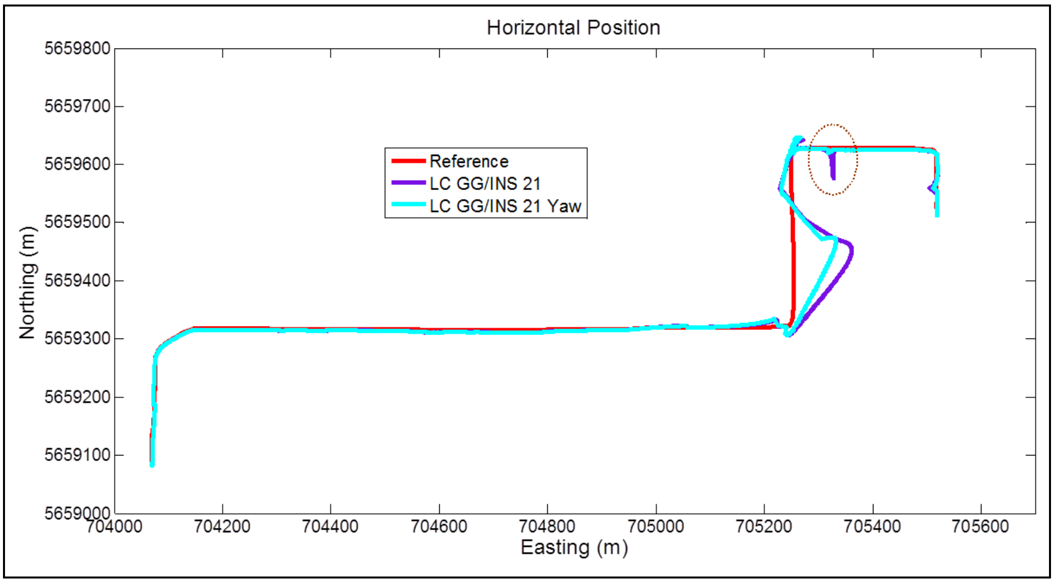

Figure 6-36 – Vehicular Test: Trajectory of LC GG/INS 21 and LC GG/INS 21 Y (Segment 1)

Table 6-14 – Vehicular Test: RMS and Maximum Errors of LC GG/INS 21 Y Configuration (Segment 1)

	RMS Error			*Maximum Error*		
	East	*North*	*Up*	*East*	*North*	*Up*
Position (m)	15,0	12,9	7,6	80,1	48,2	33,1
Velocity (m/s)	1,3	0,5	0,3	5,8	2,1	1,3
	Roll	*Pitch*	*Yaw*	*Roll*	*Pitch*	*Yaw*
Attitude (deg)	0,9	0,9	15,4	3,6	7,4	49,5

As in the pedestrian test (section 6.1.4), motion constraint equations on velocity and height (section 5.6) can be included to further enhance the integrated system performance. The configuration obtained adding the velocity constraints to the LC GG/INS 21 Y configuration is referred to as LC GG/INS 21 YV; the configuration obtained adding the height constraint too is referred to as LC GG 21 YVH.

The trajectories obtained with both LC GG/INS 21 YV and LC GG/INS 21 YVH configurations are compared with the configuration LC GG/INS 21 Y in Figure 6-37. In the area circled in Figure 6-37 it is evident the improvements obtained including the motion constraints which allow a better agreement with the reference; comparing the trajectories obtained considering only the velocity constraints and the velocity/height constraints results a better behavior in the last case as shown in circled area.

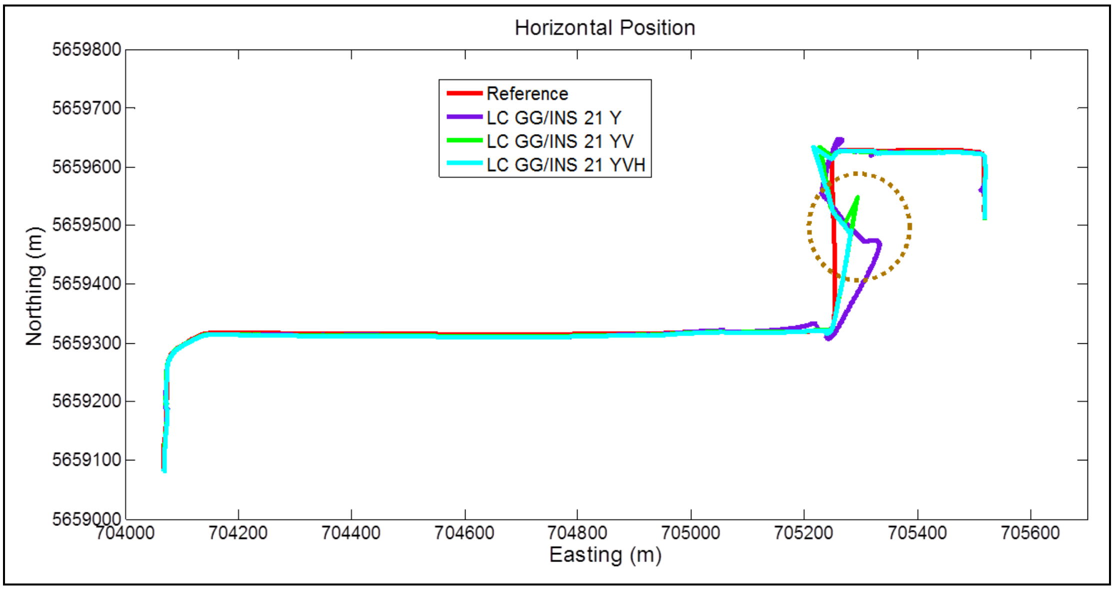

Figure 6-37 – Vehicular Test: Trajectory of LC GG/INS 21 Y, LC GG/INS 21 YV and LC GG/INS 21 YVH (Segment 1)

The LC GG/INS 21 YV and LC GG/INS 21 YVH errors are summarized in Table 6-15 and Table 6-16; in the first case the maximum position error is about 40 and the RMS less than 10 meters. In the last case the maximum position error is reduced to 30 meters and the RMS error is almost unchanged; in the last case the maximum azimuth error worsen of some degrees.

The application of the motion constraints reduces significantly the position, the velocity and the azimuth errors with respect to the previously considered case (LC GG/INS 21 Y).

Table 6-15 – Vehicular Test: RMS and Maximum Errors of LC GG/INS 21 YV Configuration (Segment 1)

	RMS Error			***Maximum Error***		
	East	*North*	*Up*	*East*	*North*	*Up*
Position (m)	8,1	6,6	3,8	41,9	40,0	8,8
Velocity (m/s)	0,6	0,5	0,1	2,4	4,3	0,3
	Roll	*Pitch*	*Yaw*	*Roll*	*Pitch*	*Yaw*
Attitude (deg)	0,7	0,9	4,9	3,0	3,0	14,1

Table 6-16 – Vehicular Test: RMS and Maximum Errors of LC GG/INS 21 YVH Configuration (Segment 1)

	RMS Error			***Maximum Error***		
	East	*North*	*Up*	*East*	*North*	*Up*
Position (m)	7,9	5,6	3,9	33,9	20,5	6,3
Velocity (m/s)	0,7	0,4	0,1	3,0	2,0	0,3
	Roll	*Pitch*	*Yaw*	*Roll*	*Pitch*	*Yaw*
Attitude (deg)	0,7	1,0	6,5	3,0	3,0	22,3

To perform a concise comparison among the analyzed configurations with LC architecture, the RMS errors of position, velocity and attitude are represented with a bar chart in Figure 6-38.

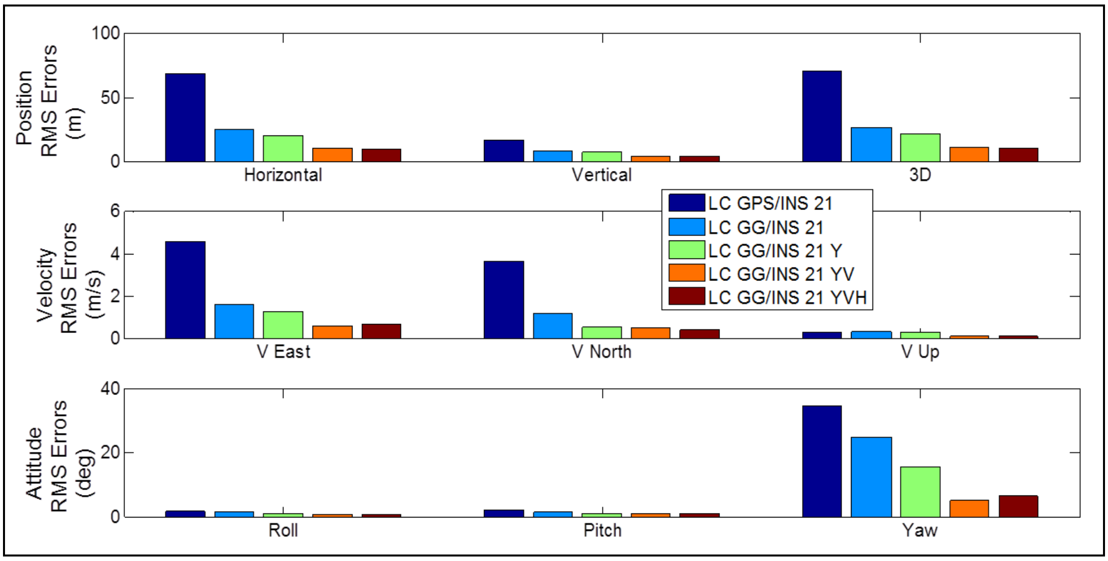

Figure 6-38 – Vehicular Test: Comparison between LC Configurations in terms of Position, Velocity and Attitude RMS Errors (Segment 1)

From Figure 6-38 it results clear the benefit of including GLONASS observations in the integrated system in terms of all the navigation parameter errors; adding the GNSS-derived azimuth aiding strongly influences the azimuth estimation and reduces the position and velocity errors too. Using the motion constraints further improves the integrated system performance in term of all the considered parameters; the two constraint-aided configurations LC GG/INS YV and LC GG/INS YVH provide similar RMS errors of about 10 meters in 3D position.

Unlike LC architecture, the TC architecture is able to compute an integrated position in case of partial GNSS outages too; this makes the TC usually more effective in the urban environment (characterized by frequent partial outages). For this reason, the TC GPS/INS 23 configuration, whose trajectory is shown in Figure 6-39 (cyan line), shows better performance than the corresponding LC configuration (LC GPS/INS 21 represented by green line), without large drift in the trajectory.

Including GLONASS observations in the TC GPS/INS 23 configuration, the TC GG/INS 24) configuration is obtained, which shows only slight enhancements in the solution (magenta line in Figure 6-39) relative to TC GPS/INS 23 case.

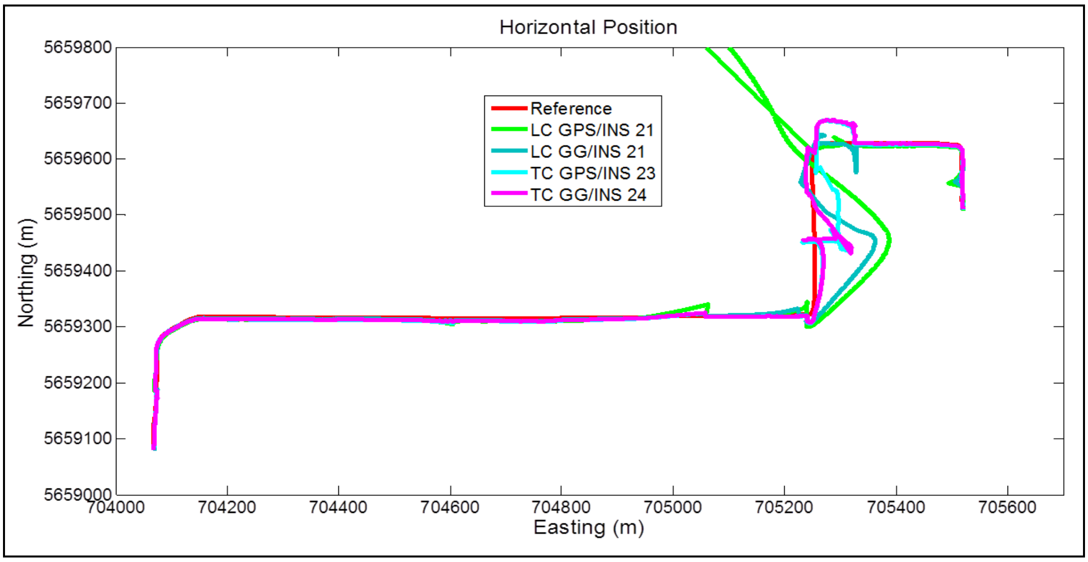

Figure 6-39 – Vehicular Test : Trajectories of LC GPS/INS 21, LC GG/INS 21, TC GPS/INS 23 and TC GG/INS 24 Configurations (Segment 1)

The RMS errors obtained with the four configurations, LC GPS/INS 21, LC GG/INS 21, TC GPS/INS 23 and TC GG/INS 24, are analyzed in Figure 6-40.

LC GPS/INS 21 configuration shows large errors, which are strongly reduced in the corresponding TC case (TC GPS/INS 23) or including GLONASS measurements in LC architecture (LC GG/INS 21). LC GG/INS 21 and TC GPS/INS 23 configurations demonstrate very similar performances for all the navigation parameters, which is consistent with the pedestrian results as well. Both solutions are only slightly worse than the TC GG/INS 24 case.

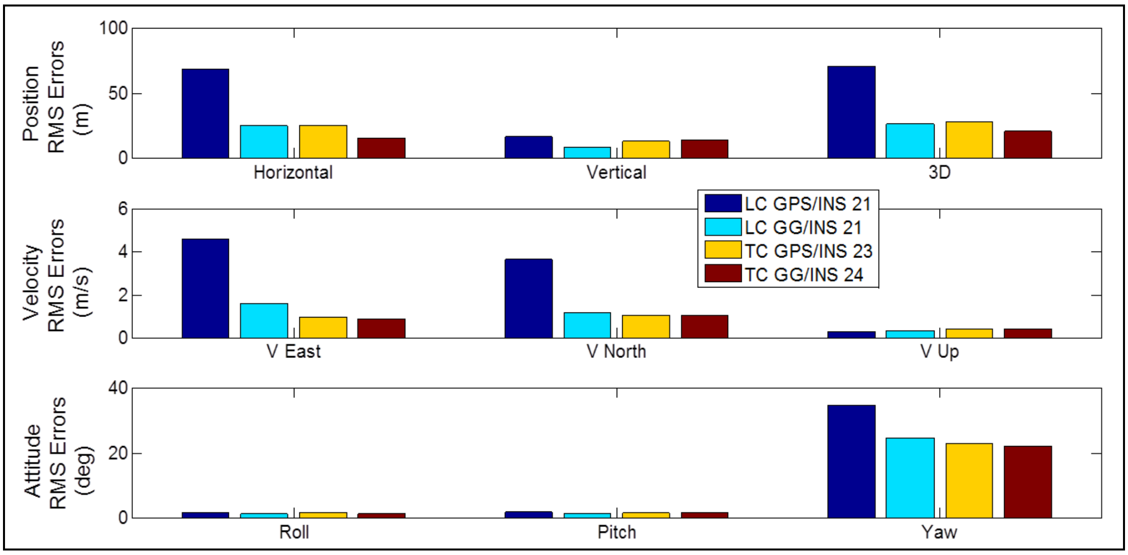

Figure 6-40 – Vehicular Test: Comparison between Configurations LC GPS/INS 21, LC GG/INS 21, TC GPS/INS 23 and TC GG/INS 24 in terms of Position, Velocity and Attitude RMS Errors (Segment 1)

To further improve the TC solution, similar to what was done with LC approach, the GNSS-derived yaw aiding and the velocity and height motion constraints can be included in the integrated system GNSS/INS; the configurations including the yaw aiding (TC GG/INS 24 Y), the velocity constrains and the yaw aiding (TC GG/INS 24 YV) and the velocity/height constraints and the yaw aiding (TC GG/INS 24 YVH) are considered and the obtained trajectories are presented in Figure 6-41. The trajectory obtained with TC GG/INS 24 Y configuration shows some disagreements between the second and the third turns, while including the motion constraints a small drift is present on the long East-West straight stretch.

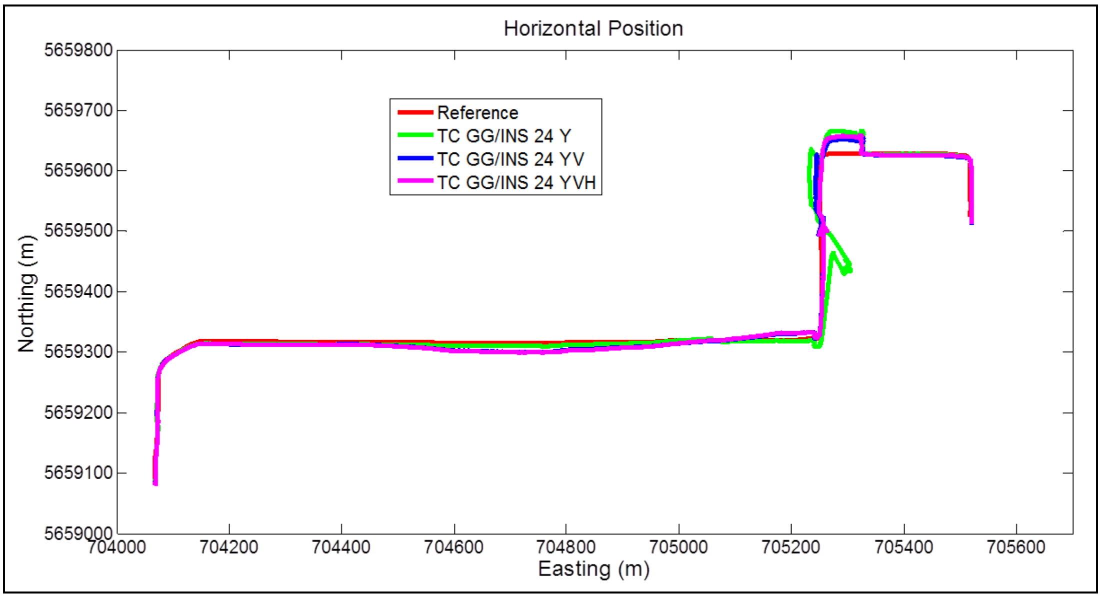

Figure 6-41 – Vehicular Test: Trajectories of TC GG/INS 24 Y, TC GG/INS 24 YV and TC GPS/INS 24 YVH Configurations (Segment 1)

To better perform a comparison among the analyzed configurations with TC architecture, the RMS errors of position, velocity and attitude are represented with a bar chart in Figure 6-42.

The enhancements of including GLONASS observations are most notable on the horizontal position (dark blue and blue bars representing TC GPS/INS 23 and TC GG/INS 24 configurations respectively). The GNSS-derived yaw aiding improves significantly the azimuth estimation, slightly degrading the position errors (by few meters of RMS error). Adding the velocity constraints too, clearly improves the integrated system performance in terms of all the navigation parameters (with only a loss of accuracy in azimuth estimation). Finally also using the height constraint (i.e. configuration TC GG/INS 24 YVH), the best results for the TC architecture are obtained; the RMS and maximum errors in position, velocity and attitude are summarized in Table 6-17.

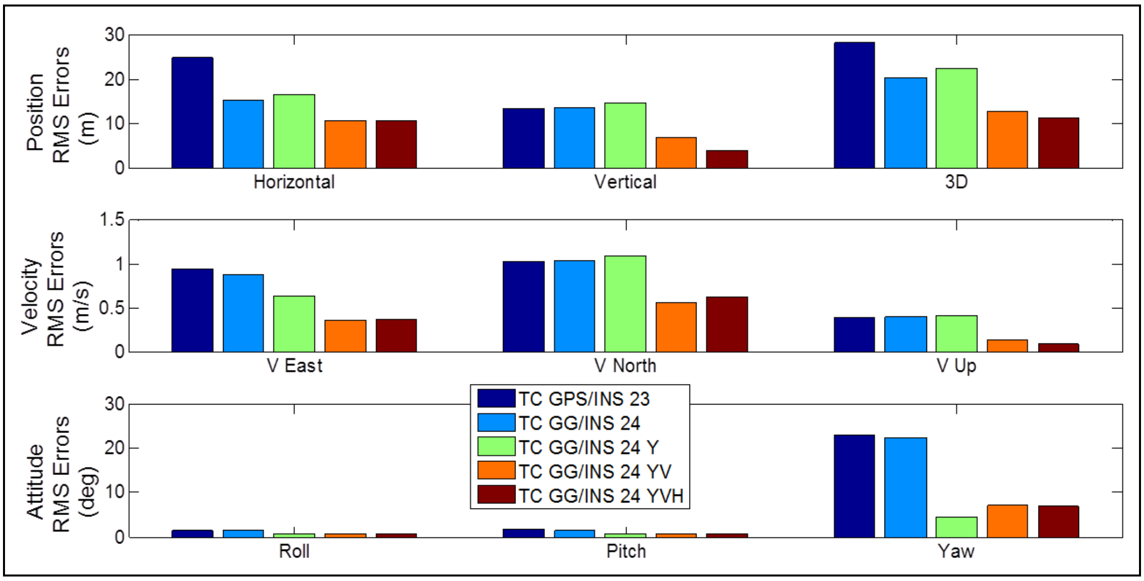

Figure 6-42 – Vehicular Test: Comparison between TC Configurations in terms of Position, Velocity and Attitude RMS Errors (Segment 1)

Table 6-17 – Vehicular Test: RMS and Maximum Errors of TC GG/INS 24 YVH Configuration (Segment 1)

	RMS Error			***Maximum Error***		
	East	*North*	*Up*	*East*	*North*	*Up*
Position (m)	4,8	9,5	4,0	18,4	30,5	6,4
Velocity (m/s)	0,4	0,6	0,1	2,0	3,0	0,3
	Roll	*Pitch*	*Yaw*	*Roll*	*Pitch*	*Yaw*
Attitude (deg)	0,7	0,7	6,9	2,8	3,0	23,2

To summarize the performances obtained in the segment 1 of the vehicular test, the more meaningful configurations considered with LC and TC architectures are compared in Figure 6-43.

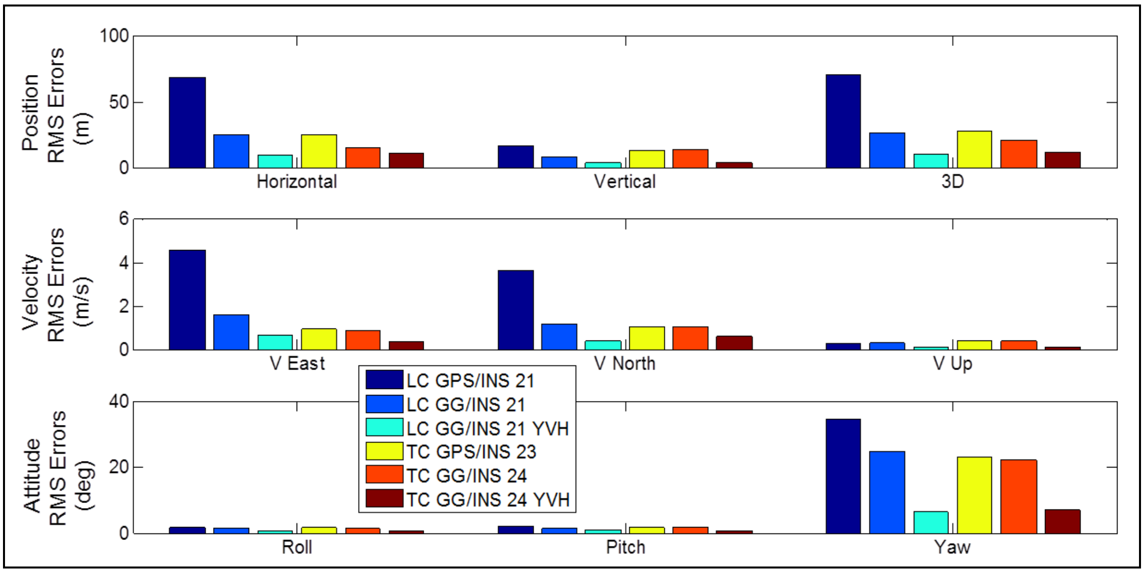

Figure 6-43 – Vehicular Test: Comparison between LC and TC Architectures in terms of Position and Velocity RMS Errors (Segment 1)

The main remarks deduced from the errors overview in Figure 6-43 are:

- In case of GPS/INS integration, TC architecture provides significantly better horizontal solution and similar altitude result than LC;
- Including GLONASS observations in the integrated system GPS/INS provides meaningful performance improvements for both LC and TC architectures and in terms of position, velocity and azimuth estimation;
- In case of GG/INS integration, TC architecture provides only slightly better solution relative to LC;
- The configurations LC GG/INS 21 and TC GPS/INS 23 provide very similar performance, as in the pedestrian case;
- Including GNSS-derided azimuth aiding and velocity/height constraints produces significant improvements of LC and TC performance in terms of position, velocity and azimuth;
- The results obtained with the configurations LC GG/INS 21 YVH and TC GG/INS 24 YVH are very similar.

Segment 2

The segment 2 is approximately 3 km long, travelled in about 7 minutes. The number of visible GPS satellites on the trajectory is presented in Figure 6-44, showing two long partial/total GPS outages (about 60 seconds) on the two east/west straight sections, connected by a turn with a sufficient visibility to continuously perform a GPS fix. The inclusion of GLONASS (Figure 6-45) does not allow a reduction in the outage durations; in fact the GPS solution availability is about 53% and the GPS/GLONASS solution availability is only 55%.

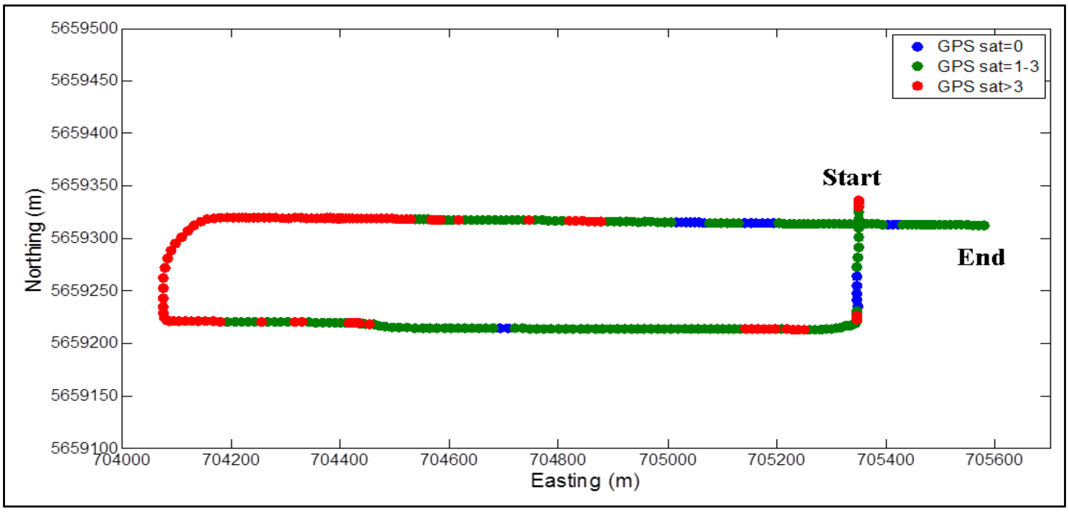

Figure 6-44 – Vehicular Test: Number of Visible GPS Satellites on the Trajectory (Segment 2)

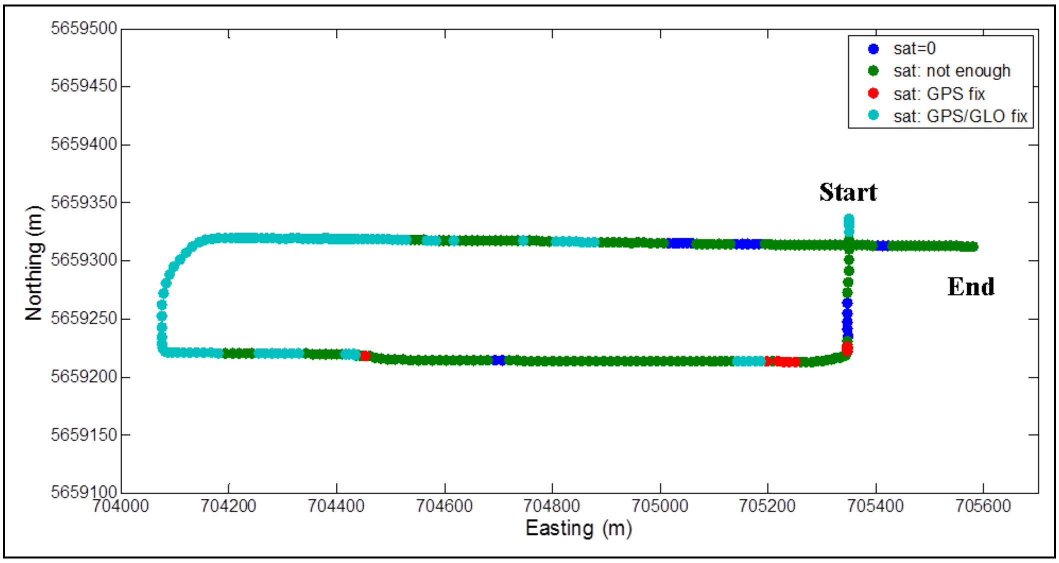

Figure 6-45 – Vehicular Test: Positioning on the Trajectory (Segment 2)

In these severe conditions, a solution including only GPS and INS measurements merged in a LC approach (LC GPS/INS 21) presents large errors during the GPS outages (green line in Figure 6-46). The inclusion of GLONASS does not improve visibility in the critical areas, so the solution of LC GG/INS 21 configuration shows similar large errors (purple line in Figure 6-46). The constraints considered in this research are tested to try to improve the results in loose architecture; the solution of LC

GG/INS 21 YVH configuration presents however large disagreements with the reference during the long GNSS outages.

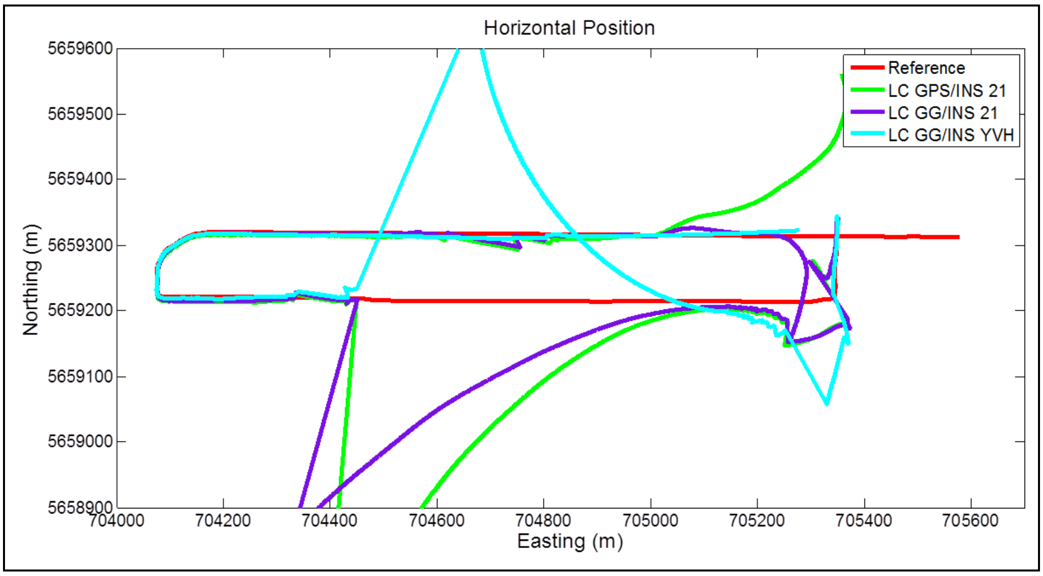

Figure 6-46 – Vehicular Test: Trajectory of LC GPS/INS 21, LC GG/INS 21 and LC GG/INS 21 YVH Configurations (Segment 2)

Hence it is clear that the LC approach does not provide satisfying performances for each tested configuration. The analysis thus shifts to the TC solution where superior performance is obtained.

The solution including only GPS and INS measurements integrated in a TC approach (TC GPS/INS 23) does not present large errors during the GPS outages as in the corresponding LC case; in Figure 6-47 the trajectory obtained is shown (green line).

A slightly better trajectory is obtained by including GLONASS measurements (configuration TC GG/INS 24), as shown in Figure 6-47 with the purple line.

A further trajectory improvement is obtained including the yaw and the motion constraints (configuration TC GG/INS 24 YVH) as shown in Figure 6-47 with the cyan line. The errors of position, velocity and attitude of this configuration are summarized in Table 6-18. The maximum position errors (and consequently the RMS errors) are significantly larger with respect to the segment 1, owing to the very severe scenario.

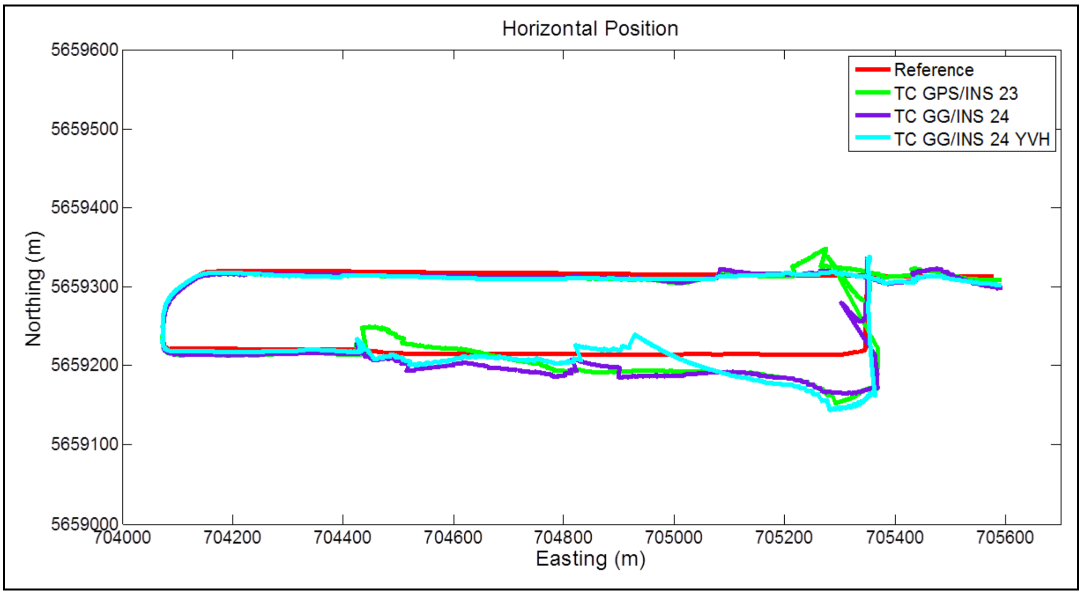

Figure 6-47 – Vehicular Test: Trajectory of TC GPS/INS 23, TC GG/INS 24 and TC GG/INS 24 YVH Configurations (Segment 2)

Table 6-18 – Vehicular Test: RMS and Maximum Errors of TC GG/INS 24 YVH Configuration (Segment 2)

	RMS Error			***Maximum Error***		
	East	*North*	*Up*	*East*	*North*	*Up*
Position (m)	7,3	18,3	3,3	24,4	68,2	6,8
Velocity (m/s)	0,5	1,1	0,1	2,1	5,1	0,4
	Roll	*Pitch*	*Yaw*	*Roll*	*Pitch*	*Yaw*
Attitude (deg)	1,1	1,1	10,9	3,3	3,9	49,4

To summarize the performances obtained in the segment 2 of the vehicular test with the TC architecture, the more meaningful configurations are compared in Figure 6-48.

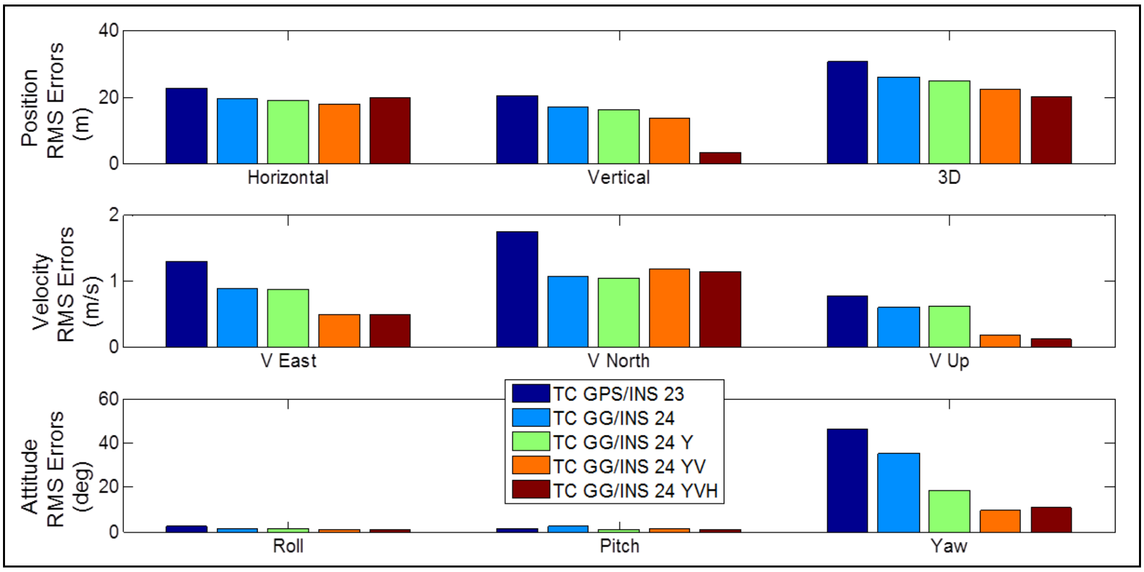

Figure 6-48 – Vehicular Test: Comparison between TC Configurations in terms of Position, Velocity and Attitude RMS Errors (Segment 2)

The main remarks deduced from the errors overview in Figure 6-48 and from the analysis carried out in the current sub-section are:

- The GNSS/INS integration in LC architecture does not provide satisfying performance for each tested configuration (with GPS and GLONASS, with GNSS-derived yaw aiding, with motion constraints), showing large errors during GNSS outages;
- The GNSS/INS integration in TC architecture shows better performance relative to LC architecture for each tested configuration;
- Including GLONASS observations in the integrated system GPS/INS provides slight performance improvements for TC architecture in terms of position, velocity and azimuth estimation;
- Including the yaw external aiding in the TC GG/INS 24 configuration improves significantly only the azimuth estimation;
- Including the velocity constraints in the TC GG/INS 24 Y configuration slightly improves the estimation of position, velocity and azimuth;
- The configurations TC GG/INS 24 YV and TC GG/INS 24 YVH provide similar results, with only a better altitude estimation of the last configuration.

Segment 3

The segment 3 is approximately 2.5 km long and is travelled in about 3 minutes. The number of visible GPS satellites during the trajectory is presented in Figure 6-49; after some short partial GPS outages (few seconds) at the beginning of the path, the satellite visibility allows almost continuous GPS positioning. Only two short outages were encountered on the trajectory.

Inclusion of GLONASS (Figure 6-50) further increases the number of available satellites, reducing the durations of the outages; the GPS solution availability is about 81% and the GPS/GLONASS solution availability is 86%.

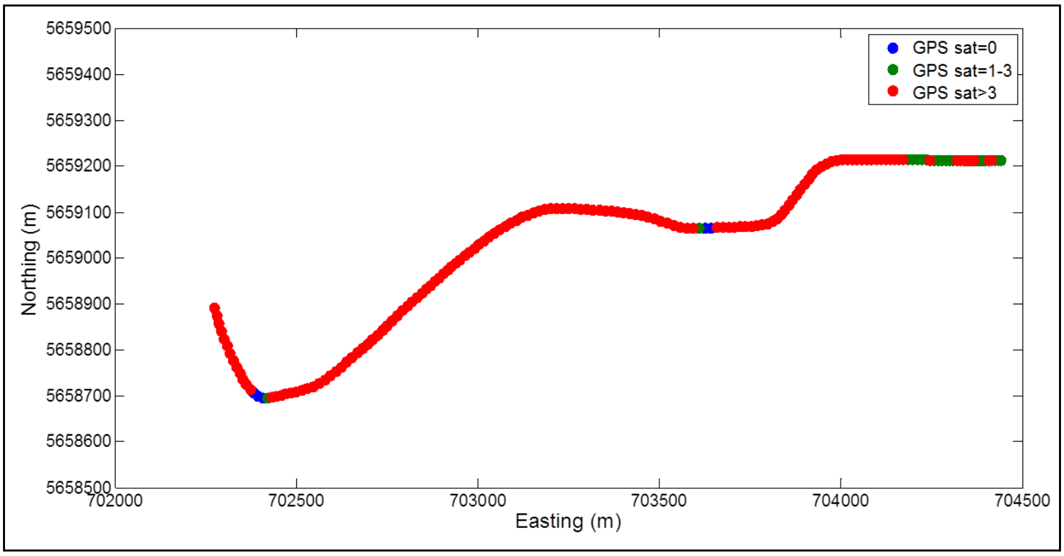

Figure 6-49 – Vehicular Test: Number of Visible GPS Satellites on the Trajectory (Segment 3)

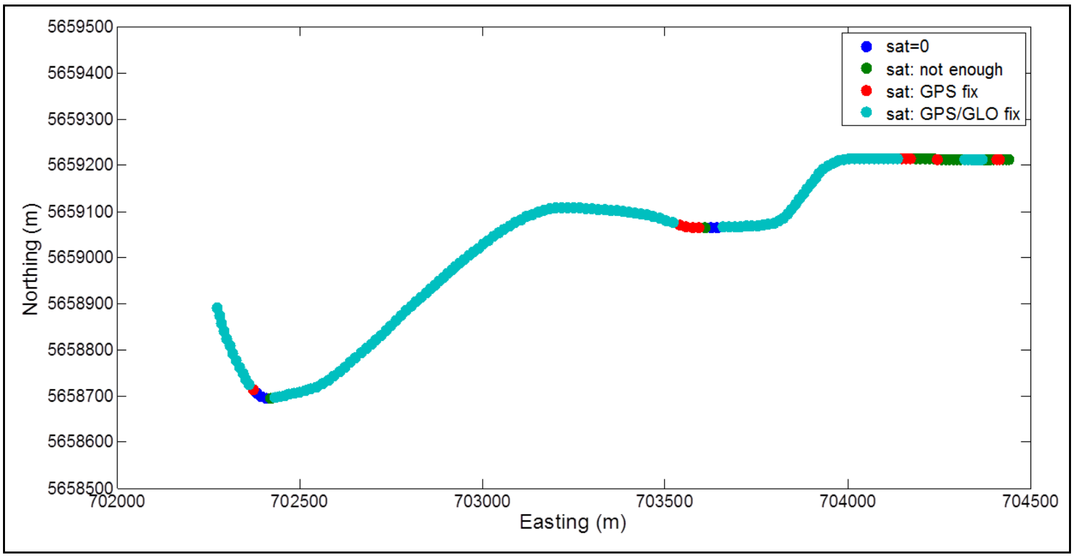

Figure 6-50 – Vehicular Test: GPS/GLONASS Solution Availability on the Trajectory (Segment 3)

The trajectory obtained by integrating GPS and INS in LC approach is presented in Figure 6-51 (green line). During the beginning of the segment, the trajectory shows some disagreements with the reference, owing to the partial GPS outages. However, during the remaining part of the segment, with a good satellite visibility, the obtained trajectory is very close to the reference. Including the GLONASS measurements (purple line) yields a reduction of the initial disagreements, as expected.

With the addition of the GNSS-derived yaw aiding and the motion constraints on velocity and height, the obtained trajectory (cyan line) is close to the reference during the whole segment. The Table 6-19 summarizes the error behavior of the last considered configuration (LC GPS/INS 21 YVH); the RMS position errors are about few meters, the maximum position error about 15 meters.

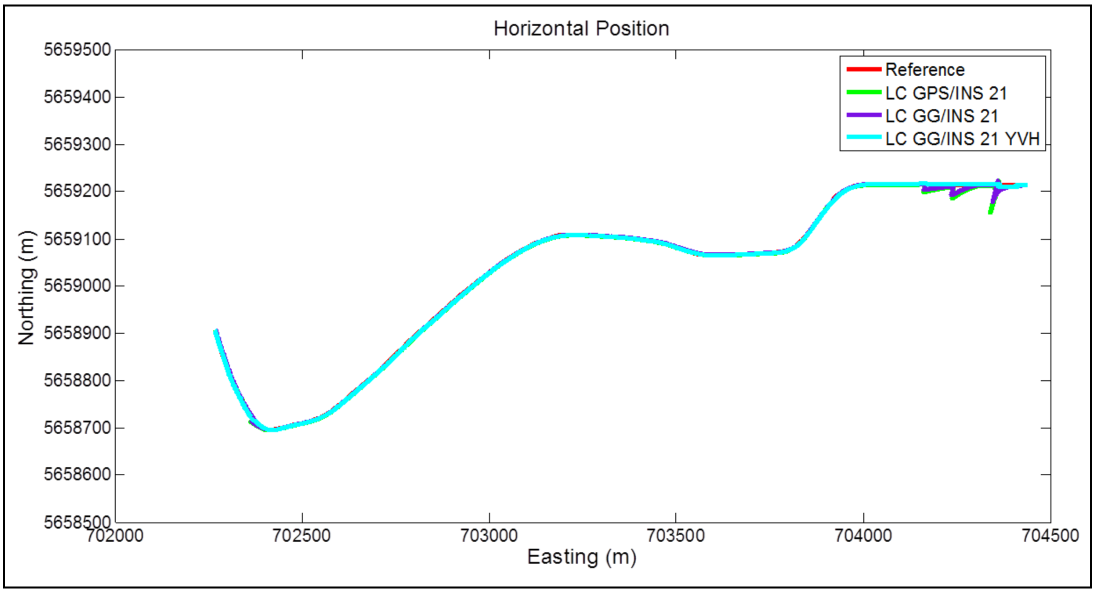

Figure 6-51 – Vehicular Test: Trajectory of LC GPS/INS 21, LC GG/INS 21 and LC GG/INS 21 YVH Configurations (Segment 3)

Table 6-19 – Vehicular Test: RMS and Maximum Errors of LC GG/INS 21 YVH Configuration (Segment 3)

	RMS Error			***Maximum Error***		
	East	*North*	*Up*	*East*	*North*	*Up*
Position (m)	6,1	3,7	3,4	13,5	7,3	5,1
Velocity (m/s)	0,3	0,5	0,1	1,6	1,9	0,4
	Roll	*Pitch*	*Yaw*	*Roll*	*Pitch*	*Yaw*
Attitude (deg)	1,0	1,0	1,5	2,2	2,3	7,6

A similar analysis is now carried out for the TC approach. The trajectory obtained integrating GPS and INS in TC approach is presented in Figure 6-52 (green line). In case of good visibility, the obtained trajectory is very close to the reference; some evident disagreements show up during the GPS outages at the beginning of the segment. Again, including the GLONASS measurements (purple line) yields a reduction of the above mentioned disagreements. Adding the GNSS-derived yaw aiding and the velocity and height motion constraints, the obtained trajectory (cyan line) is close to the reference during the whole segment. In the Table 6-20 the position, velocity and attitude errors of the TC GPS/INS 24 YVH configuration are summarized; the RMS position errors are about few meters, the maximum position error about 10 meters.

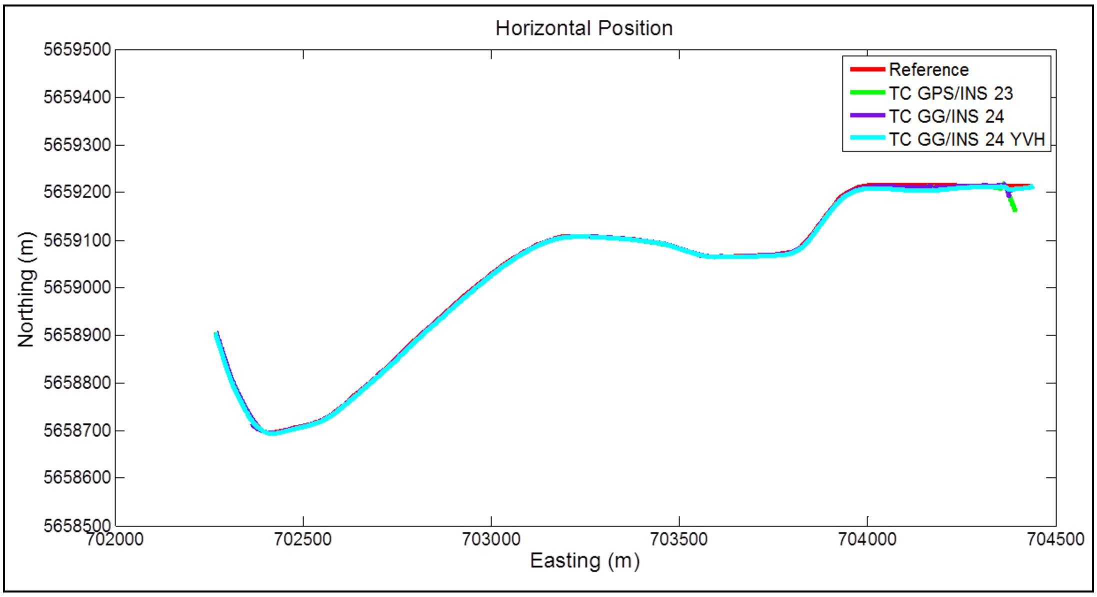

Figure 6-52 – Vehicular Test: Trajectory of TC GPS/INS 23, TC GG/INS 24 and TC GG/INS 24 YVH Configurations (Segment 3)

Table 6-20 – Vehicular Test: RMS and Maximum Errors of TC GG/INS 24 YVH Configuration (Segment 3)

	RMS Error			***Maximum Error***		
	East	*North*	*Up*	*East*	*North*	*Up*
Position (m)	6,2	5,7	5,5	8,6	11,5	9,9
Velocity (m/s)	0,3	0,6	0,1	1,3	1,8	0,3
	Roll	*Pitch*	*Yaw*	*Roll*	*Pitch*	*Yaw*
Attitude (deg)	1,0	1,0	2,4	2,3	2,0	6,9

Comparing the two best configurations, i.e. LC GPS/INS 21 YVH and TC GG/INS 24 YVH, it can be noted that the obtained performances are quite similar: the first has slightly better performance in the altitude estimation, the second a smaller maximum horizontal position error. These differences are not meaningful, so in this relatively benign scenario the LC and TC approaches provide comparable results, as expected.

To compare the considered configurations in LC and TC architectures, a bar chart of the RMS errors of position, velocity and attitude is shown in Figure 6-53.

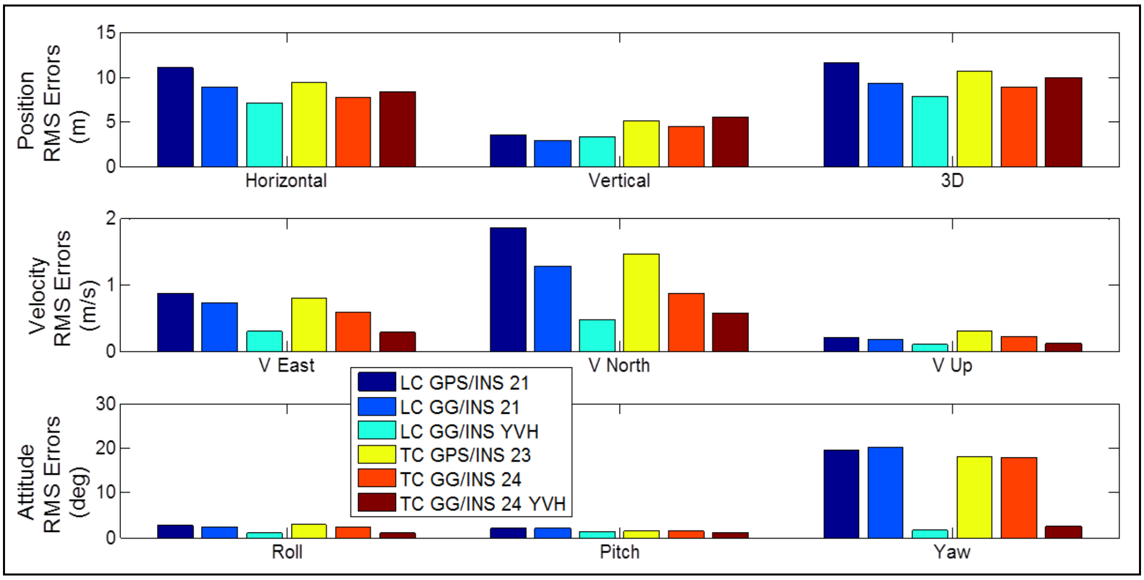

Figure 6-53 – Vehicular Test: Comparison between LC and TC Architectures in terms of Position and Velocity RMS Errors (Segment 3)

The main remarks deduced from the errors overview in Figure 6-53 are:

- In this relatively benign scenario the position performance of all the considered configurations are very similar;
- The LC configurations provide slightly better altitude performance;
- Including GLONASS observations in GPS/INS integration for both LC and TC architectures provides slight improvements in terms of position and velocity;
- Including GNSS-derived yaw aiding and velocity/height constraints yields the reduction of velocity and azimuth errors, but no benefits in position RMS errors.

6.3 Comparison between Pedestrian and Vehicular Test

In this thesis two tests are considered and analyzed: a pedestrian test described in section 6.1 and a vehicular test described in section 6.2. It is interesting to compare the results obtained in these cases, pointing out their operational and environmental differences.

The pedestrian test is carried out mostly on the edge of Calgary's downtown core and so the GNSS visibility conditions are moderately difficult; moreover for this test a high GNSS rate is used (20 Hz), as typically used in pedestrian applications (Pahadia 2010).

The vehicular test is carried out mostly in the downtown core and so the GNSS visibility conditions are often difficult; three segments of the test, representing different scenarios, are analyzed separately. The segment 1, with a maximum GPS outage of 1 minute reduced to 30 seconds including GLONASS, can be considered a difficult scenario. The segment 2, with a maximum GPS outage of 1 minute not reduced by including GLONASS and with a low GG availability (about 50%), can be considered a very difficult scenario. The segment 3, with short GNSS outages and good solution availability (>80%), can be considered a not difficult scenario.

In Table 6-21 some features of the tested scenarios are summarized, showing the GNSS solution availability and the duration of the longest outage in the GPS only and GPS/GLONASS cases.

Table 6-21 – Comparison between Pedestrian and Vehicular Tests

		GPS Availability	*GPS Max Outage*	*GG Availability*	*GG Max Outage*
Pedestrian Test (20 Hz)		82%	45 sec	90%	40 sec
Vehicular Test (1 Hz)	Segment 1	73%	60 sec	81%	30 sec
	Segment 2	53%	60 sec	55%	60 sec
	Segment 3	81%	10 sec	86%	8 sec

To compare the solution of the integration GNSS/INS obtained in the different scenarios, the RMS position errors obtained with the configurations LC GG/INS 21 and TC GG/INS 24 are shown in Figure 6-54.

The results obtained in segment 3 of the vehicular test are clearly the best owing to the benign environment, characterized by only short partial outages. The worst results are obtained in segment 2 of the vehicular test, characterized by long outages also in GPS/GLONASS case. The pedestrian test, carried out in a moderately difficult environment, has the lowest horizontal RMS error.

The LC approach in difficult scenario (segment 2) shows very large RMS position errors (yellow bar in the upper plot of Figure 6-54). Details about the performance of the considered configurations are in sections 6.1.4 and 6.2.3.

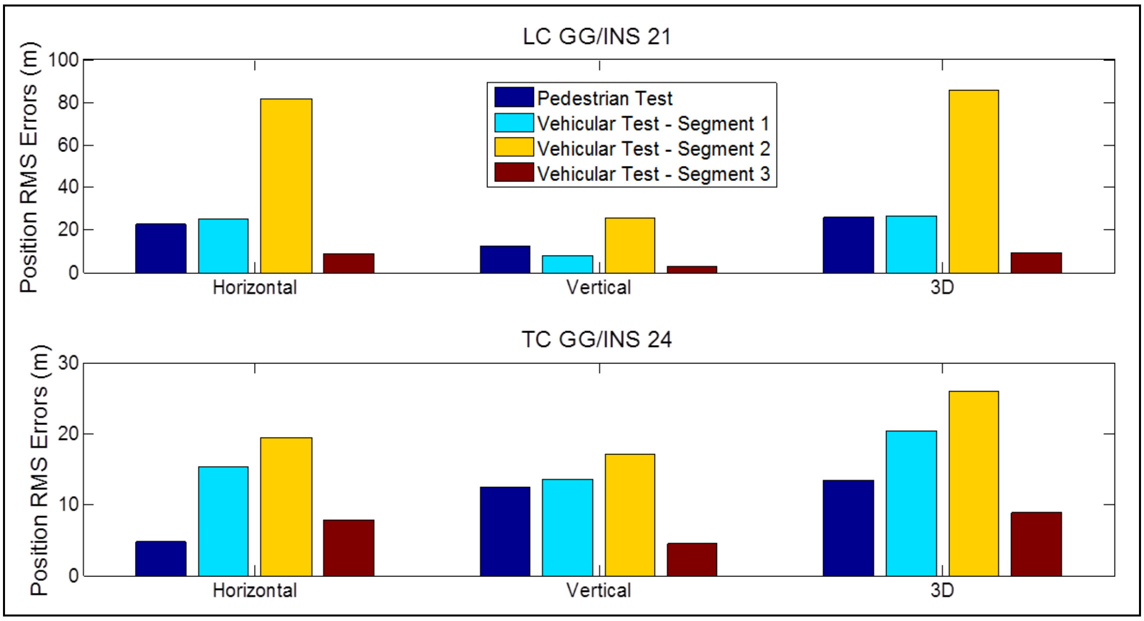

Figure 6-54 – RMS Position Error of Configuration TC GG/INS 24 in Pedestrian and Vehicular Test

Chapter 7 Conclusions

The main objective of this thesis is the performance assessment of the integrated navigation system consisting of a GNSS receiver and a low cost MEMS-based INS in urban environment for pedestrian and vehicular application. The motivations behind the GNSS/INS integration are the GNSS gaps in signal-degraded environment such as urban canyons. The recent enhancements of the Russian satellite system GLONASS suggest the combined use with GPS system in order to increase the GNSS availability; the pseudorange and Doppler observables are processed epoch by epoch in single point positioning. The main equipment includes the NovAtel GPS/GLONASS receiver ProPak-V3 and the MEMS-based Crista IMU from Cloud Cap Technology Inc.

To assess the GNSS/INS performance, the loosely coupled and tightly coupled integration architectures are considered; the tight architecture is able to provide an integrated navigation solution in case of partial GNSS outage, i.e. when the number of visible satellites is insufficient to perform a GNSS positioning. For this reason the tight architecture is commonly used in difficult scenarios for satellite navigation as urban areas; however all the researches carried out in the recent years adopted only GPS system integrated with INS of different grades. One of the objectives of this research is to assess the benefits obtained using additional GLONASS satellites (in addition to GPS satellites) in urban navigation and to determine if the integration strategy plays a significant role, specifically if including GLONASS satellite may change significantly the role of loosely coupling in urban context.

A possible approach to further improve the performance of the integrated GNSS/INS system consists in modeling properly the inertial sensor errors and estimating them in the Kalman filter; the estimated errors are used to bound the INS drift. In this context the inertial sensor errors are modeled with bias and scale factor terms.

The urban environment is characterized by frequent GNSS outages; during a GNSS outage the inertial sensor errors are not continuously estimated and tend to grow rapidly (especially for low cost MEMS sensors). To bound the INS drift, especially in vehicular navigation, pseudo-measurements can be derived from knowledge of vehicle’s motion (also referred to as motion constraints). To improve the azimuth estimation of the considered moving object, an algorithm for the direct observation of azimuth using GNSS measurements can be considered too.

In this work the effectiveness of the motion constraints and of the azimuth aiding are evaluated and pedestrian and vehicular tests are carried out in different operational environments.

7.1 Conclusions

The pedestrian test (analyzed in section 6.1) was carried out on the edge of downtown Calgary (Canada), characterized by areas with good satellite visibility (e.g. parking lot) and by areas with poor visibility (e.g. urban canyon). In case of GPS only positioning, the solution availability is about 80% and the maximum outage has a duration of about 45 seconds; in case of combined GPS/GLONASS positioning, the solution availability rises to about 90% and the duration of the maximum outage is reduced to 40 seconds. These features make the environment a moderately difficult scenario.

The main conclusions from the results obtained in this scenario are:

- The GPS/INS integration in LC architecture provides satisfying performance only in the areas with good visibility or with brief GPS outages. During long outages the solution shows very large errors (several hundreds of meters), which are reduced when accurate INS sensor error modeling is enabled (i.e. including both bias and scale factor terms).
- The GPS/INS integration in TC architecture provides a better solution than the LC case, but with large drift during the long GPS outages (about 100 meters).
- Including GLONASS observations in the integrated system GPS/INS provides meaningful performance improvements in both LC and TC architectures for position and velocity estimation (in the LC case the maximum position error remains large, while is strongly reduced in TC case).
- The GPS/GLONASS/INS integration in LC architecture and the GPS/INS integrations in TC architecture provide similar performance (in terms of RMS errors), suggesting that the former might be a good (and relatively simple) replacement for the latter.
- Including velocity and height constraints to aid the GPS/GLONASS/INS integration produces significant performance improvements in both LC and TC architectures, which show very similar position and velocity RMS errors.

The results obtained with motion constraints demonstrate the effectiveness of this strategy (usually applied in vehicular context) in a particular pedestrian application too;

however it must be pointed out that these results are obtained in a specific arrangement with the IMU fixed on a box, carried on the back of a pedestrian (which somehow acts as a vehicle). More tests are necessary to demonstrate a more general effectiveness of this method in the pedestrian context.

The vehicular test (analyzed in section 6.2) was carried out through the core of downtown Calgary (Canada) and shows very difficult scenarios for satellite navigation, with frequent partial/total GNSS outages of several seconds. Specifically, three test segments, each representing a different operational scenarios, are identified:

- A not difficult scenario, characterized by short GNSS outages (few seconds) and good GNSS solution availability (>85%),
- A difficult scenario, characterized by GPS outage of 60 seconds (reduced to 30 seconds when including GLONASS observations) and a GPS solution availability about 70% (increased to more than 80% when including GLONASS),
- A very difficult scenario, characterized by outages of 60 seconds and solution availability about 50% in the GPS/GLONASS case.

The main remarks deduced analyzing the results obtained in these scenarios are:

- <u>Under benign operational conditions</u> the GPS/INS integration in both LC and TC architectures provides satisfying performance; adding GLONASS satellites and the considered aids slightly improves the performance.
- <u>In difficult scenario</u>
  - The GPS/INS integration in LC architecture shows large errors during the long outage, while in TC approach the errors are significantly smaller.
  - Including GLONASS observations provides meaningful performance improvements for both LC and TC architectures and in terms of position, velocity and azimuth estimation.
  - The GPS/GLONASS/INS integration in LC architecture and the GPS/INS integration in TC approach provide very similar performance (in terms of RMS errors); this might change significantly the role of loosely coupling which could be preferred to tight approach in urban navigation owing to its relative implementation simplicity.

    - Including the GNSS-derided azimuth aiding and the velocity/height constraints produces significant improvements of LC and TC performance in terms of position, velocity and azimuth and the results with the two cases are very similar.
- In very difficult scenario
    - The GNSS/INS integration in LC architecture does not provide satisfying performance for each tested configuration (with GPS and GLONASS, with GNSS-derived yaw aiding, with motion constraints), showing large errors during GNSS outages.
    - The GNSS/INS integration in TC architecture shows better performance relative to LC architecture for each tested configuration. Including GLONASS observations in the integrated system GPS/INS in TC architecture provides slight performance improvements in terms of position, velocity and azimuth estimation; including the azimuth external aiding and the velocity/height constraints only slightly further improves the navigation parameter estimation.

7.2 Future Work

The following research topics would be logical extensions to the work presented herein:

- The PPP technique uses precise satellite orbit and clock products to improve the accuracy of the un-differenced GNSS positioning; similarly the performance of the integrated system GNSS/INS(MEMS) can potentially be improved by using the PPP technique.
- The extended Kalman filter performance strongly relies on the knowledge of the system models and noise properties; the use of an adaptive Kalman filter may improve the filtering performance and can be investigated in urban scenario.
- In vehicular navigation an odometer can be used to aid the velocity estimation in addition to the motion constraints.
- Map-matching techniques can be used to generate motion constraints, helping to keep the INS errors bounded during GNSS outages.
- Including, in the GNSS/INS integrated system, measurements from the rising European GNSS system Galileo or from the Japanese QZSS can potentially improve the integrated performance.

References

Abdel-Hamid, W. (2005), Accuracy Enhancement of Integrated MEMS-IMU/GPS Systems for Land Vehicular Navigation Applications, PhD Thesis, Department of Geomatics Engineering, University of Calgary, Calgary, Canada, UCGE Report No. 20207

Angrisano, A (2006), Sviluppo di Software per lo Studio della Visibilità della Costellazione dei Satelliti GPS, MSc Thesis, Dipartimento di Scienze Applicate, Parthenope University of Naples (in Italian)

Angrisano, A. et al. (2009a), Multi-Constellation System as Augmentation To GPS Performance in Difficult Environment or Critical Application, Proceedings of ENC-GNSS09, Naples

Angrisano, A., Nocerino, E., Troisi S, and Del Core G. (2009), IMU low cost calibration method, Proceedings of ENC-GNSS09, Naples

Angrisano, A., Petovello, M.G. and Pugliano G. (2010) GNSS/INS Integration in Vehicular Urban Navigation, Proceedings of GNSS10 (Portland, OR, 21-24 Sep), The Institute of Navigation

Axelrad, P. and Brown, R.G. (1996), GPS Navigation Algorithms, B. Parkinson and J. J. Spilker, Jr., eds., Global Positioning System: Theory And Applications, volume 1, chapter 9. American Institute of Aeronautics and Astronautics, Inc., Washington D.C., USA.

Bancroft, J.B., Lachapelle, G., Cannon, M.E. and Petovello, M.G. (2008) Twin IMU HSGPS Integration for Pedestrian Navigation. Proceedings of GNSS08 (Savannah, GA, 16-19 Sep, Session E3), The Institute of Navigation

Bar-Shalom, Y., Li , X. and Kirubarajan T. (2001), Estimation with Applications to Tracking and Navigation, John Willey and Sons, New York, 2001.

Bowring, B.R. (1976), Transformation from spatial to geographical coordinates, Survey Review XXIII, 181, July 1976

Brogan W. L. (1981), Improvements and Extensions of GDOP Concept for Selecting Navigation Measurements

Brown, R. G. and P.Y.C. Hwang (1997) Introduction to Random Signals and Applied Kalman Filtering. John Wiley & Sons.

Cai, C. (2009) Precise Point Positioning Using Dual-Frequency GPS and GLONASS Measurements, MSc Thesis, Department of Geomatics Engineering, University of Calgary, Canada, UCGE Report No. 20291

Cai, C and Gao, Y (2009) A Combined GPS/GLONASS Navigation Algorithm for use with Limited Satellite Visibility, Journal of Navigation (2009), 62: 671-685 Cambridge University Press

Chatfield, A. (1997), Fundamentals of High Accuracy Inertial Navigation, AIAA, Inc., 1997.

Conley, R. et al. (2006), Performance of Stand-Alone GPS, Kaplan, E.D. ed., Understanding GPS: Principles and Applications (second edition), Chapter 7, Artech House Mobile Communications Series.

Crista Interface/Operation Document, (2004) Crista Inertial Measurement Unit (IMU) Interface / Operation Document. A Cloud Cap Technology Inc.

Daly, P. and Misra, P.N. (1996), GPS and Global Navigation Satellite System (GLONASS), B. Parkinson and J. J. Spilker, Jr., eds., Global Positioning System: Theory And Applications, volume 2, chapter 9. American Institute of Aeronautics and Astronautics, Inc., Washington D.C., USA.

De Agostino, M. (2010), I Sensori Inerziali di Basso Costo per la Navigazione Geodetica, PhD Thesis, Politecnico di Torino, Italy (in Italian).

Dorsey, A.J. et al. (2006), GPS System Segments, Kaplan, E.D. ed., Understanding GPS: Principles and Applications (second edition), Chapter 3, Artech House Mobile Communications Series.

El-Sheimy, N. (2004) Inertial techniques and INS/DGPS Integration, ENGO 623-Course Notes, Department of Geomatics Engineering, University of Calgary, Canada

El-Sheimy, N., K. P. Schwarz, M. Wei, and M. Lavigne (1995), VISAT: A Mobile City Survey System of High Accuracy, Proceedings of ION GPS 1995 , pp. 1307–1315. Institute Of Navigation.

Farrell, J. A. (2008), Aided Navigation: with High Rate Sensors, McGraw-Hill Publications,

Gautier, J., B. Parkinson (2003), Using the GPS/INS Generalized Evaluation Tool (GIGET) for the Comparison of Loosely Coupled, Tightly Coupled and Ultra-Tightly Coupled Integrated Navigation Systems, in Proceedings of ION 59th Annual Meeting/CIGTF 22nd Guidance Test Symposium, 23-25 June, 2003, Albuquerque, NM, pp. 65-76, U.S. Institute of Navigation, Fairfax VA

Gaylor, D.E. (2003), Integrated GPSINS Navigation System Design for Autonomous Spacecraft Rendezvous, PhD Thesis, The University of Texas at Austin, 2003

Global Positioning System Standard Positioning Service Performance Standard (2008), US Department of Defense, 4th Edition, September 2008

Godha, S. (2006), Performance Evaluation of Low Cost MEMS-Based IMU Integrated With GPS for Land Vehicle Navigation Application, MSc Thesis, Department of Geomatics Engineering, University of Calgary, Canada, UCGE Report No. 20239.

Godha, S., Lachapelle, G. and Cannon, M.E. (2006), Integrated GPS/INS System for Pedestrian Navigation in a Signal Degraded Environment, Proceedings of ION GNSS06, 26-29 Sept., Fort Worth, Session A5, pp. 2151 – 2164, The Institute of Navigation.

Grejner-Brzezinska, D. A., R. Da, and C. Toth (1998), GPS error modeling and OTF ambiguity resolution for high-accuracy GPS/INS integrated system. Journal of Geodesy, 72, pp. 626–638.

Groves, P. (2008), Principles of GNSS, Inertial, and Multisensor Integrated Navigation Systems, Artech House Publishers

Hoffmann-Wellenhof, B., Lichtenegger, H. and Collins, J. (1992), Global Positioning System: Theory and Practice, Springer New York.

ICD-GLONASS (2008) Global Navigation Satellite System GLONASS Interface Control Document, version 5.1, Moscow.

IS-GPS-200 (2004) Navstar GPS Space Segment/Navigation User Interfaces, Revision D, ARINC Research Corporation, El Segundo, CA

Kaplan, E.D. and Leva, J.L. (2006), Fundamentals of Satellite Navigation, Kaplan, E.D. ed., Understanding GPS: Principles and Applications (second edition), Chapter 2, Artech House Mobile Communications Series.

Klein I., Filin S. and Toledo T. (2010), Pseudo-measurements as aiding to INS during GPS outages, Navigation 57(1), pp. 25-34, 2010

Klobuchar, J.A. (1996), Ionospheric Effects on GPS, B. W. Parkinson and J. J. Spilker, Jr., eds., Global Positioning System: Theory And Applications, volume 1, chapter 12. American Institute of Aeronautics and Astronautics, Inc., Washington D.C., USA

Kouba, J. and Héroux, P. (2001), Precise Point Positioning using IGS orbit and clock products. GPS Solutions 5(2): 12-28

Kuusniemi, H., Lachapelle, G. and Takala, J. (2004), Position and Velocity Reliability Testing in Degraded GPS Signal Environments. GPS Solutions, 8 4, 226-237.

Lachapelle, G. (1997), GPS Theory and Applications. ENGO 625 Lecture Notes. Department of Geomatics Engineering, University of Calgary, Canada.

Li, T. (2009), Use of Wheel Speed Sensors to Enhance a Reduced IMU Ultra-Tight GNSS Receiver, MSc Thesis, Department of Geomatics Engineering, University of Calgary, Canada, UCGE Report No. 20300.

Mezentsev, O. (2005), Sensor Aiding of HSGPS Pedestrian Navigation. PhD Thesis, published as UCGE Report No. 20212, Department of Geomatics Engineering, University of Calgary, Canada.

Misra, P., Pratt, M. and Burke, B. (1998), Augmentation of GPS/LAAS with GLONASS: Performance Assessment, ION GPS-98, 11th International Technical Meeting of the Satellite Division of the Institute of Navigation

Nassar, S. (2003) Improving the Inertial Navigation System (INS) Error Model for INS and INS/DGPS Applications, PhD Thesis, Department of Geomatics Engineering, University of Calgary, Canada, UCGE Report No. 20183

Nastro V. (2004), Navigazione inerziale ed integrata, Guida Editore, 2004

Nayak, R. A. (2000), Reliable and Continuous Urban Navigation Using Multiple GPS Antennas and a Low Cost IMU, MSc Thesis, Department of Geomatics Engineering, University of Calgary, Canada. UCGE Report No. 20142

Pahadia, A. (2010), GPS/INS Integration Aided with Gyroscope-Free IMU for Pedestrian Applications, MSc Thesis, Department of Geomatics Engineering, University of Calgary, Canada, UCGE Report No. 20321

Parkinson, B.W. (1996), GPS Error Analysis, B. W. Parkinson and J. J. Spilker, Jr., eds., Global Positioning System: Theory And Applications, volume 1, chapter 11. American Institute of Aeronautics and Astronautics, Inc., Washington D.C., USA.

Petovello, M. (2003) Real-time Integration of a Tactical-Grade IMU and GPS for High-Accuracy Positioning and Navigation, PhD Thesis, Department of Geomatics Engineering, University of Calgary, Canada, UCGE Report No. 20173

Petovello, M. (2009) Estimation for Navigation, ENGO 699.18 - Lecture Notes, Department of Geomatics Engineering, University of Calgary, Canada

Remondi, B. W. (2004), Computing Satellite Velocity Using the Broadcast Ephemeris, GPS Solutions, 8(3):pp.181-183.

Revnivykh, S.G. (2007) GLONASS Status, Development and Application, International Committee on Global Navigation Satellite System (ICG) Second meeting, September 4-7, 2007, Bangalore, India

Roßbach, U. (2000) Positioning and Navigation Using the Russian Satellite System GLONASS, PhD Thesis, University of the Federal Armed Forces Munich, Germany (Universität der Bundeswehr München), June, 2000.

Sairo, H., Akopian, D. and Takala, J. (2003), Weighted dilution of precision as quality measure in satellite positioning, IEE Proc. in Radar, Sonar, and Navigation, 150(6): 430–436, Dec. 2003.

Salychev, O. S. (1998) Inertial Systems in Navigation and Geophysics, Bauman MSTU Press

Satirapod, C. and Wang, J. (2000), Comparing the Quality Indicators of GPS Carrier Phase Observations, Geomatics Research Australasia, vol. 73, pp. 75-92.

Shin, E. (2001), Accuracy Improvement of Low Cost INS/GPS for Land Application, MSc Thesis, Department of Geomatics Engineering, University of Calgary, Canada, UCGE Report No. 20156

Shin, E. (2005), Estimation Techniques for Low-Cost Inertial Navigation, PhD Thesis, Department of Geomatics Engineering, University of Calgary, Canada, UCGE Report No. 20219

Spilker, J. J., Jr. (1996a), GPS Navigation Data, B. Parkinson and J. J. Spilker, Jr., eds., Global Positioning System: Theory And Applications, volume 1, chapter 4. American Institute of Aeronautics and Astronautics, Inc., Washington D.C., USA.

Spilker, J. J., Jr. (1996b), Tropospheric Effects on GPS, B. Parkinson and J. J. Spilker, Jr., eds., Global Positioning System: Theory And Applications, volume 1, chapter 13. American Institute of Aeronautics and Astronautics, Inc., Washington D.C., USA.

Spilker, J. J., Jr. (1996c), Satellite Constellation and Geometric Dilution of Precision, B. Parkinson and J. J. Spilker, Jr., eds., Global Positioning System: Theory And Applications, volume 1, chapter 5. American Institute of Aeronautics and Astronautics, Inc., Washington D.C., USA.

Stockwell, W. (2003) Angle Random Walk. Available at http://www.xbow.com.

Sukkarieh, S. (2000), Low Cost, High Integrity, Aided Inertial Navigation Systems for Autonomous Land Vehicles, Ph.D. Thesis, Australian Centre for Field Robotics, Dept. of Mechanical and Mechatronic Engineering, The University of Sydney, Sydney, Australia.

Tiemeyer B. (2002), Performance Evaluation of Satellite Navigation and Safety Case Development, PhD Thesis

Wang, D. (2010) Performance Evaluation of GPS L1/L2 Positioning with Partial Availability of the L2C Signals. MSc Thesis, Department of Geomatics Engineering, University of Calgary, Canada, UCGE Report No. 20314

Ward, P.W. etal (2006), GPS Satellite Signal Characteristics, Kaplan, E.D. ed., Understanding GPS: Principles and Applications (second edition), Chapter 4, Artech House Mobile Communications Series.

Wells, D.E., N. Beck, D. Delikaraoglou, A. Kleusberg, EJ. Krakiwsky, G. Lachapelle, R.B. Langley, M. Nakiboglu, K.P. Schwarz, J.M. Tranquilla and P. Vanic'ek (1987) Guide to GPS Positioning, Second Edition, Canadian GPS Associates, Fredericton, N.B., Canada.

Wieser, A. (2001), Robust and fuzzy techniques for parameter estimation and quality assessment in GPS, Ph.D. thesis, Graz University of Technology

Yang, Y. (2008), Tightly Coupled MEMS INS-GPS Integration with INS Aided Receiver Tracking Loops, PhD Thesis, Department of Geomatics Engineering, University of Calgary, Canada, UCGE Report No. 20270